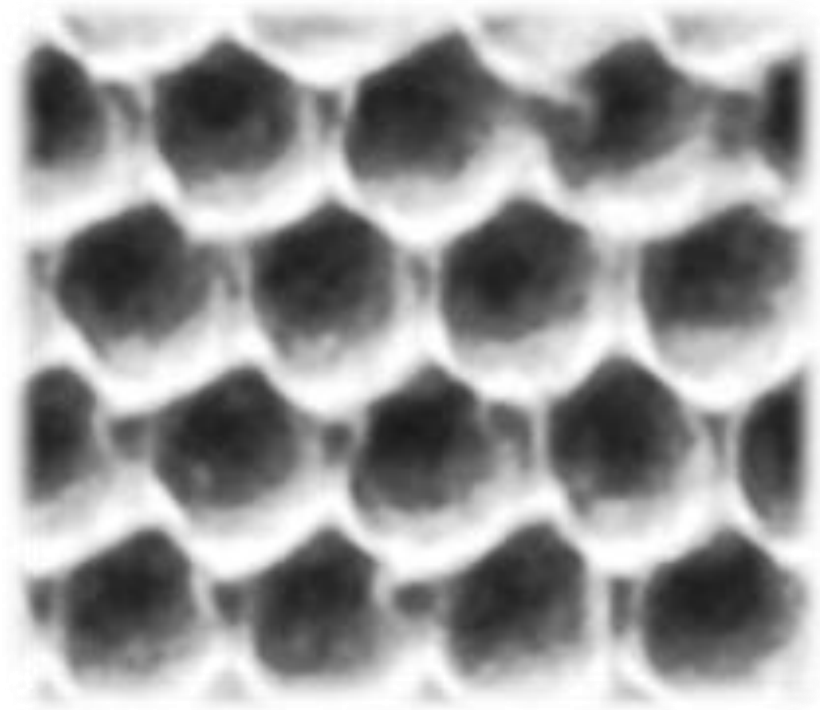




Anna Katarzyna Piotrowska

Mechanochromic Photonic Crystals as Strain Sensors for Structural Applications





UNIVERSITY OF TRENTO - Italy
Department of Civil, Environmental
and Mechanical Engineering



Doctoral School in Civil, Environmental and Mechanical Engineering
Topic 1. Civil and Environmental Engineering - XXIX cycle 2014/2017

Doctoral Thesis - December 2017

Anna Katarzyna Piotrowska

Mechanochromic Photonic Crystals as Strain Sensors for Structural Applications

Supervisors

Daniele Zonta (Department of Civil and
Environmental Engineering, University of Strathclyde;
Department of Civil, Environmental and Mechanical
Engineering, University of Trento;
Institute for Photonics and
Nanotechnologies, National Research Council)

Maurizio Ferrari (IFN-CNR CSMFO
Lab. & FBK Photonics Unit; Centro di Studi e Ricerche
“Enrico Fermi”)

Lidia Žur (Centro di Studi e Ricerche
“Enrico Fermi”; IFN-CNR CSMFO Lab. & FBK Photonics
Unit)

Andrea Chiappini (IFN-CNR CSMFO
Lab. & FBK Photonics Unit, Povo-Trento, Italy)

The cover image refers to the internal structure of experimental sample. The picture was taken by a scanning electron microscope (SEM), for sample with the diameter of holes equal to $\sim 1 \mu\text{m}$. The holes create the hexagonal close packed (hcp) lattice at the top surface of sample. Their hexagonal arrangement refers to the hexagonal shape of unit cell, which is assumed as the principle element of periodic structure

Except where otherwise noted, contents on this book are licensed under a Creative
Common Attribution - Non Commercial - No Derivatives 4.0
International License (Times New Roman 9pt)

ISBN (paper): ; ISBN (online):

University of Trento
Doctoral School in Civil, Environmental and Mechanical Engineering
<http://web.unitn.it/en/dricam>
Via Mesiano 77, I-38123 Trento
Tel. +39 0461 282670 / 2611 - dicamphd@unitn.it

Preface

Structural Health Monitoring is an important aspect in civil engineering, dedicated to monitor and maintain the structural conditions of civil architecture objects. It results in extension of their life time and appropriateness for human use.

Present, commercially available sensors for SHM are complex, sophisticated and multicomponent systems. Although, they provide high precision of measurements, their total cost (the price and costs of exploitation) has been still too high to be commonly applicable. There are also other disadvantages such as distributed architecture, heavy cables or their sensitivity to electromagnetic interference like it is in case of conventional electrical sensors. Unlike them, more advance fiber optic sensors are robust to external fields. However, they involve the infrared light for data transmission, therefore they desire additional support of other devices for data processing.

Now a day, there is a lack of portable sensing instruments supporting more sophisticated technologies, whose applications can be reduced by failure assessing with those instruments.

Current investigations have been focused on development of structures that can be used as an independent sensing tool without a power supplier, such as mechanochromic photonic crystals with three-dimensional structure. Their mechanochromic properties are visible with naked eye as a color variation on their top surface stimulated by mechanical deformation of the structure. However, their fabrication desires high precision to obtain sample with the high sensitivity to stretching and omit some limitation corresponding to its composition (deeply described in chapter 4). Hence, there is need to find alternative solutions. One of them refers to two-dimensional photonic crystals, which were intensively investigated as a components of sensing systems such as MOEMSs (micro-opto-electro-mechanical microsystems). However, their main disadvantage is the fabrication that involves the lithography techniques, which are quiet expensive and time-consuming. Furthermore, the lithographic techniques desire clean room conditions. Hence, the number of produced specimens is limited.

In this thesis, there is proposed completely new approach to develop a strain sensor, including fabrication of strain-sensitive sample and methodology of measurements. The sample was fabricated as two-dimensional finite structure of hexagonally arranged voids on the PDMS substrate. The applied fabrication protocol was cost-effective and not time-consuming. The final product was a PDMS replica of monolayer colloidal crystal obtained by self-assembly of polystyrene colloidal spheres. Further investigations involved diffractive properties of its periodic structure. Its strain sensitivity was investigated by monitoring the parameters of diffracted (transmitted or reflected) light such as the diffracted wavelength (chapter 6) and the polarization (chapters 7 and 8), which vary by stretching the sample. Moreover, there was tested another approach, which involved shape changes in diffraction pattern. The diffraction pattern is a result of interaction between a periodic structure and an illuminating light.

The obtained data confirmed strong relationship between optical response and the geometry of diffractive structure. However, the experiments require further optimization of fabrication protocol, methodology (conditions of measurements, sample parameters, an appropriate arrangement of components in the experimental setups)

Anna Katarzyna Piotrowska was a master student at the Department of Physics of Warsaw University of Technology. In September 2010, she completed the master course at the Faculty of Technical Physics with the very good result, and received the degree of Master of Science in Engineering, with the major in optoelectronics.

In 2008, as a master student, she had a work placement at PCO S.A. (the Polish factory of optoelectronic devices, providing equipment for military forces, the security service and the police). Since 2011, she has been employed as junior researcher at National Institute of Telecommunications. She has been involved in several research projects and statutes works referring to photonics aspects of optical fiber data transmission.

Since 2014, she has been a Phd student at the Department of Civil, Environmental and Mechanical Engineering of the University of Trento (Italy), and at the "Photonics: Materials, Structures and Diagnostic" Trento IFN UOS of the Institute for Photonics and Nanotechnologies (IFN). Her research activities referred to structural features and optical properties of photonic crystals (two- and three dimensional structures) applicable for strain sensing in structural health monitoring (SHM).

*To my parents
for their patience and sustainable support,
and to my brother
for his enormous sense of humour*

Related publications

- Ferrari M., I. Vasilchenko, S. Normani, A. Piotrowska, A. Chiappini, A. Chiasera, et al. 2014, “Photonic Glasses and Confined Structures” Presented at XII Encontro da SBPMat, João Passoa, September 28 – October 02.
- Ferrari M., I. Vasilchenko, S. Normani, A. Piotrowska, A. Chiappini, A. Chiasera, et al. 2014, “Photonic Glasses and Confined Structures” Presented at 3rd International Workshop of Fundamentals of Light-Matter Interaction, Recife Brazil, October 05-08.
- Chiappini A, A. Piotrowska, M. Marciniak, M. Ferrari, D. Zonta, “Design and Fabrication of Mechanochromic Photonic Crystals as Strain Sensor” Submitted to present at Smart Structures-NDE 2015, San Diego, March 8 – 12, 2015.
- Chiappini A, A. Piotrowska, M. Ferrari, D. Zonta. “Method and measurement system of 2-dimensional strain tensor field of a substrate based on photonic coating with sub-micrometric structure and interrogation through polarized light.” Patent under proceeding.
- Piotrowska A.K., A. Chiappini, C. Armellini, A. Lukowiak, D. Zonta, G.C. Righini, R. Ramponi, M. Marciniak, M. Ferrari. 2015. “Mechano-responsive Elastomeric Photonic Crystals for Strain Detection.” Presented at XVIII AISEM Annual Conference, Fondazione Bruno Kessler, Trento, February 3 – 5.
- Chiappini A., Piotrowska A., M. Marciniak, M. Ferrari, and D. Zonta. 2015 “Design and fabrication of mechanochromic photonic crystals as strain sensor”, Proceedings of SPIE 9435:94350J-1/13;
- Piotrowska A. K., A. Chiappini, D. Zonta, and M. Ferrari 2015. “Investigating the Strain Sensitivity of Photonic Crystals.” Presented at FOTONICA 2015, 17th Edition, Torino, May 6 – 8;
- Minati L., A. Chiappini, F. Benetti, D. Zonta D., A. Piotrowska, M. Marciniak, and M. Ferrari, “Fabrication and optical properties of assembled gold nanoparticles film on elastomeric substrate”, *Colloids and Surfaces A: Physicochemical and Engineering Aspects* 482:431–437.
- Piotrowska A.K., A. Chiappini, A. Lukowiak, C. Armellini, A. Carpentiero, M. Mazzola, S. Varas, M. Marcinak, M. Ferrari, and D. Zonta. 2015. “Strain-sensitive photonic crystals for sensing applications in structural health monitoring.” Proceedings IEEE Workshop on Environmental, Energy and Structural Monitoring Systems (EESMS 2015): 102-106, Trento, 9-10 July. doi: 10.1109/EESMS.2015.7175860

- Piotrowska A., V. Piccolo, A. Chiappini, Maurizio Ferrari, M. Pozzi, L. Deseri, D. Zonta. 2015. “Mechanochromic Photonic Crystals for Structural Health Monitoring”. Proceedings 10th International Workshop on Structural Health Monitoring (IWSHM 2015), doi: 10.12783/SHM2015/386.
- Piccolo V., A. Piotrowska, A. Chiappini, A. Vaccari, M. Ferrari, L. Deseri, and D. Zonta. 2016. “Numerical Characterization of Mechanochromic Photonic Crystals for Structural Health Monitoring” Proceedings EWSHM 2016, 8th European Workshop On Structural Health Monitoring, Bilbao, Spain, July 5-8
- Piccolo V., A. Piotrowska, A. Chiappini, A. Vaccari, M. Ferrari, L. Deseri, D. Zonta. 2016. “Photonic crystal slab strain sensors: A viable tool for structural health monitoring”. Proceedings ICTON 2016: 18th International Conference on Transparent Optical Networks, Trento, Italy, July 10-14, pp. 1-4. doi: 10.1109/ICTON.2016.7550655
- Piotrowska A., D. Zonta, M. Ferrari, and M. Marciniak. 2016. “Mechanically tuneable 2D and 3D Photonic Crystals for strain sensing and structural health monitoring.” 7th International Conference on Optical, Optoelectronic and Photonic Materials and Applications ICOOPMA 2016, Paper Tu-B3 –I2–Invited, Detailed Program page 45, June 12-17, 2016, Polytechnique Montréal, Canada
- Piotrowska A., D. Zonta, M. Ferrari, M. Marciniak. 2016. “Strain Detection in Two- and Three-Dimensional Periodic Structures with the Low Index Contrast by Monitoring Their Optical Response.” 24th Optical Wave and Waveguide Theory and Numerical Modelling Workshop, paper p-0,1Book of Abstracts p. 35, Warsaw University of Technology, Warsaw, Poland, 20-21 May 2016, co-located with the 18th European Conference on Integrated Optics (ECIO 2016).
- Chiappini A., C. Armellini, A. Vaccari, V. Piccolo, A. Piotrowska, D. Zonta, and M. Ferrari. 2017. “Assessment of The Chromatic Behavior of Colloidal Sensors” Presented at FOTONICA 2017, 19th Edition, Padova, May 3 – 5;

Acknowledgement

First of all, I dedicate my sincere thanks to Prof. Marian Marciniak for His sustainable support over the three-years period of my PhD studies, and for valuable suggestions and advices how to develop theoretical aspects of my PhD thesis.

Furthermore, I would like to express my profound gratitude to my supervisors, Dr. Maurizio Ferrari and Prof. Daniele Zonta, for their patience and motivation to continue the measurements, and for discipline with their performance.

However, the greatest contribution to develop the experiments comes from the laboratorial staff. Hence, I would like to thank two my mentors, Cristina Armellini and Dr. Andrea Chiappini, who provided me priceless support to understand the key aspects of investigations, and shared their amazing knowledge to improve my experimental skills. Besides Cristina Armellini and Andrea Chiappini, I would like to mentioned three other people, who supported my laboratorial activities with their technical knowledge and skills i.e. Alessandro Carpentiero, Maurizio Mazzola and Stefano Varas. In particular, I dedicate my great thanks to Maurizio Mazzola for His priceless help with the measurements, and for the LabView application to control the monochromator, which improved the measurements significantly.

Last but not the least, I would like to thank my dear friend, Dr. Lidia Žur, for her help with the final version of my PhD thesis; and Dr. Alessandro Chiasera for his clarifications of the optical aspects of experiments.

Contents

1	Introduction	13
1.1	Motivation	13
1.2	Objective	13
1.3	Method	14
1.4	Thesis outline	15
2.	State of the art in structural health monitoring (SHM)	19
2.1.	Civil structural health monitoring	19
2.1.1	General information about SHM systems	19
2.1.2	Methodology	22
2.1.3	Types of tests in structural health monitoring	26
2.1.4	Key aspects of SHM systems design	30
2.2.	Commercially available sensors	32
2.2.1	Fibre Optic Sensors (FOSs)	34
2.2.2	Piezoelectric sensors	38
2.2.3	Self-diagnosing fibre reinforced composites	41
2.3.	Optical approach for strain detection: innovative materials with strain-sensitive optical parameters and optical techniques to detect structural deformation	45
2.3.1	Optical techniques to measure displacement, and examples of their applications.	45
2.3.2	Innovative materials with strain-sensitive optical parameters	59
3.	State of the art in diffraction gratings	61
3.1.	Definition and classification of diffraction gratings	61
3.2.	Mathematical description of diffraction influenced by deformation of diffraction grating	72
3.3.	State of the art in diffraction gratings as applied to SHM	76
4.	Photonic Crystals (PhCs)	86
4.1	Definition and classification of photonic crystals	86
4.1.1	Light interaction with 2D photonic crystals	90
4.1.2	Light interaction with 3D photonic crystals	93
4.2.	Mathematical description of photonic band-gap effect	96
4.3.	Photonic crystals as strain sensors	101
4.3.1	Strain – sensitivity of photonic crystal slabs (PhCSs)	101
4.3.2	Mechanochromic properties of colloidal crystals	106

5. Fabrication of 2D slab	109
5.1 Introduction	109
5.2 Materials properties	110
5.2.1 Monodispersed colloidal spheres	110
5.2.2 Monolayer colloidal crystals (MCCs) and their derivatives	117
5.2.3 Polydimethylsiloxane (PDMS)	124
5.3 Process	130
5.4 Results	134
6. Strain sensitivity assessed by analysing the light spectrum of diffracted incoherent light transmitted by the sample	143
7.1 Introduction	143
7.2 Experimental set up and acquisition program	146
7.3 Results and discussion	149
7.4 Conclusions	152
7. Estimation of the strain based on transmission measurements: changes in shape of diffraction pattern and in the polarization of the diffracted light	153
7.1 Introduction	153
7.2 Experimental set up	156
7.3 Results	159
7.4 Discussion	164
7.5 Conclusions	164
8. Strain sensitivity estimated by measurements in reflection mode, referring to the shape changes of diffraction pattern and the polarization of diffracted light	166
8.1 Introduction	166
8.2 Experimental setup	167
8.3 Results and Discussion	170
8.4 Conclusions	175
9. Conclusions and further developments	177
9.1 Conclusions	177
9.2 Further developments	179
References	181

Chapter 1

Introduction

1.1 Motivation

The motivation to this work was provided by present market of sensors that are complex, multi-components systems requiring integrated knowledge and intensive collaboration between experts in various field of science and engineering. Hence, their price and costs of their exploitation are high. Other disadvantages refer to technical issues of their design. All current sensors are distributed systems. Additionally, the more conventional of them such as electrical strain gauges are heavy because of electrical wires, and require power supply. Hence, they cannot be used everywhere where it is desired. Furthermore, they exhibit strong sensitivity to the electromagnetic interference (EMI). Unlike them, fibre optic sensors are lightweight, small, electrically passive, nonconductive, immune to EMI and atmospheric conditions, electrically passive, low loss, etc. Although, they enable detailed analysis of failures, they operate within the range of infrared. Therefore, they are supported by several optoelectronic subsystems to obtain appropriate data.

Regarding all these issues, the recent investigations aim to simplify structural health monitoring systems by reducing their size or development novel, innovative materials that do not require power supply, and limit use of more sophisticated and expensive technologies only there where they are indispensable.

1.2 Objective

The main purpose of the project was to design and manufacture photonic crystal sample with mechanochromic properties i.e. reacting to mechanical deformation in visible way, by changing the colour of surface. The previous experiment (Zonta et al.2009) showed that such materials provide great opportunities to develop a strain sensitive

material supporting currently available sensors. Obviously, the parameters of such material determining its strain sensitivity are not comparable with those of more sophisticated sensors. However, they can be involved at early stage of damage to assess how serious is the failure and limit use of present used sensors only there where it is urgently needed. This could help avoiding additional costs of exploitation of advanced technologies, and efforts of installing complex sensing systems at places with limited access. In fact, the costs of SHM could be significantly decreased. Therefore, it was reasonable to continue efforts to optimize the PhC structure to avoid limits that appeared during previous experiment and referred to properties and size of polystyrene spheres.

1.3 Method

This project was developed in two ways. At the beginning, the protocol of sample fabrication was proposed. The manufacture was running in three steps. Each step provided other product that was involved in the next step. The first step hired the self-assembly of polystyrene colloidal spheres to obtain monolayer colloidal crystal template. In the next step, the PDMS was deposited on the template and removed with the spheres within it. The colloidal spheres confined within PDMS matrix is called a replica of monolayer colloidal crystal. In the last step, the spheres are etched with dimethylformamide. In fact, the final product of fabrication is an inverse replica of monolayer colloidal spheres. In spite of no mechanochromic effects (typical for three-dimensional photonic crystals) on the sample surface, the further investigations exploit its diffractive properties. However, some color effects induced by an incident white light were observable. It is so called blazed effect, which is typical for diffraction gratings obtained by chemical wet etching (Popov 2012).

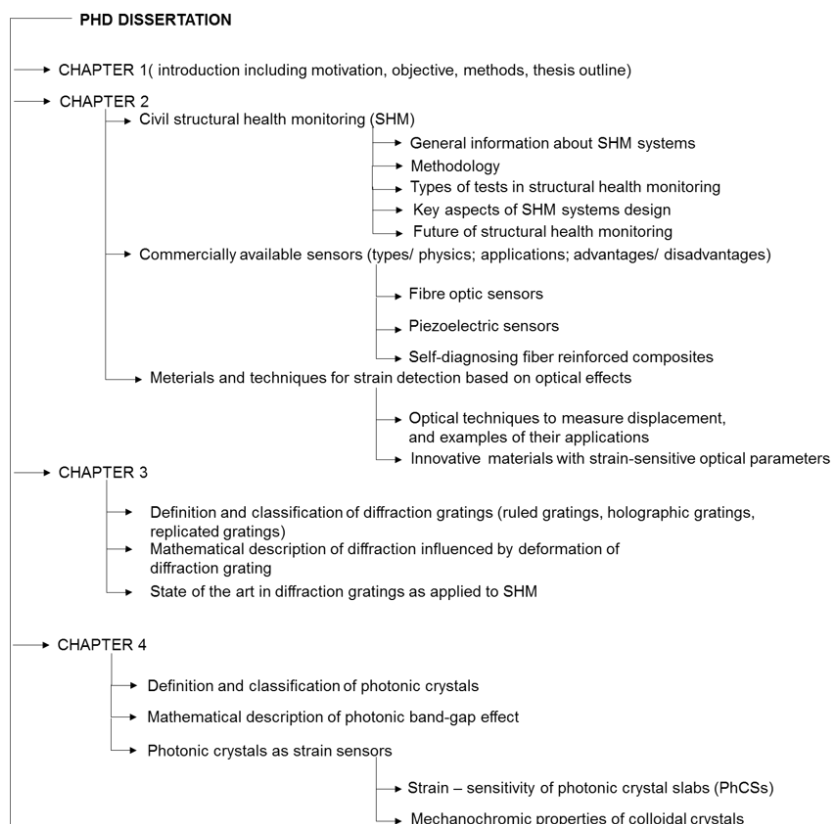
Further measurements were performed in the reflection and transmission modes (Chapter 6 – Chapter 8). The object of investigations was the diffraction pattern, which is here considered as main source of information about changes induced by structural deformation. The geometrical changes were detectable by CCTV camera. However, these measurements are strongly affected by noises coming from the screen background, and/or correlated with straight, and ghost lines.

In the other approach (Chapter 6), the analysis was performed based on light spectra of diffracted light, which was performed for each spot and each step of elongation separately. Another approach assumed to detect changes induced by deformation by measure the polarization variations of diffracted light.

In the experiment (chapters 6, 7 and 8), main efforts were focused on development of methodology of measurements and finding appropriate conditions to avoid additional errors and improve the quality of results. Nevertheless, this issue depends strongly also on the sample quality. Therefore, the fabrication protocol should be optimized.

1.4 Thesis outline

As shown in Fig. 1.1, the entire composition is divided into nine chapters. Starting from chapter 2, three subsequent chapters include fundamental theory of structural health monitoring (SHM), diffraction gratings, and photonic crystals (PhCs), respectively.



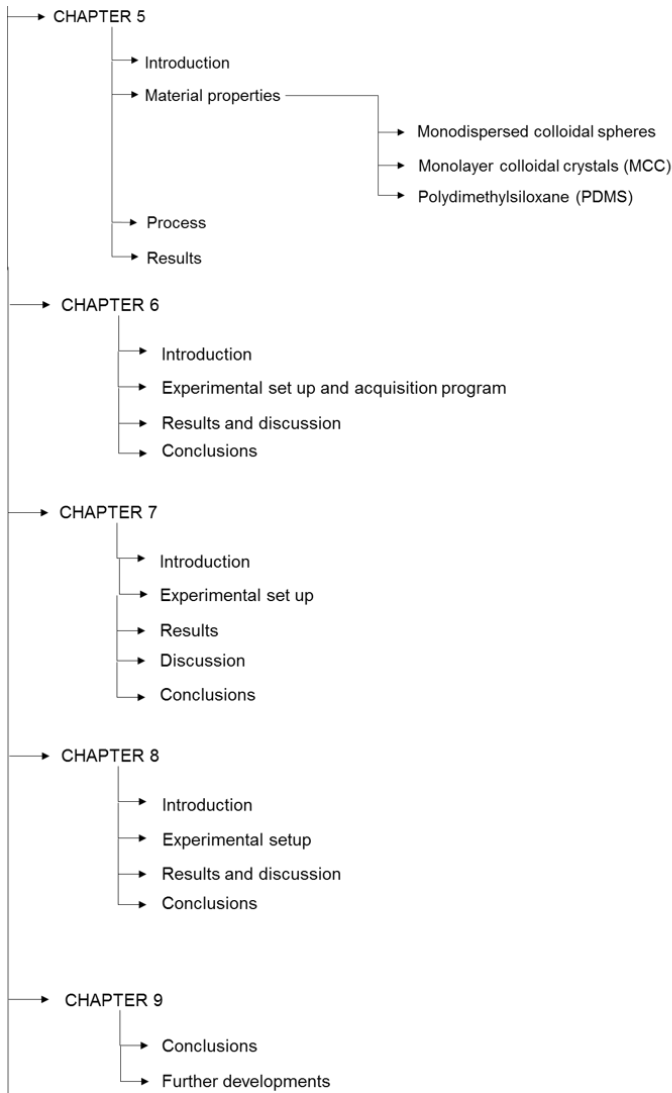


Figure 1.1. Schematic representation of PhD thesis composition.

In particular, great attention was put to describe the practical aspects of these issues. Hence, in chapter 2, there are given details of currently available sensors (methodology, applications, and advantages/disadvantages). In chapter 3 and 4, there are described the investigations on diffraction gratings and photonic crystal, respecting their strain sensitivity.

Although, the main theoretical aspects of thesis are described in chapter 1, 2, 3, also the experimental chapters (5, 6, 7, and 8) include theoretical introductions with basic information allowing understanding the methodology of experiments.

Chapter 2 includes state of the art in structural health monitoring. Hence, there are presented the main aspects of methodology, objective and applications. Furthermore, it describes physics, use, advantages and disadvantages of currently available strain sensors. To compare, it is summarized by examples of running investigations on innovative materials and applicable optical methods for detection of structural damages.

Chapter 3 covers the fundamental theory of diffraction gratings. To compare with the experiment, the theory includes information about available methods to fabricate diffraction gratings, the parameters determining their quality, basic selection of diffraction gratings, and mathematical formalism of optical response stimulated by applied stress. It refers to structural health monitoring by given examples of recent investigations on strain sensitivity of diffraction gratings.

The main objects of chapter 4 are photonic crystals. Here, the basic theory of photonic crystals is given. It includes the selection of photonic crystals into 1D (multilayer stack), 2D (photonic crystal slab), and 3D (opals) photonic crystals, main parameters and terminology for their characterization. Furthermore, they are considered as diffractive element interacting with incident light, for which the mathematical formalism is developed. The last subchapter refers to the recent investigations (theoretical and experimental) on strain-sensitive 2D and 3D structures.

Chapter 5 initiates the experimental part of thesis and described key aspects of fabrication protocol. It is started by theoretical introduction with detailed characteristic of properties of involved materials. The last subchapter presented a detailed sample analysis performed based on AFM images and SEM images, as well as observations performed during the investigations.

Chapter 6 refers to the first experiment, which involved a fibre detector to collect intensity of light diffracted by the stretched diffraction grating. The results were graphed as a function of wavelength (the sample was illuminated by various wavelength of visible light ranging from 400 nm to 700 nm). The final results show that for different step of elongation

the diffracted wavelength is different, what corresponds with moving peak of light spectrum along horizontal axis.

In **Chapter 7** new instrument to data collection was tested. The object of investigation was the same, diffraction pattern. Sample stretching indicates the shape changes of diffraction pattern, which were registered by CCTV camera. Each image corresponded to the other step of elongation. In fact, it was possible to estimate how the distance between the centres of spots at the same diagonal varies during elongation. Simultaneously, it was observed a brightness variation of diffraction image. Based on Malus' law and measurements performed in grey scale, the polarization of diffracted light was computed.

Chapter 8 reports on the last measurements. Like previously, the geometrical changes of diffraction pattern and the polarization of diffracted light were estimated. However, unlike previously, the measurements were performed in the reflection mode.

Chapter 9 includes summarize of results provided by each experimental chapter. Moreover, the applied techniques were revised and their alternatives were proposed. The final conclusions refer to possible ways to develop the experiment and optimize the results.

Chapter 2

State of the art in structural health monitoring (SHM)

2.1. Civil structural health monitoring

Structural health monitoring can be defined as a non-destructive in-situ structural evaluation method, which involves several types of sensors that can be embedded or attached to investigate structure and to provide complete data about it. To assess the structural conditions this data is transmitted, stored and proceeded by using statistical methods. Moreover, the data can be used to evaluate the safety, the integrity, the strength or the performance of the structure, and to identify damage at its onset.

Usual activities of SHM focus on assessing the condition of structure, or its key components based on their response for different types of loading. The most common tools to obtain the data are non-destructive testing (NDT) and non-destructive evaluation.

2.1.1 General information about SHM systems

Generally, structural health monitoring relies on evaluation of health condition of civil structures such as bridges, buildings, tunnels, pipes, highways and railways, based on data obtained by the sensors attached to them or embedded inside them. To date, commercially available sensors are multicomponent systems, complex in their structure and involving numerous processes, such as:

- data acquisition (a sensory system);
- data transfer;
- intelligent processing and analyzing of data;
- storage of processed data;
- diagnostics (i.e. damage detection and modelling algorithms);

- retrieval of information as required.

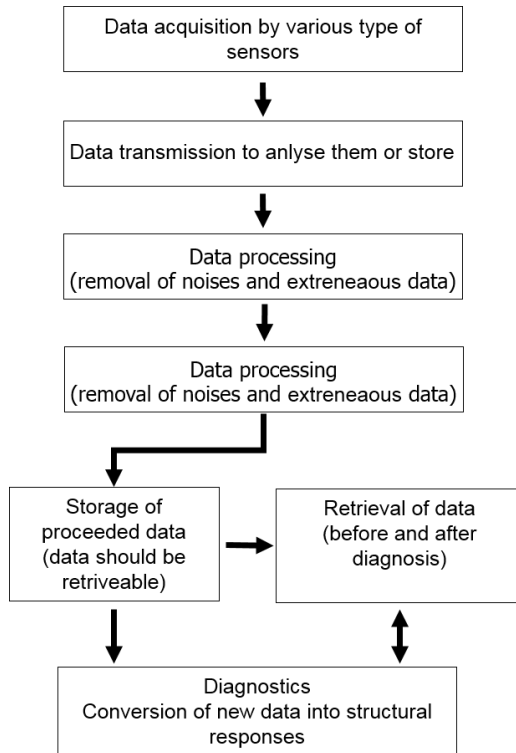


Figure 2.1. Data flow in typical SHM system. Based on (ISIS Canada 2004).

With respect to the name, especially the word health, the body analogy is commonly used, which compares SHM to the medical investigation performed by a doctor on a patient. In both cases, immediate preventative action can avert catastrophic consequences (ISIS Canada 2004).

Other section of SHM system refers to the types of involved test. Generally, there are four tests (as illustrated in Fig.2.2 with their subcategories), which differ from each other for methods of data collection and its timescale, i.e.:

- static field testing;
- dynamic field testing;
- periodic monitoring;
- continuous monitoring;

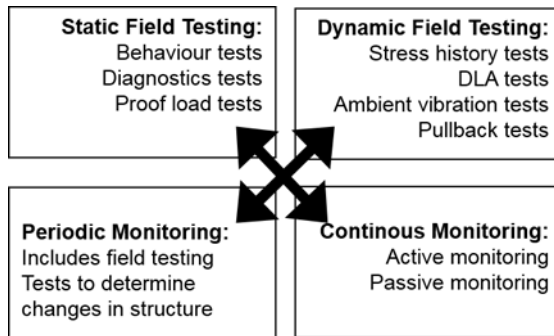


Figure 2.2. Four tests applied for SHM with their subcategories. Based on (ISIS Canada 2004).

There is also another classification of SHM systems that is based on four levels (the highest level corresponds to the most advanced SHM system) as follow:

- **LEVEL I:** the systems are capable to detect damages in a structure, but they are not able to provide any information about their nature, location, or severity. Hence, they don't allow assessing the safety of the structure.
- **LEVEL II:** these systems are more sophisticated than those of LEVEL I. Expect damage detection; they detect also its location.
- **LEVEL III:** the systems detect and pinpoint damages and they also provide some information about their severity.
- **LEVEL IV:** the systems of this level are the most advanced (complex) and the most expensive. They provide detailed information about damage i.e. the presence, location, and its severity. Furthermore, they allow assessing the safety of structure.

The benefits for civil engineering provided by SHM are obvious and related to increasing structural safety, decreasing ongoing inspection and maintenance costs. In particular, they refer to the following aspects:

- early damage detection (Lau 2003), that is one of the primary objective of SHM;
- improve understanding of in-situ structural behaviour;
- assurance of a structure's strength and serviceability;
- improve maintenance and management strategies for better allocation of resources;

- enables and encourages use of innovative materials

2.1.2 Methodology

As shown in Fig.2.1, SHM systems are multicomponent arrangement of subsystems that refer to various disciplines (i.e. civil engineering, material science, damage detection, sensors, data management and intelligent processing, computers and communication) and collaborate with each other to provide fast and reliable data flow. The main tasks of each component are discussed below.

Acquisition and collection of data

The main objective of data collection and acquisition is to obtain complete information about structural parameters such as: strains, deformations, temperature, moisture levels, acoustic emissions and loads. There are several sensors commonly involved to measure those parameters, e.g. *load cells electrical resistance strain gauges, vibrating wire strain gauges, displacement transducers, accelerometers, anemometers, thermocouples and fibre optic sensors*. Their accurate choice depends on the conditions and objectives of their use.

The data collection and acquisition refer to the largest amount of activities, such as:

- **selection of sensor:** is the essential step that determines the desired quality of the measurements. There are several criteria for sensor selection, such as: *its ability to measure a specific parameter (strain or vibration), accuracy, reliability, limitations in their installation, power requirements, signal transmission limitations, durability and cost of sensory system*. ‘Sensory system’ refers to the sensor and other supporting devices such as: wires, cables and the signal conditioning/data acquisition system. The time over which the sensor can be intensively exploited is a key aspect that has to be taken into account. There are some sensors that are useless for long-term monitoring because of deterioration in their performance with time. Moreover, the appropriate location of the sensors inside the structure allows keeping them in good conditions.
- **sensor installation and placement:** the sensor should be installed within the structure to not affect its behaviour (Isis Canada 2004). In fact, the arrangement of all components of

sensory system (i.e. sensor wiring, conduit, junction boxes, etc.) should be accounted during its design. Although, the sensors are quiet durable, the poor durability of cables and poor design of data acquisition system reduce significantly the functionality of SHM system.

- **transfer to data acquisition system (DAS):** this is an onsite system supporting signal demodulation, conditioning and storage coming directly from the sensors. These actions provide data ready to be sent to the off-side system for further analysis. The data acquisition system has usually the input for incoming signals (for the FOS it is a reflected light) and the output for the transmission to the offsite systems (for FOS systems these are strain values calculated based on incoming signal from sensors). Then, the output data are stored in a buffer or long-term memory. The most common technique to transfer the data to/from the DAS is via lead cables (wires). Nevertheless, there are also other techniques such as wireless technique, which is more expensive and slower than the traditional one, and the data are not secure. There are also some systems involving combination of two techniques. For example, the incoming signal is delivered to the DAS via wires, whereas the data for analysis are provided via wireless connection. Although, data transmission via lead cables is currently the most widely used technique, it is not perfect and provide some difficulties. Sometimes, especially when data are transmitted for a long distance, they can be distorted by errors resulting from the electromagnetic interference. This effect is typical in high-voltage power lines and radio transmitters. The solution of this problem is constituted by differential signalling techniques and properly shielded cables. Nevertheless, for some applications, wire data transmission is an inappropriate solution. It is in two extremely different cases, i.e. in small systems, where the long cables are problematic, and in very large systems, where data sensor signals might be corrupted by excessive noise.
- **data sampling and collection:** this step starts after the data arrival at DAS and before sending them for analysis. It requires an adequate data acquisition algorithm, which captures the necessary amount of data. It is important, especially for systems collecting a large amount of data, over a long time (what usually

relates to continuous monitoring). Hence, the general rule to avoid problem with management of large data amount is that the quantity should not be scanty, even not voluminous. The sampling rate should match the type of test. The low rate leads to the former, whereas too high rate provides the latter.

Communication of data

Communication of data refers to data transmitting between two places, which usually are remote from each other for a long distance. One of them is a place, where the data are collected and stored, whereas another relates to the data processing and its analysis. In general, present modern SHM systems use wireless technologies for data transmission such as radio or cellular transmission, or another more recent approach involves telephone lines or internet. More details on this topic were given in (Han, Newhook and Mufti 2004).

Intelligent processing and management of data

The data obtained by sensors contain extraneous information and noises that make them almost useless for structural health monitoring. Hence, data processing is desired before their storage and analysis. In general, data processing aims to prepare data for easier, faster and more accurate interpretation. In reality, this process removes also the influence of thermal and other undesired effects in the data. With respect to the amount of data and the complexity of measurements, several techniques of data processing were developed, which remove without destructing the integrity of overall system. For instance, in the simplest method, only changes in readings are recorded. Hence, long time periods without any changes are kept. In this way the amount of data is reduced, making their transfer faster and the time for their delivery to be analysed shorter. An alternative approach introduces the threshold values, above which values are registered or it just record their maximum corresponding to a certain time period.

In sophisticated systems, more advanced computational techniques like neural computing or artificial neural network techniques are implied, which are described in (McNeill 2004). The key aspects of these methods are highlighted in (Isis Canada 2004)

The major advantage of neural computing is automatically running data processing without human control required.

The data acquisition algorithm strongly affects the stored data volume and the type of diagnostic information. Hence, its accurate selection is one of the crucial aspects of SHM.

Storage of processed data

There are several techniques to collect data. Usually, only processed/analysed data are stored. With regard to their volume, raw data are usually disregarded. Nevertheless, this disallows them for interpretation at a later time. In order to plan adequate data storage, the following issues should be considered:

- the data should be available for a long period without susceptibility to corruption;
- there must be sufficient memory to store the data, especially in complex SHM systems providing a large amount of data;
- the data should be complete and kept in the order to use them again in the future;

Diagnostics

In this part, the collected, cleansed, and intelligently processed data are involved to further diagnosis. Its main objective is to obtain useful information about the response and the condition of the structure. The data analysis resulting in adequate conclusions should be supported by detailed knowledge about structural behaviour and its dependence on presence of damage, deterioration or other changes inside the structure. Generally, the complexity of analysis depends on the needs of monitoring program and SHM system components.

Retrieval of data

The data retrieval and the choice of techniques for it depend directly on a data amount, which is related to the type of test. For instance, in the static test, the volume of gained data is relatively small; therefore, they and the diagnostic information can be stored and designated for the retrieval. Unlike the static test, the dynamic test provides a large amount of data. In fact, only the diagnostic information is stored. The overarching goal of SHM is to provide detailed physical data to make rational and knowledge-based engineering decisions.

2.1.3 Types of tests in structural health monitoring

Static field testing

It is the most commonly used test for structural monitoring, whose beginning refers to early years of twentieth century. In general, its main objectives are: determine the load carrying capacity of a structure, provide data about structures behavior and its ability to sustain live loads. The early static field tests measured only deflection. Hence, the obtained data could be used only to determine the stiffness of bridge and its safety in the short term. Furthermore, long-term testing resulted in a small amount of information about the structure. Nevertheless, in recent years a progress in static field testing has been made. Unlike previously, current static field testing enables a wealth of information about the in-situ behavior of real structures.

- **behaviour tests**, whose main objective is to learn about mechanics of structural behaviour and to verify methods to analyse similar structures. Usually, the applied loading is less or equal to the maximal allowed service load on the structure. The results refer to the load distribution throughout the structure without any details about the load capacity of the individual structural components.
- **diagnostic tests** involve the same method to diagnose the structure but its results provide information about the response from single components. The results allow assessing the interaction between components, which generally can be detrimental or beneficial to the general behaviour. In fact, engineers can overtake adequate effort to fix detriments or utilize benefits. The diagnostic test is a useful tool to find a source of distress or to enhance the load-carrying capacity of a component.
- **proof load tests** are applied to estimate the load-carrying capacity of the structure by inducing proof loads on the structure. Proof load is defined as the maximum load of a given configuration that the structure has withstood without suffering any damage. It is usually of static type and its value is greater than the maximum service load. During the test, the load is increased progressively up to the limit of elastic behaviour of the structure. Nevertheless, there are several issues that need special care in order to obtain reliable test results, which are: correctness of calculations, the structure should be not damaged

by excessive loading, the structure should be continuously monitored during testing, and subjecting the structure to sufficient high proof load is not always confirmation of its load carrying capacity.

Dynamic field testing

Dynamic field testing is usually applied for when structures are subjected to moving dynamic loads e.g. moving vehicles through bridges. Hence, the most often monitored objects with this test are bridges this kind of test is mostly used to monitor bridges. In the dynamic field test, moving vehicles induced dynamic response of the bridge structure. The tests are run several times and the measurements are performed for various velocities of moving vehicles. The vehicles stimulate a dynamic load of structure by hitting a bump. In fact, they induce a dynamic response from the structure. There are four types of dynamic field testing, which are briefly discussed below:

- **stress history test** is applied to estimate the range of stresses that cause failures in bridges. This type of failures is called fatigue loading and is a result of repeated cycles of loading and unloading. The test requires a modern DAS, which exhibits capabilities to store large data amount, rapid sampling data, and to enable a continuous record of strain profiles in various instrumented structural components. The method relies on a strain profile analysis whose result is a range of strains experienced by components. Consequently, is possible to assess the fatigue life that is a time remaining for structure to fail by fatigue.
- **dynamic load allowance (DLA) tests** are used to determine the dynamic amplification factor, that allows to determine the maximum load experienced by the structure. For the design purposes, these loads are assumed as static. In reality, they are dynamic. Hence the result of calculation performed for static approach should be amplified by some factor, which is referred to the dynamic amplification factor. There are several techniques for its estimation and many factors affect it e.g. type and weight of moving vehicles.
- **ambient vibration test:** its main objective is to provide a complete and detailed profile of the vibrations experienced by

the bridge subjected to external stimuli, such as: wind, human activity and traffic. In some cases, through this analysis some information about structural damages and deterioration can be found. The use of vibration characteristic to identify damages is referred to as vibration damage detection (VBDD). In this type of tests, the accelerometers are usually used as sensors. Their positioning cannot be arbitrary to avoid undesired random errors. The sensors measure the vibration response of the structure, which determine its natural frequencies and the characteristic shapes of vibration (i.e. the mode shape). Based on this, sophisticated analysis technique provides information about damages. To avoid undesired random errors, special care should be taken about: appropriate and strategical positioning of sensors, their adequate number. In some case is reasonable to consider other vibration sources then the ambient. For instance, a controlled shaking by a hydraulic actuator could provide less variability in measurements that could be more appropriate for damage identification. Another problem to overcome is the typical ambient factors such as: temperature variations, normal changes to substrate conditions affected by structure ages or snow accumulations. Their impact is assumed more significant than the one of small-scale local damages.

- **pull back test is usually used** for bridges, but it is also applicable for other structures in which the response to lateral dynamic excitation has to be estimate. The gives the lateral vibration characteristic for bridges. This parameter cannot be determined on the results of the ambient vibration test, since normal traffic loads do not significantly excite a bridge in the lateral direction. The test involves a set of cables, which first pull the structure laterally and then they are suddenly released. The response from the structure is controlled by accelerometers and the data analysis looks the same as for ambient vibration tests.

Periodic monitoring

With respect to the timescale of monitoring, the test can be selected into two groups: periodic and continuous. The periodic monitoring refers to a time period like weeks, months or years. In this test, changes of

structural behaviour are detected and can be used to estimate damage or deterioration in the structure. There are several techniques involved into periodic monitoring such as:

- **monitoring through ambient vibrations**, which involve ambient vibrations caused by live or wind loads to examine the dynamic response from structure. Any changes in the vibration characteristics are treated as potentially caused by sensors can be permanently fixed to the structure at the place assumed as the ideal location, or temporarily installed at the surface for the time of testing.
- **bridge monitoring through testing under moving traffic refers to temporarily tracking structural changes**: this activity refers to periodic records of strain, performed for various components of structure. Based on the measurements there is possible to track changes in the structural behaviour. Moreover, changes of strain in various components enable to detect structural deteriorations and damages.
- **monitoring through static field testing**: with respect to high costs of the test, it is applied only for objects exhibiting innovative. Recently, this type of test was successfully involved to monitor the performance of highway bridges in Ontario. The novel approach in their design referred to incorporated innovative steel-free bridge deck systems.
- **monitoring crack growth**: it is usually applied for concrete structures that are able to develop cracks around places exposure to tensile forces. When concrete structure is intensively exploited, then the formation of cracks will stabilize and the structure becomes elastic. However, in case of progressive cracking, when its consequences may be more severe, there is need to monitor the progress and growth of cracking. Current tests with this method usually involve manual activities. Nevertheless, some efforts were overtaken to employ more advanced instruments such as acoustic emission systems and long-gauge FOSs.
- **periodic monitoring of repairs** performed before and after structural repairs is particularly significant to assess the effectiveness of repairs enhancing the stiffness of structure. This type of testing was successfully applied for reinforced concrete

structures, which were strengthened by introducing externally-bonded fibre reinforced polymer materials.

Continuous monitoring

As the name suggests, this type of monitoring refers to long-term investigations. This type of monitoring has only recently been used in full scale field applications, due to the higher costs and complexity of measurements. The obtained data are collected on site and remained for later, remote transfer for real-time monitoring and interpretation.

With respect to the high costs of this method, it is applied only for extremely important objects, being exposed to extreme events (e.g. severe earthquakes or hurricanes), or their design refers to unique concept without history of performance to prove its long-term safety (Isis Canada 2004).

2.1.4 Key aspects of SHM systems design

Structural health monitoring is a relatively new and a constantly evolving science. Hence there is no commonly accepted approach to design SHM systems. Nevertheless, there are some issues that should be respected and applied to design such systems. Figure 2.3 presents these issues grouped into three categories.

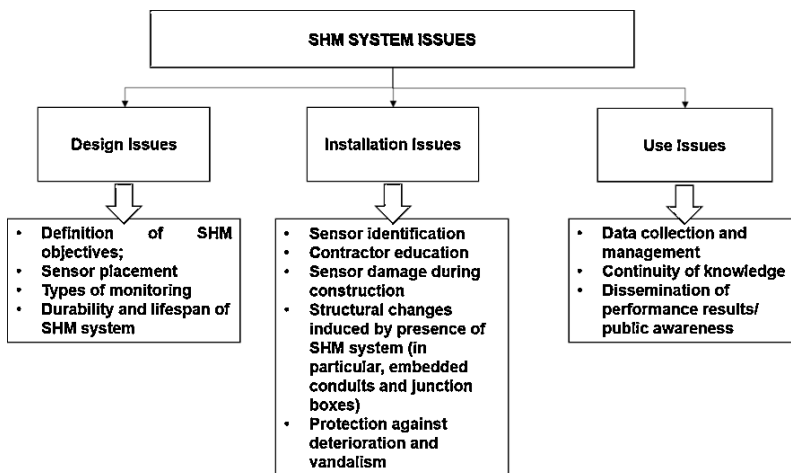


Figure 2.3. Main aspects of SHM systems design.

To design an adequate SHM system, there is need to determine the objective of investigation. Assuming that the SHM aims to diagnose the health condition of structure based on already existing damage, the following steps should be overtaken:

- determine the damage or deterioration mechanisms;
- determine the influence of damage/deterioration on the mechanical response of structure i.e. develop numerical and theoretical models of structure;
- establish (experimentally or theoretically) the characteristic response of key parameters such as strain, vibration and tilt, and their sensitivity to a certain level of deterioration;
- select the most sensitive parameter and determine the index that relates the change in response under services loads to the level of deterioration;
- design the monitoring system with respect to: a type of sensor, data acquisition, data management, data interpretation; these issues relate to type of monitoring i.e. static or dynamic, continuous or periodic, controlled loading or ambient loading;
- install the system and calibrate it with a baseline reading;
- assess field data and adapt the system as necessary.
- The above methodology assumes damage detection as the main objective of SHM. Nevertheless, this chapter show that structural health monitoring covers many other activities than those directly related to damage detection.
- To design an adequate SHM system, there is need to determine the objective of investigation. Assuming, the SHM aims to diagnose the health condition of structure based on already existing damage, following steps should be overtaken:
 - determine the damage or deterioration mechanisms,
 - determine the influence of damage/deterioration on the mechanical response of structure i.e. develop numerical and theoretical models of structure,
 - establish (experimentally or theoretically) the characteristic response of key parameters such as strain, vibration and tilt, and their sensitivity to an appropriate level of deterioration,
 - select the most sensitive parameter and determine the index that relates the change in response under services loads to the level of deterioration,

- design the monitoring system with respect to: a type of sensor, data acquisition, data management, data interpretation; these issues relate to type of monitoring i.e. static or dynamic, continuous or periodic, controlled loading or ambient loading.
- install the system and calibrate with a baseline reading,
- assess field data and adapt the system as necessary.

The above methodology assumes damage detection as main objective of SHM. Nevertheless, this chapter show that structural health monitoring covers many other activities than those directly related to damage detection.

2.2. Commercially available sensors

Sensing technologies incorporated into SHM system, are exploited to obtain complete information about the health condition of structures. Most sensors measure the parameters referring directly to deterioration or structural damages. Nevertheless, there is a group of sensors which provide complete information about a structure by measuring its physical and chemical parameters such as temperature, pH etc. They are called smart sensors. Additionally, smart sensors such as magnetorestrictive sensors and piezoelectric sensors can be used as actuators as well, this fact enhance the effectiveness of SHM systems. Furthermore, they are available in various sizes, hence they can be used even for remote and inaccessible places. On the other hand, fibre optic sensors (FOSs) are small, thus they do not influence the performances of the structures in which they are embedded. State of the art in sensing technologies for SHM and their progress are intensively discussed at annual meetings of International Workshops of SHM and European Workshops of SHM. Based on recent reports prepared in 1999 – 2014. P. Ferdinand resumed the progress in the sensing technology over last 35 years (Ferdinand 2014). Figure 2.4a shows two diagrams with the percentage of participation of various sensor technologies available on the market.

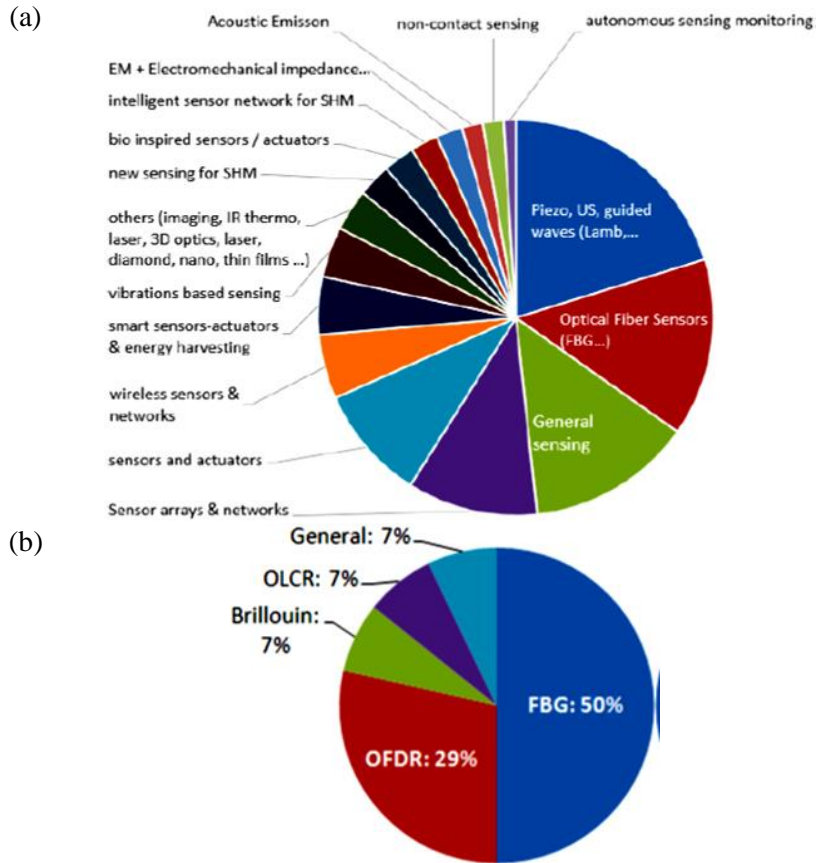


Figure 2.4. a) The contribution of various sensing technologies to the sensor market from IWSHM1999 to EWSHM 2014; b) OFS techniques available for SHM (EWSHM2014) (Ferdinand 2014).

The major impact (20%) comes from piezo, ultrasonic, guided waves sensors. The second position belongs to optical fibre sensors, whose impact amounts 15% of total market. The other sensing technologies hired for SHM are sensors arrays, wireless sensors, smart sensors, vibration-based sensors, bio-inspired sensors, etc. The number of published papers (12.7%) about optical fibre sensors confirms their importance for SHM. In Fig. 2.4 (b) it is shown that 50% of them refer to fibre Bragg grating (FBG) technology, another 29% relate to OFDR technology. The last 21% discuss the fibre optic sensing technology in general (7%), or refer to optical time domain reflectometry sensors

(OLCR), or distributed Brillouin optical time domain Analysers and reflectometers (BOTDA – BOTDR).

2.2.1 Fibre Optic Sensors (FOSS)

In the last fifty years a significant progress in theoretical studies on properties of optical fibres has been made, which was followed by their intensive applications in telecommunication and sensing technology. The application of optical fibres is desired where data transfer should be fast, secure and cost-effective. Optical fibres have several advantages among which one can list: they are immune to the electromagnetic interference (EMI), nonconductive, electrically passive, low loss, high bandwidth, small, lightweight, relatively low cost.

The standard optical fibre is made by the core which is surrounded by the cladding, which in turn is separated from the jacket (which is an external layer) by the buffer coating. The light is guided inside the core via total internal reflection, thanks to the higher refractive index contrast between the core and the cladding. The buffer coating protects from damage the cladding and the core, the latter one interacts directly with the light. This external layer varies in function of the desired protection. In fibre optic sensors the parameters such as polarization, frequency, phase and intensity, are sensitive to environmental conditions. Based on their variations, it is possible to determine precisely the stimulating factor.

The most commonly involved optical fibre technologies are Fabry-Perot interferometers, fibre Bragg gratings (FBG), and distributed sensors based on Rayleigh, Raman and Brillouin optical scattering. With respect to the modulated parameter involved to measure physical phenomena, the optical fibre technologies can be classified as following (National Instruments):

- Intensity
 - Attenuation of light
- Interferometric
 - Phase difference between two light waves (Sagnac, Michaelson, Mach-Zehnder)
- Resonant
 - Optical resonant frequency of on optical cavity (Fabry-Perot)
- Distributed

- Backscattering (Rayleigh, Raman, Brillouin)
- Polarimetric
 - Polarization state of light wave
- Spectral Interference
 - Frequency of light wave interfering with a periodic structure (fibre Bragg grating)

Regarding the configuration, fibre optic sensors can be classified as single – point, multi – point, or distributed sensors. A single – point sensor has one sensing point, which is usually localized at the tip. Multi-point FOSs possess at least two sensing regions distributed along the length of fibre. The size of sensing areas, as well as the density of their distribution, depends on application, i.e. the distance between sensing regions may vary from few millimetres to several meters. Distributed systems exploit the whole length of fibres (up to several tens of kilometres). The general information about the four major fibre optic sensing technologies are resumed in Table 2.1.

Table 2.1. Comparison between four major fibre optic sensing technologies. Based on (National Instruments)

Technology	Topology	Range	Temperature	Strain	Pressure	Vibration
Fabry-Perot	Single-Point	<10km	Yes	Yes	Yes	Yes
FBG	Multi-Point	<50km	Yes	Yes	Yes	Yes
Rayleigh	Distributed	<70km	Yes	Yes	No	No
Raman	Distributed	<20km	Yes	No	No	No
Brillouin	Distributed	<50km	Yes	Yes	No	No

Distributed fibre optic sensors

The concept of distributed sensing appeared in 1980. It relies on measuring the scattered light at every location along the fibre. There are three types of scattering supporting distributed sensing i.e. Rayleigh, Raman, and Brillouin scattering.

Rayleigh scattering is the most commonly used. It is caused by fluctuations in material, which appeared during fabrication. In case of light, whose narrow pulse is introduced into the fibre, the Rayleigh backscattering appears because of variation in the refractive index of core. This effect is relatively sensitive for temperature. Hence, it is used for temperature detection, as well as strain sensing. It is effective up to

70 m of distance. It is considered as a promising and emerging technology.

Another type of scattering is Raman scattering, which is caused by molecular vibration of glass fibre stimulated by an incident light. The scattered light as two components which propagate into two different directions with respect to the initial light pulse. These components are called Stokes and anti-Stokes. The ratio between the components allows temperature sensing and it is immune to strain. This technology is intensively employed in oil and gas industries for collecting temperature variations in oil wells.

The last, third type of scattering is called Brillouin and it is stimulated by acoustic vibrations resulted by incident light. Because of energy conservation, there is a phase shift between original light pulse and the scattered response. This shift is sensitive to temperature and stress variations. Since these effects are difficult to differentiate, a possible solution could be the combination of Brillouin scattering with other effect such as Raman scattering or FBG (National Instruments).

Fabry – Perot interferometric sensors

The basic components of Fabry – Perot interferometer are mirrors that are parallel to each other and separated by the cavity, as shown in Fig.2.5. In the intrinsic fibre Fabry-Perot interferometric (FFPI) sensor the mirrors are separated by a segment of a single – mode fibre, whereas an extrinsic Fabry - Perot interferometric (EFPI) sensor possesses an air gap between the mirrors. Multiple beams of light interfere with each other inside the cavity and this produces an optical spectrum. The spacing between the peaks of the spectrum changes with the distance between the mirrors, which is affected by external factors. In the output signal sinusoidal modulation occur, whose amplitude decreases with the increasing distance between mirrors.

Thanks to its high sensitivity, the extrinsic EFPI sensors are perfect to measure various physical quantities relating to micro displacement. Fabry – Perot interferometer sensors are of single-point type and are applied to measure temperature and pressure. Their applications in medicine or as pressure transducers are possible thanks to their compact size and relative simplicity.

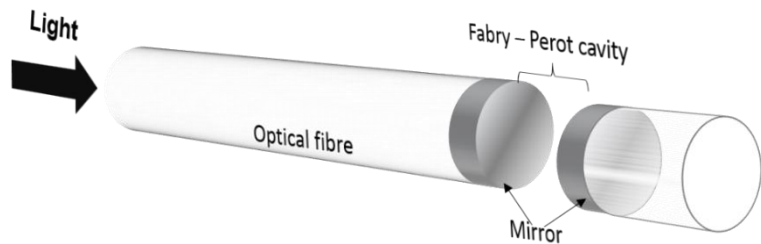


Figure 2.5. Basic configuration of Fabry – Perot interferometer sensor. Based on (National Instruments).

Fibre Bragg Gratings sensors

Fibre Bragg gratings sensors are systems that show a shift of reflected wavelength in response of temperature and strain. Since 1978, when the first sensor of this type was invented, their technology has been being intensively developed; hence they have gained many applications in the telecommunications industry for dense wavelength division multiplexing, dispersion compensation, laser stabilization.

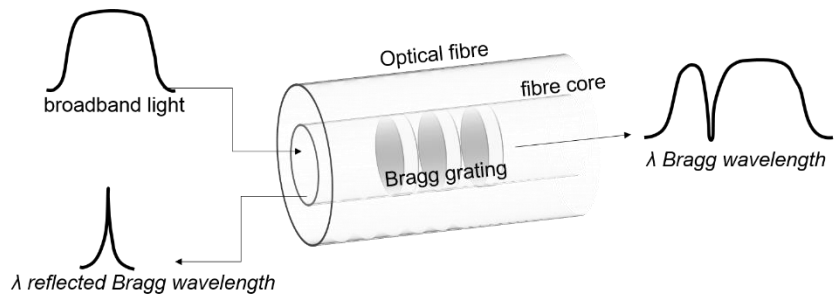


Figure 2.6. Operation of optical FBG sensor. Based on (National Instruments).

A FBG is a wavelength-dependent optical filter/reflector created inside a fibre core. It possesses a periodic composition of layers with different refractive indices. When a broadband light is introduced into the core, then the reflections at each layer interfere with each other constructively only with the Bragg wavelength. This wavelength corresponds to twice the grating period. The reflected signal is a narrowband signal with the peak referring to the Bragg wavelength. Figure 2.6 shows the mechanism of filtration by the FBG. Any external factor that is able to change the grating period, such as temperature, strain etc., results in a

shift of Bragg wavelength ($\Delta\lambda_B$). Then, its value is converted by the interrogator into strain with regard to following relationship (Maheshwari et al. 2017):

$$\varepsilon = \frac{\Delta\lambda_B}{a} \quad (2.1)$$

Where ε refers to strain, $\Delta\lambda_B$ is the shift of Bragg wavelength and is the wavelength-strain sensitive factor, whose value is $0.67\mu\varepsilon$ -1pm for 850 nm.

Their capabilities to detect variations in temperature, pressure or strain, coupled with their physical features, such as light weight, flexibility, make them a perfect sensor for SHM. In addition, the current FBG sensors are available as multi-point and single-point sensing arrays, which can be substitute for electrical sensors.

Benefits of FBG optical sensing

The major benefits of optical sensing are: nonconductive, electrically passive, immune to EMI, lightweight, and noncorrosive. Its mean, they can be use both with high voltage, high sources of electromagnetic interference, and in explosive environments (National Instruments).

In particular, FBG sensors can be an alternative for conventional electrical sensors.

Unlike them (e.g. conventional electrical foil strain gages), FBG optical sensors are very stable, what makes them accurate to perform measurements in long-term SHM. Furthermore, FBG can interrogate systems over long distances, employing powerful lasers and low-losses fibre arrays. Their temperature resolution is around 0.1°C , and strain resolution is equal approximately to 0.7.

2.2.2 Piezoelectric sensors

Piezoelectric sensors are based on the piezoelectric effect, meaning the linear electromechanical interaction between the mechanical and the electrical state in crystals without a centre of symmetry.

There are two types of piezoelectric effect: the direct and the converse. In the direct piezoelectric effect, the deformation of piezoelectric material induces a proportional change in electric polarization of the material, i.e. the electrical charge appears at both opposite faced of mechanically loaded medium. The converse piezoelectric effect is when

piezoelectric medium is placed externally to the electrical field and it is deformed by the applied electrical voltage.

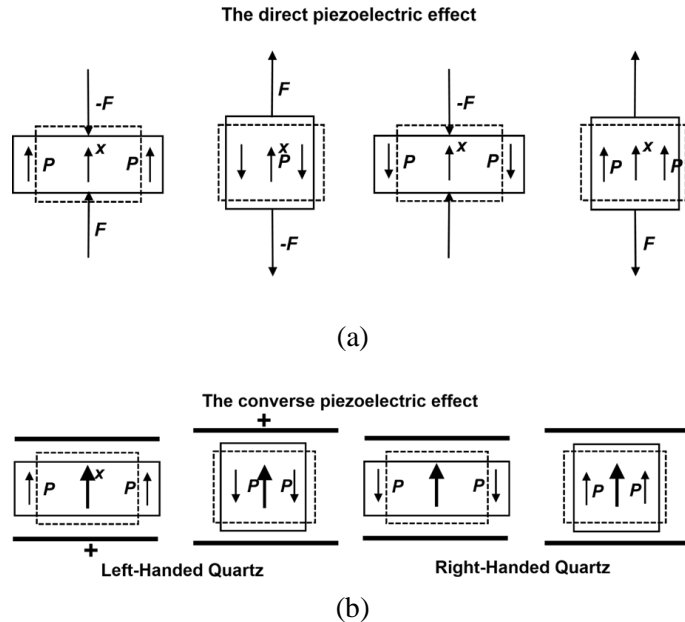


Figure 2.7. Schematic representation of piezoelectric effect in an X-quartz plate. (Gautschi 2002).

Both effects are shown in Fig.2.7. As experimental medium, it was used a quartz plate cut normal to the crystallographic x -axis (X -quartz plate). In the direct effect, the applied external force F induces the electric polarization P , whereas in the converse case, the external electrical field E deforms the piezoelectric sample, which was placed inside it.

There are two methods of SHM that exploit the capabilities of piezoelectric sensors. The first one refers to measurements of variations in electrical impedance of piezoelectric transducer (PZT). It is placed in the electrical field that stimulate small deformation within its waver and in the structure on which it is attached. The mechanical response from the structure is transferred back to the transducer, changing its electrical response. Hence, any structural damages and deteriorations are detectable by monitoring the electrical impedance of PZT. Comparing with the next method, the electrical impedance-based technique exhibits local applicability i.e. it is suitable to monitor small areas. The local character of measurements with piezoelectric sensors was confirmed by Ayres et al. (Ayres et al. 1998), and Park et al. (Park et al. 2006). Unlike

Ayres et al., Park et al. combined the electric impedance-based method with Lamb wave method. This approach allowed to detect not only structural damages, but also provides information about the influence of the temperature. Moreover, they developed a compensation technique to minimise the effects of temperature on impedance measurement. It was based on the reconstruction of the damage metric, which minimised the impedance drifts due to temperature. Other tested methods allow determining damage characterization based on structural parameters. For instance, Lim et al. (Lim, Bhalla and Soh 2006) estimated the parameters such as stiffness, mass, and damper by measuring the admittance signature, whereas Wen et al. (Wen et al. 2007) investigated the influence of temperature and stress on concrete structure and various parameters of PZT such as the static compliance, the static resistance, dynamic compliance etc.

The impedance-based method has involved self-sensing actuator concept. Here, a piezoelectric transducer works as a sensor and an actuator, as well. Its main advantage refers to its qualitative nature; hence, any background knowledge is needed to interpret the results (Sun, Staszewski and Swamy 2010). It is sensitive to stimulation provided by local area, and insensitive to far-field changes in loading and boundary conditions. Nevertheless, this method does not provide any information about the origin of structural damages (i.e. various damages such as corrosion, delamination will affect the impedance similarly). Hence, this method should be used with the assistance of other quantitative method to obtain complete information about a structural damage.

The elastic-based method relies on monitoring the parameters of mechanical waves (longitudinal and transversal one) in a damaged structure. Several experiments confirmed the reliability of this method. Wu and Chang (Wu and Chang 2001) used ultrasonic waves to detect structure defects. Their test referred to the debonding between the reinforcing bar and concrete. Its results showed that the amplitude of received signal increased in a linearly proportional manner to the debonding size. Furthermore, numerical investigations showed that cracks do not influence the output signal. Nevertheless, when cracks and a debonding damage exist in the structure, then a debonding damage dominated the output signals.

Sun et al. (Sun, Staszewski, Swamy and Li et al. 2008) showed that any damages in the structure can be detected by using PZT patches to induce

and receive Rayleigh waves propagating along the surface of the structure and longitudinal waves (meaning shear waves) propagating through internal concrete. Based on the measurements of Rayleigh waves velocity, they calculated the dynamic elastic modulus and the dynamic Poisson's ratio of concrete. Difference in amplitudes of induced and received waves were highly sensitive to the cracking process in concrete.

In opposition to the electric impedance-based method, the elastic wave-based method can monitor larger areas. Moreover, the elastic wave approach provides more information about wave propagation in order to identify damages, i.e. amplitude and phase of the transfer function, shift in frequencies, amplitude and the arrival time.

Both methods represent active approach for sensing, whereas most of sensing methods in SHM relate to passive sensor measurements to determine changes in the conditions or environment of the structure (Sun, Staszewski and Swamy 2010).

2.2.3 Self-diagnosing fibre reinforced composites

Self-diagnosing fibre reinforced composites are composition of electrical conductive phase (i.e. carbon fibre) embedded in a matrix of cement or polymer. They exhibit capabilities to monitor their own strain, damage and temperature. Table 2.1. shows the most common types of composites listed with their components.

Table 2.2. The commonly used self-diagnosing fibre reinforced composites with their phase and matrix components. Based on (Sun, Staszewski and Swamy 2010).

Composite	Electrical conductive phase (with its volume content, and length, l)	Matrix component
Carbon fibre, reinforced concrete (CFRC)	Short carbon fibre ($l < 10\text{mm}$, $< 0.5\%$)	Cement, mortar, concrete including admixtures (methylcellulose, silica fume et al.)

Carbon fibre, reinforced polymer (CFRP)	Short carbon fibre ($l < 10\text{mm}$, 10%) Continuous carbon fibre (58%)	Resin, curing agent
Carbon fibre glass fibre reinforced polymer (CFGFRP)	Continuous carbon fibre ($<0.5\%$)	Resin, curing agent
Carbon powder dispersed in glass-fibre-reinforced plastics (CPGFRP)	Graphite carbon powders (0.15%, average particle diameter = $5\mu\text{m}$)	Resin, curing agent
Hybrid carbon fibre reinforced polymer (HCFRP) sensors	High modulus (HM), medium modulus (MM), high-strength (HS) carbon tows	Resin, curing agent

Many papers refer to investigations on strain-sensitive parameters of self-diagnosing fibre reinforced composites. For instance, Cheng and Chung showed (Chen and Chung 1993), (Chen and Chung 1995), that (CFRC) exhibits sensitivity to strain and damage by changing its electrical resistance. They involved sample with dimension of $(5.1 \times 5.1 \times 5.1)$ cm in which there are included short carbon fibres with the volume ratio of 0.24%. The measurements were performed step by step. Initially, the ratio $\Delta R/R_0$ increased irreversibly because of the wreaking of fibre-matrix interface. In the next steps, the ratio decreased reversibly due to the push-in of the fibres, whereas at the unloading conditions, the fibres were pushed out. Similar properties to CFRC exhibit CFRP, as was confirmed by (Chung 1998).

The investigations on CFRC resistance variation during elongation were followed by Mao et al., who introduced selection into three stages: reversible sensing stage, balancing stage (the resistance hardly changes in this phase), and rapidly increasing stage, which corresponded to different phases of crack development in CFRC during loading (Mao et al. 1996). Another trend in research on CFRC strain-sensitivity was initiated by Mingqing et al. They gave insights on temperature sensing by CFRC and on the cement-based thermoelectric materials.

Other investigations on CFRC strain sensitivity were overtaken by Wen and Chung, who developed CFRC coating material. The measurements of the resistance of CFRC-coating at loading conditions showed higher sensitivity of reinforced concrete beam to stress and fatigue damage. Similar application was tested for CFRP (Wang and Chung 1998). Unfortunately, it is useless for practical applications because of its low sensitivity to strain. The “non-destructive” range referred to 0 – 420 $\mu\epsilon$ in tension, and 0 – 1100 $\mu\epsilon$ in compression. Exceeding these limits caused damages in the coating.

CFGFRP was designed as a hybrid composition of two types of fibres: glass and carbon (Sun, Staszewski and Swamy 2009). Unlike conductive carbon fibres, the insulating glass fibres exhibit large ultimate elongation value. Hence, during elongation, the significant change in its resistance is resulted by the failure of carbon tows. Nevertheless, this doesn't affect the elongation capabilities of composition because of glass fibres. Hence, their possible applications relate to monitor high values of strain by use of carbon with different ultimate elongation values, or to give early-warnings of catastrophic failure of structures (Sun, Staszewski and Swamy 2010). In reality, CFGFRP have gained applications as prevention systems in security walls to detect and prevent burglaries.

The Major disadvantages of CFGFRP refer to its material properties and fabrication aspects. Their strain-sensitivity is very low in the range from zero to the failure of carbon fibres. Hence, they are useless for strain monitoring in the small or medium strain range. Moreover, their fabrication costs are high hence an industrial production is difficult to achieve.

One advantage of self-diagnose fibre reinforced composites is that they are structure and sensors as well. CFGFRP and CPGFRP are used as reinforcing components in concrete. CFRC involves small volume of short fibres, which exhibit higher stiffness, an increased tensile strength and a lower drying shrinkage than plane concrete.

There are many aspects of self-diagnosing fibre reinforced materials that should be developed or improved. One of them is the use of CPGFRP and HCFRP, which are more sensitive than CFGFRP. There are many factors that influence the sensing repeatability, such as (Sun, Staszewski and Swamy 2009):

- distribution state of conductive material;

- changes of electrical resistance caused by temperature variations, moisture, and transversal effect;
- irreversible increase of resistance caused by damages in sensing materials, and interfaces during cyclic loading;
- methods of preparation of the composites and resistance measurements.

However, the use of only one type of smart sensors is not sufficient to obtain complete information about damages in the structure (Maheshwari et al. 2017). One of the possible solutions was proposed by Maheshwari et al. (Maheshwari et al. 2017) who involved a combination of three types of smart sensors: a fibre Bragg grating sensor, fibre-optic polarimetric sensor (Fig. 2.8).

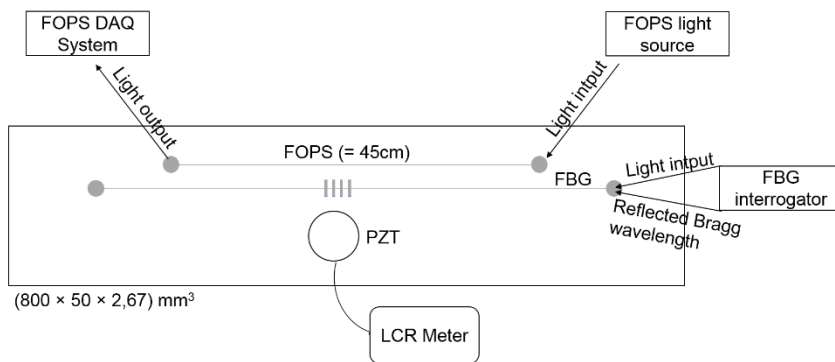


Figure 2.8. The cross-section of the sample (the aluminum beam) with arrangement of smart sensors inside. Based on (Maheshwari et al. 2017).

Each sensor had its own instrumentation system i.e. FBG was supported by the interrogator coupled with the light source, for FOPS the DAQ system and the light source were separate devices, whereas PZT signal was displayed by LCR meter. The beam was fixed at both its edges and it was loaded in the middle. The complete test setup is depicted in Fig.2.9

The novel optical systems deliver extensometric information about deformed surfaces (Grédiac 2004). This approach corresponds to the morphology characterization of materials. Hence, their methodology refers to three subsequent actions

- Record the 2D image of 3D object;
- Display the image;
- Computation of mechanical parameters based on images.

The principal classification for optical techniques groups the optical techniques into two categories: geometrical methods (moiré, grid methods, digital image correlations method), and interferometric methods (holography, moiré interferometry, the electronic speckle pattern interferometry (ESPI)). M. Grédiac proposed another selection of full-field optical techniques for structure characterization. In the first step, all full-field techniques are divided into two groups with respect to the measured effectuated, i.e. displacement and strain. In the second step, the displacement methods and the strain methods are classified with respect to the applied techniques as interferometric or non-interferometric methods. In case of displacement techniques, the non-interferometric methods are: spackle photography, image correlation, geometric moiré, and grid method. The second subcategory refers to Moiré interferometry and electronic speckle pattern interferometry.

The strain field can be calculated by applying an appropriate algorithm for the results obtained by the displacement techniques, or by direct measurements involving e.g. shearography (Templeton 1987; Bulhak and Surrel 1999), speckle shearing photography (Rastogi 1998), moiré fringes shifting (Wasowski and Wasowski 1987) This classification is depicted schematically in Fig. 2.10.

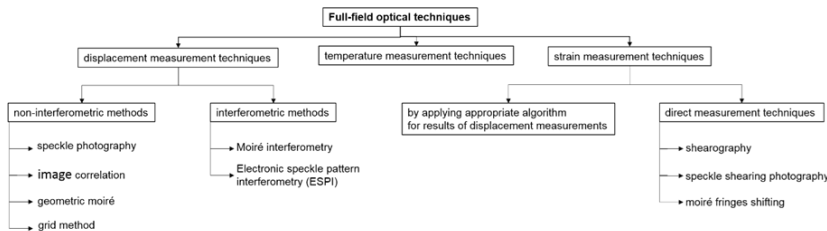


Figure 2.10. The classification of full field optical techniques proposed by M. Grédiac. One of the possible ways to measure the temperature field provides an infrared camera. This method was

substantially described in (Bakis 1987) (Heller 1988) (Rauch 1993).

Grid method

In this technique, the basic tool is the simplest type of diffraction grating, meaning the one with one-dimensional periodicity. The periodic structure consists of straight, parallel lines distributed with equal distance (also called the pitch of grating, p) between two adjacent lines exhibiting the maximal intensity. This grating is attached to the investigated sample by engraving, painting or bonding. It works as a “spatial carrier” (Vautrin et al.), meaning that its phase ($\phi(r)$) is modulated by the displacement field. The relation between both values is defined by:

$$\phi(\mathbf{r}) = 2\pi \frac{u_x(\mathbf{r})}{p} \quad (2.2)$$

Here, u_x is the displacement in the perpendicular plane to the grid lines, and r determines the location of this component.

The typical parameters of grating used in the grid method are: for the pitch the value of 0.5 mm, and for the phase resolution is $\frac{2\pi}{100}$. For these values, the resolution of displacement measurements achieves 5 μm .

Digital image correlation (DIC)

Digital image correlation is a geometrical full-field optical method to measure displacement at the surface of the structure. The two approaches to perform the measurements are two- and three-dimensional.

The main idea of two-dimensional measurements is to match one point at the image of surface, taken for unloaded sample, to a point at the image of the surface after loading. Hence, an accurate point-to-point mapping from image of unloaded object to the image taken after loading allows measuring the displacement of surface. This approach requires the fulfilment of two requirements:

- the surface must have a pattern with the varying intensity;
- the imaging camera should be positioned in a proper way in order to have the sensor plane parallel to the monitored surface.

The imaging process of camera converts the continuous intensity field reflected in the sample surface into a discrete field of intensity level.

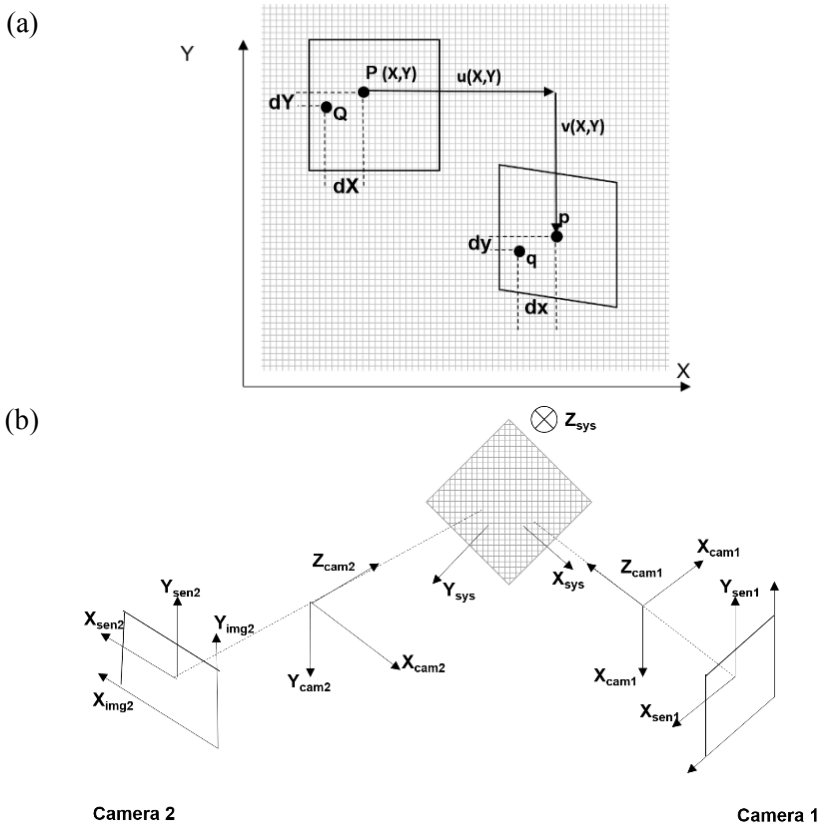


Figure 2.11. a) The scheme of deformation in two dimensions; b) Image creation of object in three-dimensional measurements (Sutton et al. 1999).

The three-dimensional measurements refer to a simple “binocular vision model” (Sutton et al. 1999), which is similar to human depth perception. These measurements involve two cameras, which take images of investigated surface. By comparing the images of corresponding subsets in images of object surface, there is possible to determine the surface shape. Moreover, comparing the subset in images taken before, and after loading the specimen, there is possible to measure the displacement caused by loading. Nevertheless, both measurements require detailed information about position and operating characteristics of involved cameras.

The characteristic involves the *extrinsic* and *intrinsic parameters* of both cameras. From the point of view of methodology, more important are the extrinsic parameters ($\alpha, \beta, \gamma, X_0, Y_0, Z_0$) which determine the setup

arrangement by position and orientation of cameras.

Figure 2.11b shows the sample arrangement of experimental setup, it reports the notation used for the calculations that relate the image parameters and the object parameters.

Interferometric moiré

The principles of this technique refer to the wave theory of diffraction. As in the grid method, the grating is moulded to the surface. Its typical pitch is equal to $p = 1200/\text{mm}$. Then, the grating area is illuminated by two symmetric oblique collimated beams, which interfere with each other on the screen, where the image of grating area is created. Fig. 2.12 shows the experimental setup.

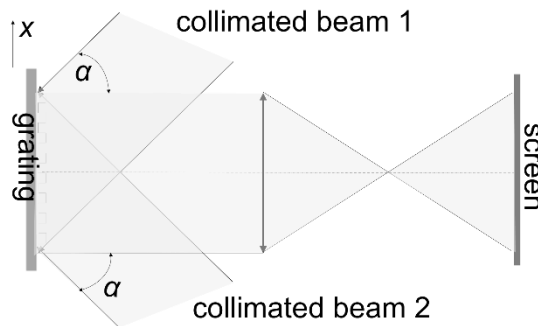


Figure 2.12. The experimental setup to measure displacement with the interferometric moiré method. (Vautrin et al.)

The variation of phase in the fringe pattern, stimulated by an applied loading can be estimated by:

$$\phi(\mathbf{r}) = \frac{4\pi}{p} u_x(\mathbf{r}) \quad (2.3)$$

Electronic speckle pattern interferometry (ESPI)

Electronic speckle interferometry can be considered as “video equivalent of holographic interferometry”. It provides complete information about the surface displacement by all the three coordinates: out-of-plane (z), and in-plane (x, y). The main concept of *ESPI* refers to the relationship between fringe pattern and surface motion. This relationship is determined by the *fringe function*, which depends on the

illumination and the optical configuration of the interferometer. The typical two-beam interferometry allows measuring the sensitive vector (depending on the geometry of interferometer) for displacements in one direction. Hence, to obtain information about displacements in all three directions it requires three sets of data. The solution of the set refers to the displacement in three-dimensional space. The error of such calculations depends on the spatial separation of sensitive vectors, and its minimal value refers to the mutually orthogonal vectors.

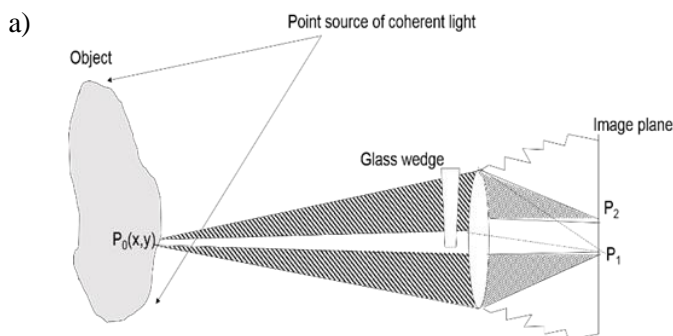
The fringe function relates to the phase change, $\Delta\phi$, which can be expressed by:

$$\phi = k\Gamma d_n \quad (2.4)$$

Here, k is the fringe numbers, Γ is a fringe sensitivity factor (determining how many fringes correspond to a given surface displacement), d_n is the component of object displacement along the sensitivity vector \mathbf{n} . Γ and \mathbf{n} depend on the geometry of interferometer which is different for measurements of in-plane sensitivity and out-of-plane sensitivity (Tyrer 1997).

Shearography

Shearography (or speckle shearing interferometry) is a laser optical method, which was originally developed for strain measurements. It is also applicable to measure displacements or the slope of a surface, which enables to compute the surface strain by differentiating the displacements data. However, numerical differentiation is laborious and prone to large errors. There are two types of shearography: photography and digital. The experimental setups of both are depicted in Fig.2.13.



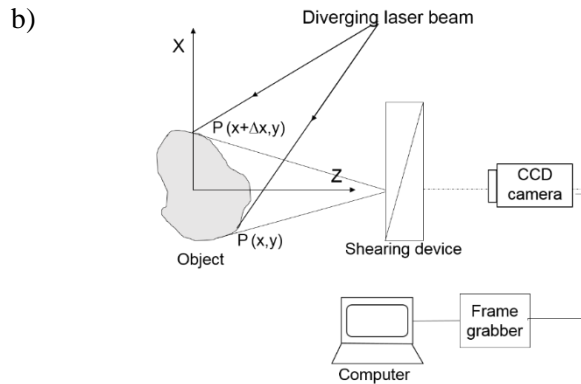


Figure 2.13. The schematic diagram of a) photography shearography; b) digital shearography. (Hung 1996)

In the photographic shearography, the coherent light is provided by a point source. The light beam illuminates the object whose image is created by an image-shearing camera equipped with a shearing device e.g. a small angle glass wedge. The image-shearing camera creates a couple of laterally sheared images in image plane, which interferes with each other creating a speckle pattern. The pattern is slightly modified when the object is deformed. The superposition of two speckle patterns (for deformed and non-deformed objects) results in a fringe pattern depicts the derivatives of the surface displacements.

The main drawbacks of photographic shearography are the high costs of photographic recording and long-time processing of the photographic film. However, it provides high-quality fringe patterns compared to digital shearography.

The digital shearography is a computerized process, which eliminates the steps as photographic recording and wet processing that are integral parts of photography shearography. The sample is illuminated by coherent light beam, which is generated by a point source. Its image is created by an image-shearing camera. The shearing device is the birefringent crystal that provides two non-parallel beams scattered from two different points on the object surface as collinear or nearly collinear. In fact, the spatial frequency of the speckle pattern is very low, thus resolvable by CCD camera.

The digital shearography can be performed by a modified Michelson shearing interferometer, which employs a frame grabber to digitize the speckle pattern. The fringe pattern is created as the difference between

two speckle patterns and displayed on monitor. The major advantage of this approach is that the final results are displayed in near real time.

Shearography seems to be more practical than holography in non-destructive evaluation, for the following reasons:

- unlike holography that measures displacements, shearography measures strains;
- holography requires an isolation from vibration because they affect significantly the results, whereas shearography is insensitive to that motion;
- the experimental setup for shearography is quite simple;
- shearography provide wider and more controllable range of sensitivity, thus it allows to measure larger deformation.

Full field optical techniques are attractive methods to analyse a heterogeneous and anisotropic structure of composite materials. Nevertheless, they are not applicable without any supporting of numerical methods to analyse results of measurements. However, this fact doesn't exclude these techniques from applications which require compact measurement. It has been experimentally confirmed and reported in (Newman 1991) (Ettermeyer and Honlet 1994) (Ettermeyer, Wang and Walz 1997) (Walz and Ettemeyer 1998). In the list below one can find the recent application of these methods ordered with regard to the increasing connection between measurements and modelling (Grédiac 2004):

- **non-destructive testing and inspections (Waldner 1996) (Ettermeyer 1994) (Hetwig 1997)**; Full field techniques are particularly valuable to detect structural defects. In composite materials, the defects are results of fabrication process or (e.g. delamination) or intensive, long-time exploitation (microcracks, impacts, damages). Waldner used ESPI and shearography to detect hidden damages in a sandwich composite material. He found that the defects induced strain concentration, which was detectable by fringes nearing each other. The same approach was applied to find influence of paint removing from a sandwich part with a strong pulsed laser.
- **experimental evidence of local gradients due to material heterogeneities** is very important for composite materials, or any other exhibiting a structural anisotropy and heterogeneity.

Hence, the strain/ displacement field is non-uniform in their whole volume. The local value of strain can differ from the average value with respect to different components. There are numerous examples of the application of full-field optical techniques to determine strain/displacement field, or to find structural effects, e.g. failure mechanisms in laminates (Xing, Yun and Dai 1999), tension and bending coupling effects in the wrap and fill yarns (Bulhak and Surrel 1999), curved surfaces (Mollenhauer 1997) (Mollenhauer and Reifsnider 2000) (Boeman 1991). The typical full field optical methods used for this and other applications are the grating shearography method (Bulhak and Surrel 1999, Vautrin et al. 2002) and the moiré interferometry (Xing, Yun and Dai 1999)

- **cracking characterization** is obtained by analysing singularities in a displacement field. The measurements involve grid methods or the image intercorrelation technique, which provide results with the order of micrometres. The results provide information about the width and profile of cracks. Hence, they can be used to determine a model of mechanical response of structure (Avril et al. 2004). Full-field optical techniques are particularly valuable to detect multicracking of brittle materials. It was confirmed by investigations on cement-based composites willsteel fibres.
- **verifications of boundary conditions**
- **verification of assumptions under which theoretical or numerical models are built;**
- **validation of models;**
- **identification of constitutive parameters;**

The applications described above of non-destructive optical techniques refer to experimental determination of displacement, stress/strain field. However, the main objective of the measurements is to derive the parameters of constitutive equations of materials based on their results. In case of composite materials, it is a difficult task. Now a day, loading conditions and geometry of sample are referred to a homogenous strain/stress field. Hence, the measurements provide the unknown parameters directly. Nevertheless, there are still some inaccuracies due to:

- the anisotropy and heterogeneity that could be at different scales

in composite materials;

- the number of unknown parameters which influence the number of mechanical tests;
- the fabrication process strongly affects the properties of product.:

Hence, there is desired to apply an adequate numerical method to solve the problem. In case of composite materials, the calculation of constitutive parameters with the known sample geometry, the resulting force, F , and the type of constitutive equations, refers to the inverse problem.

There are two numerical methods recommended for these types of problems: updating finite element models, and the virtual fields method.

Updating finite element models

This method was developed for problems that need a direct method to be solved, but it is also applicable for the inverse one by involving iterative methods. Nevertheless, iterative computations increase the computational time significantly. This method is a combination of experimental and numerical approach. The first step concerns the calculation of the displacements at each node and the values of constitutive parameters are needed. The numerical results are compared with their experimental counterparts. The difference is assessed by applying the objective function, which is the sum of squared differences between numerical and experimental data. Hence, the main concept of this approach is to minimize iteratively this estimation with respect to the constitutive parameters.

The main drawbacks of this model are:

- its procedure is ‘numerical black box’ (Grédiac 2004), i.e. its basic tool, such as the objective function and initial data are estimated to satisfy suitable conditions;
- is time-consuming;
- the choice of suitable boundary conditions.

Nevertheless, there are some successful examples of its applications:

- Allix and Vidal developed the method called LATIN to reduce the number of iterations and improve their quality (Allix and Vidal 2002);
- LeMagorou et al. optimized loading conditions, including location of applied forces, to determine the constitutive

parameters of the elastic response of wooden plates under loading (LeMagorou, Bos and Rouger 2002);

- Meuwissen used this model to determine the plastic response of some metals (it was applied with the assistance of image correlation technique) (Meuwissen 1998)

The virtual fields method

Unlike the previous method, this one is a direct method, which requires no iterative techniques in any cases at all. Its main idea is to write the principle of virtual work with different and independent virtual fields. This lead to the system with number of equations equal to number of constitutive parameters, which are the only unknown variables. Hence, the unknown parameters can be estimated directly after inversion of system. This approach was successfully applied in many cases described in (Grédiac et al. 1998; Pierron and Grédiac 2000; Pierron, Zhavaronok and Grédiac 2000; Grédiac, Auslender and Pierron 2001; Grédiac, Toussaint, Pierron 2002).

Its main advantages are:

- the directness in many cases (no iterative techniques required, shorter time for calculations);
- the problem can be simplified by introducing virtual fields with virtual work of the resulting forces.

Nevertheless, there is one limitation for this approach, which corresponds with the reduced number of results in non-linear case.

Huke et al. (Huke et al. 2013) proposed another selection, which refers to optical non-destructive techniques (ONDT) (Fig. 2.14). Optical non-destructive techniques are one of the non-destructive testing methods, despite of mechanical, x-ray, and electrical techniques. The appropriate ONDT is selected with respect to the material properties and optical appearance of probe (26). The accurately selected ONDT must be able to measure structural properties in a resolution sufficient for a qualifying decision.

In Fig. 2.14, Huke *et al.* introduce two categories of ONDT: passive and active

The passive methods involve any optical techniques providing signal related to properties of examined object, for instance ellipsometry, reflectometry, photogrammetry, interferometry, etc. (Savio, De Chiffre and Schmitt 2007; Chen, Brown, and Song 2000; Osten 2008). In the

next step, the passive methods can be divided into two subcategories: the surface related methods and look through methods.

The active methods are a combination of optical passive techniques with a certain load to excite a signal related to the structural properties. As shown in Fig. 2.11., there are two subcategories of active methods: time-/depth resolved methods and integrating methods.

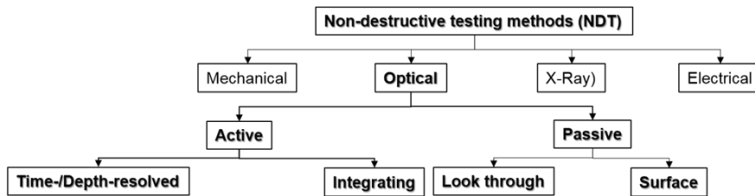


Figure 2.14. The general selection of optical non-destructive techniques, introduced by Huke et al. (Huke et al. 2013).

Time-/depth resolved methods

The typical method for this class is time-gated and phase-resolved thermography involving various methods of wave excitation. With respect to the excitation method, there are distinguished three types of thermography: optical- (OLT), ultrasound-(ULT), induction-(ILT)lock-in thermography. In general, these methods apply two types of loading: elastic and thermoelastic waves. The response from the structure is detected by a Doppler-vibrometry or a designed Fabry-Perot cavity. There are two factors influence the resolution of measurements: the measurable time steps, which should be enough small and the wavelength of excited ultrasounds induced by piezoelectric crystal or short-pulsed high-power laser. The mechanism of ultrasounds generation by a (pump-) laser is depicted in Fig. 2.15.

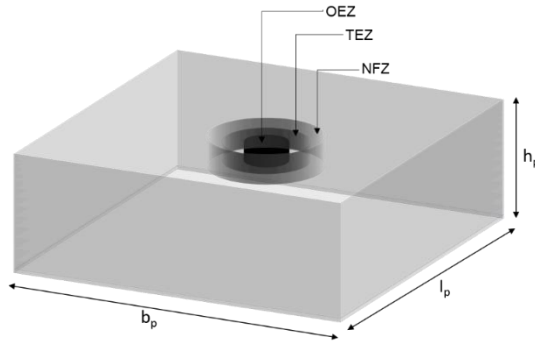


Figure 2.15. Laser – material interaction (Huke et al. 2013).

The propagating laser pulse produces an optical penetration zone (OEZ), which induces the thermoelastic zone (TEZ). The exiting ultrasounds can be divided into two types of the near-field zone (NFZ), and the far-field zone ultrasounds, with respect to the range of their expansion.

Propagating through the structure ultrasounds can be generated by short-pulsed high-power laser with sufficient absorption in the material. The absorbed energy of the pump-laser induces a thermoelastic stress-zone (Fig.2.13). Here, the energy dissipates in various directions, through thermal stresses as well as ultrasound waves, depending on material parameters, laser parameters and excited frequencies (Scruby and Drain 1990) (Zhang, Ying and Shen 1997) (Dubois et al. 2000). In general, the excitation is a broad band signal. Thus, it can be applied to detect larger defects or to perform thickness measurements. Nevertheless, thanks to tunability of (probe-)laser, there is reasonable to excite narrow-band signals to detect smaller defects in multi-layered structures (Shi et al. 2012; Stepinski and Johnsson 2004; Stratoudaki et al. 2007). This method enables measurements with high accuracy and high time resolution. Therefore, the obtain results are more detailed than provided by conventional ultrasounds methods (Kopylow, Focke and Kalms 2007).

Integrating methods

Integrating methods involving two types of loading: thermal and mechanical.

With regard to the contactless character of thermal loading, it is suitable

for most of objects and materials. It is usually applied with assistance of shearography (suitable for rough and smooth surfaces), reflectometry (adequate for reflective surface), and holography (for small objects). Thermal excitation is commonly exploited in transient thermography, which monitors cooling behaviour of objects (Osten, Elandalousi, and Jüptner 1996). The measurements involve a thermography camera to monitor heating flow, which change dramatically during deformation of object surface. By subsequent time stepping, the alteration of the thermal flow can provide qualitative information about the depth of hidden defects. The mechanism of thermal loading in the structure with hidden defects is presented at Fig.2.16.

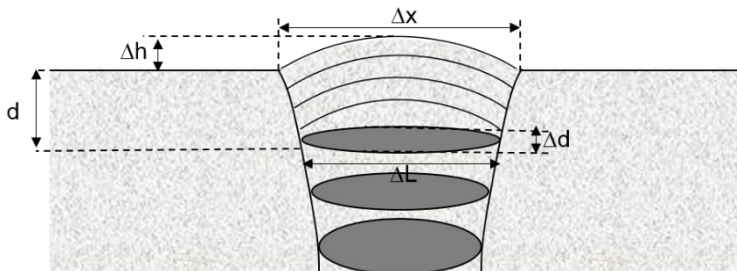


Figure 2.16. The mechanism of thermal loading. Heating causes the surface deformation, whose length (Δx) and high (Δd) is the same regardless the parameters (Δd , ΔL) of defects. (Huke et al. 2013).

Vibrational (mechanical) loading can be induced by pulsed excitation or by excitation with continuous waves. In practice, it requires an electro-mechanic or piezoelectric transducer.

Shearography is an optical technique compatible with vibrational and thermal excitation, as well. Its basis, as it was written above, are two images taken for the structure without loading, and after loading, this may result in surface deviation caused by hidden defects. The superposition refers to the change of surface gradient, which is altered by any defects below the surface.

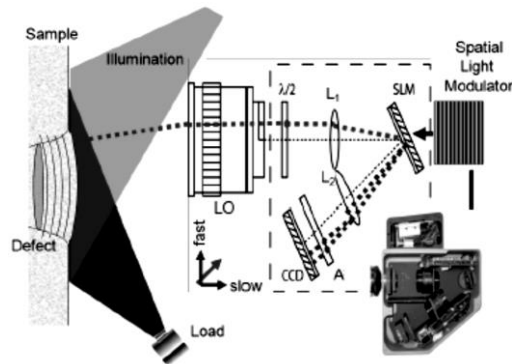


Figure 2.17. The system to detect hidden structural defects by shearography coupled with thermal loading, proposed by Falldorf et al. (Falldorf et al. 2009). The elements selected by the black dashed line are integrated into one single device (the right-bottom corner of scheme).

Figure 2.17 shows the setup to detect hidden, structural defects. In this system, the specimen (a damaged structure) is illuminated by the linearly polarized laser beam. The reflected wave passes the lens, which enables a larger area for inspection. Furthermore, the polarization of light is switched into circular. Circular-polarized light is focused by the lens (L1) on the spatial light modulator. The lens (L1) affects only a part of light, which is polarized in plane of it, while the other part with the perpendicular polarization is reflected. The CCD registered two beams shifted laterally. The registered image of the full field of view is sheared and the shear can be controlled by the spatial light modulator. (Huke et al. 2013).

According to the bcc research report (http://www.marketwired.com/printer_friendly?id=2079967), the total market of optical systems and non-destructive testing systems for inspection and maintenance, which was \$571 million of value in 2015, is supposed to reach \$875.7 in 2020.

2.3.2 Innovative materials with strain-sensitive optical parameters

The recent investigations on strain sensitive materials, were performed by Jimenez et.al (Jimenez, Kumar, Reis 2016), who has fabricated an

elastomeric slice by mixing the polydimethylsiloxane (PDMS), which is an optically clear media, with the suspension of black micrometre – sized dye particles. PDMS exhibits the average transmittance about 90 % for all light wavelengths except for two gaps in the infrared range. But this value decreases rapidly by adding a small amount of dopant. Indeed, having a concentration of particles equal to 0.17%, means a drastic decrease in the transmittance from 92%±0.5% (pure PDMS) to 7.2%±0.7%. The measurements were performed in visible light range by illuminating the sample with a light wavelength of 400÷700 nm. The value of the curing agent-to-base ratio of the PDMS influences the initial shear stiffness, and also the sample behaviour at high strain. On the contrary, the dopant does not influence the mechanical properties of the sample in the perpendicular direction to the propagation of light. When a stretch is applied, a thickness variation occurs and it equals to $h = h_0 \cdot \lambda_z$. The relationship between transmittance and stretch λ_z were determined based on Beer-Lambert law in the following form:

$$\bar{T} = \bar{T}_0^{\lambda_z} \quad (2.1.)$$

where \bar{T}_0 and \bar{T} are the initial transmittance and the transmittance of stretched sample, respectively. λ_z is the stretch perpendicular to the applied stress, following the direction of illuminating light. The transmittance is a function of the thickness of the sample, which decreases by with the deformation. The possible applications spans from smart windows for indoor light control, to band pass filters in microfluidic devices. By introducing dye particles with different colour it is possible to extend the light range for the calculated transmittance.

Chapter 3

State of the art in diffraction gratings

3.1. Definition and classification of diffraction gratings

To highlight the role and the importance of diffraction gratings for various fields of engineering and science, there is sufficient to mention two opinions coming from G.R Harrison, who is called a father of the modern diffraction grating (Chen and Schattenburg 2004), and J. Strong (Strong 1960):

“No single tool has contributed more to the progress of modern physics than the diffraction grating, especially in its reflecting form.” (Harrison 1949)

“It is difficult to point to another single device that has brought more important experimental information to every field of science than the diffraction grating. The physicist, the astronomer, the chemist, the biologist, the metallurgist, all use it as a routine tool of unsurpassed accuracy and precision, as a detector of atomic species to determine the characteristics of heavenly bodies and the presence of atmospheres in the planets, to study the structures of molecules and atoms, and to obtain a thousand and one items of information without which modern science would be greatly handicapped.” (Strong 1960)

A diffraction grating can be thought as a collection of reflecting / transmitting elements, such as transparent slits or apertures in an opaque screen, or reflecting grooves on a substrate, separated by a distance comparable to the wavelength of interacting light (Palmer and Loewen 2004). Considering the relation between its structural features and potential applications, a diffraction grating should be defined as an optical element with the spectral modulation of refractive index.

A diffraction grating is the most principle optical instrument, whose usefulness has been determined by the diffraction effect. Light interaction with a periodic structure of diffraction grating provides a diffracted wavefront, which propagates at a certain angle (termed as β_i in Fig.3.1) to the normal of grating surface. The wavefront is created by light beams in the same phase, which interfere with each other constructively.

The principles of light interaction with one-dimensional grating are depicted in Fig.3.1. Each scheme refers to the other type of grating. In Fig. 3.1.a, there is depicted a reflection grating, whose interaction with the incident light result in the diffracted light beam at the same side of grating as the incident beam. In case of transmission grating, the incident and the diffracted beams are at two the different sides of grating.

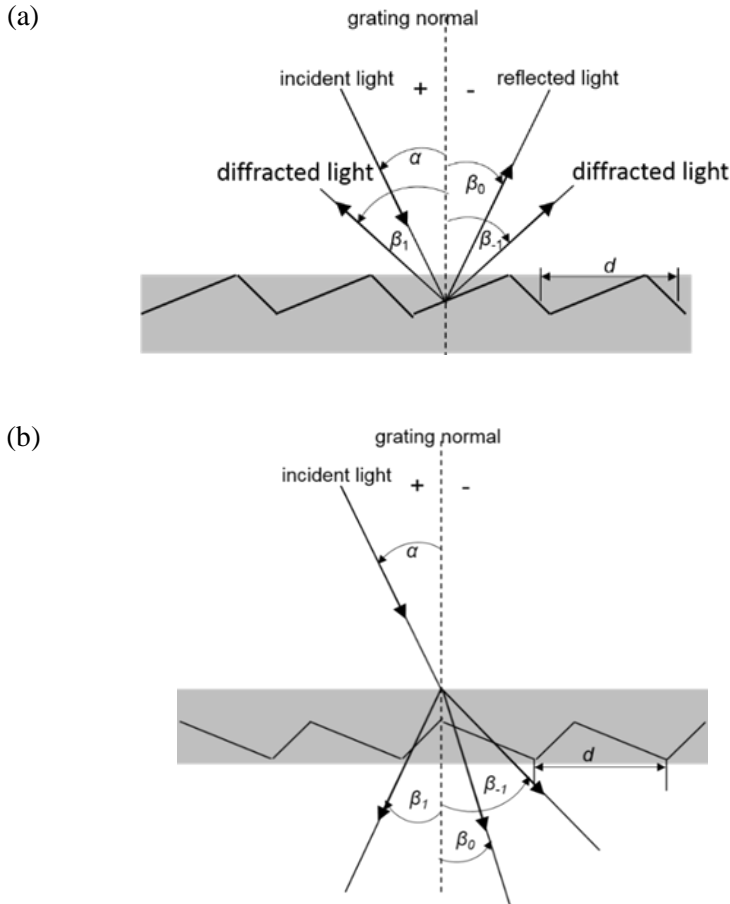


Figure 3.1. The interaction of monochromatic light with a) a reflection grating, b) a transmission grating. (Palmer and Loewen 2004)

Both schemes (Fig.3.1. a, b) involve the same notation i.e.: β_i is the diffracted angle, α is the incident angle, d refers to the groove spacing (also called the pitch). The signs '+' and '-' relate to the signs of angles. Angles measured from the grating normal clockwise are assigned as negative, whereas angles measured from the grating normal counter-clockwise are assigned as positive.

The term of constructive interference indicates the principle grating equation:

$$m \cdot \lambda = d \cdot (\sin\alpha + \sin\beta) \quad (3.1)$$

which determines the angular locations of intensity maxima, when light of wavelength λ is diffracted by the grating with the pitch d . Here, m is the *diffraction order* (also called spectral order). Sometimes, there is more suitable to use the modified form of eq. 3.1., i.e.:

$$Gm\lambda = \sin\alpha + \sin\beta \quad (3.2)$$

Where $G = 1/d$ is the groove frequency or groove density, which is also called “grooves per millimetre”.

However, this formula is applicable in the case, when the plane of incident and diffracted light beams are perpendicular to the plane of grating grooves (so called classical diffraction). Otherwise, eq. 3.2. must be modified to the following form:

$$Gm\lambda = \cos\zeta(\sin\alpha + \sin\beta) \quad (3.3)$$

where ζ is the angle between the incident light and the plane that is perpendicular to the grooves at the grating centre. In the simplest case, $\zeta = 0$, eq. 3.3 takes the form of eq.3.2. For $\zeta \neq 0$, eq.3.3. refers to the conical diffraction.

However, the diffraction effect is strongly influenced by parameters of diffraction gratings and the incident light wavelength. Hence, when a diffraction grating is illuminated by a polychromatic wavefront, different wavelengths are separated from each other with respect to the following relation:

$$\beta(\lambda) = \sin^{-1} \left(\frac{m\lambda}{d} - \sin\alpha \right) \quad (3.4)$$

For $m = 0$, a diffraction grating acts as a mirror. This effect is called specular reflection. On the other hand, if $\alpha = \beta$, the light is diffracted back toward the direction from which it came. This is called Littrow configuration defined by the following equation:

$$m\lambda = 2d\sin\alpha \quad (3.5)$$

The usefulness of diffraction grating relates to the diffraction effect, which is influenced by the grating quality, which can be assessed by the following parameters:

- diffraction order (m), a diffraction order corresponds to the interference of diffracted wavelengths in the same phase (the constructive interference). Interfering wavelengths are in the same phase, which is different for different wavelength and differ in the phase from other wavelengths. The phase difference determines the diffraction order, whose sign is defined by advances/retardance of phase, and relate to the path difference being an integral multiple of the wavelength. However, the number of diffraction order is strictly determined by the relation $|m\lambda / d| < 2$ and its sign depends on the relations between the incident angle and the diffracted angle as follow:

$$\beta > -\alpha, (m > 0) \quad (3.6a)$$

$$\beta < -\alpha, (m < 0) \quad (3.6b)$$

$$\beta = -\alpha, (m = 0) \quad (3.6c)$$

- dispersion is a measure of separation between diffracted light of different wavelengths (Loewen and Palmer 2004). In case of diffraction gratings, there are two its types: angular that expresses the spectral range per unit angle, and linear that expresses the spectral range per unit length. The angular dispersion, D , is calculated by differentiating the grating equation assuming that the incident angle is constant. Hence, the relative equation takes the form (Loewen and Palmer 2004):

$$D = \frac{d\beta}{d\lambda} = \frac{m}{d\cos\beta} = \frac{m}{d} \sec\beta = Gm \sec\beta \quad (3.7)$$

Thus, if the groove frequency, G , increases, the angular dispersion increases. It means that the angular separation increases between wavelengths of the same order m .

Substituting $\frac{m}{d}$ by $\frac{\sin(\alpha)+\sin(\beta)}{\lambda}$ (eq. 3.1), eq.3.7 takes the form:

$$D = \frac{d\beta}{d\lambda} = \frac{\sin(\alpha)+\sin(\beta)}{\lambda\cos(\beta)} \quad (3.8)$$

Eq.3.8. shows that for a given λ , the angular dispersion can be expressed as a function of incident angle, and a diffracted angle. In particular case, which is the Littrow configuration ($\alpha = \beta$), eq. 3.8. takes the form:

$$D = \frac{d\beta}{d\lambda} = \frac{2}{\lambda} \tan(\beta) \quad (3.9)$$

The *linear dispersion* for a given λ in order m (m corresponds to an angle of diffraction β) is the product of angular dispersion and the effective focal length, $r'(\beta)$, defined as follows:

$$r'D = r' \frac{d\beta}{d\lambda} = \frac{mr'}{d \cdot \cos(\beta)} = \frac{mr'}{d} \sec(\beta) = Gmr' \sec(\beta) \quad (3.10)$$

The quantity $r' \Delta\beta = \Delta l$ is the change in position along the spectrum (a real distance, rather than the wavelength).

More often than the linear dispersion, there is consider the *reciprocal linear dispersion (P)* defined as:

$$P = \frac{d \cdot \cos(\beta)}{mr'} \quad (3.11)$$

It is usually measured in (nm/mm), and is defined as a change of wavelength (measured in nm) in the spectrum, corresponding to a change in location along the spectrum (measured in mm)

- **resolving power** determines an ability of diffraction grating to separate adjacent spectral lines of average wavelength λ . Usually, it is expressed by a dimensionless quantity estimated by the equation:

$$R = \frac{\lambda}{\Delta\lambda} \quad (3.12)$$

The quantity $\Delta\lambda$ is the limit resolution, i.e. the wavelength difference between two lines with the same intensity that can be distinguished. The value of $\Delta\lambda$ can be assessed by applying *Rayleigh criterion*. The Rayleigh criterion allows finding two maximal intensities corresponding to two neighbouring wavelengths that can be identified as distinct spectral lines.

An alternative equation of eq. 3.12, eq. 3.13 can be applied. It depicts the dependence of the resolving power, the grating parameters (the grating pitch, d , the number of illuminated grooves, N , and an incident and a reflected angle.

$$R = \frac{N \cdot d \cdot (\sin\alpha + \sin\beta)}{\lambda} \quad (3.13)$$

In practice, the resolving power does not depend only on the angles α and β , but also on the optical quality of the grating surface, such as: the uniformity of the groove spacing, and the quality of associating optical instruments in the system (including detector elements).

- **spectral resolution** relates to the minimum wavelength difference ($\Delta\lambda$) between two wavelengths λ_1 and λ_2 which relate to each other $\lambda_2 = \lambda_1 + \Delta\lambda$. It can be determined by convoluting the image of the entrance aperture with the exit aperture. However, it depends not only on gratings, but also on the dimension and location of entrance and exit slits. Its units are nm.
- **bandpass** is difference of wavelengths relating to the half-maximum intensity; it is defined by the following formula:

$$B \sim w'P \quad (3.14)$$

From practical point of view, the instrument with a smaller bandpass can resolve wavelengths that are closer together than an instrument with a larger bandpass. There are two approaches to reduce the bandpass, by decreasing the light intensity, or by decreasing the width of the exit slit.

- **focal length and f – number** are used to characterize diffraction gratings (or their system) that have abilities to create an image as well as to diffract light, and disperse light that is not collimated. The focal length, $r'(\lambda)$, is defined as the distance between the centre of grating and the focus. Input, and output f – numbers (also called focal ratios) are defined by following formulas:

$$\frac{f}{no_{INPUT}} = \frac{r}{W}, \frac{f}{no_{OUTPUT}} = \frac{r'(\lambda)}{W} \quad (3.15)$$

- **free spectral range is determined by the range of wavelength** of given order whose superposition with the light of adjacent orders doesn't occur. The equation for its calculation is derived directly from:

$$\lambda + \Delta\lambda = \frac{m+1}{m}\lambda \quad (3.16)$$

as

$$F_\lambda = \Delta\lambda = \frac{\lambda}{m} \quad (3.17)$$

- **energy distribution (grating efficiency)** depends on many parameters including the power and the polarization of incident light, the incident and the diffraction angle, the refraction index of materials at the grating surface and the groove spacing. Two

basic formulas defining the maximum efficiency of gratings refers to the *blaze conditions* and *Littrow blaze conditions*. The blazed conditions are defined as follow:

$$m\lambda = 2d\sin\theta_B \quad (3.18)$$

where θ_B is the *blaze angle* defined as the angle between the face of groove and the plane of the grating (Fig.3.2).

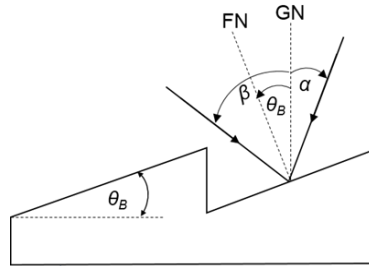


Figure 3.2. The configuration corresponding to the blazing effect. θ_B is confined between the grating normal (GN) and the face normal (FN) of groove. Based on (Loewen and Palmer 2004)

The satisfied blaze conditions are determined by $\alpha - \theta_B = \beta - \theta_B$

The blaze angle determines the related reflected wavelength, which can be computed by the following equation:

$$\lambda_B = \frac{2d}{m} \sin(\theta_B) \quad (3.19)$$

- **signal-to-noise ratio** is the ratio of diffracted energy to unwanted energy (Loewen and Palmer 2004). This parameter is typical for all optical instruments, not only for gratings. However, there are not any rules clarifying which grating provides higher SNR.
- **image magnification**
- **scattered and stray light**

There are so many criteria to categorize diffraction gratings as many various type of their structural geometry, fabrication techniques, the surface shape/geometry, and applications are available for them. However, this list is not complete and has been extending following a

progress in fabrication technologies and appearing new applications. Nevertheless, companies (e.g. Newport Group) producing diffraction gratings have introduced the selection with respect to a fabrication technique, which, in fact, indicates other criteria such as: the shape of surface, and applications. The criteria proposed by Richardson Gratings refer to:

- techniques of fabrication a master grating: *holographic gratings*, *ruled gratings*; there are also replicated gratings that are derivatives of master gratings, manufactured by replication of master gratings;
- shape of grating surface: plane gratings, concave gratings;
- applications: UV/VIS gratings, fibre optic telecommunications gratings, dye laser tuning gratings, large astronomical gratings, pulse compression gratings

From theoretical point of view, especially considering light effects, the distribution of periodicity seems to be more important. Hence, the selection proposed by Bruno and Reitich (Bruno and Reitich 1993) distinguishes two types of diffraction gratings, i.e. singly periodic (classical) diffraction gratings, doubly periodic (biperiodic or crossed) diffraction gratings.

Ruled gratings

Ruled method refers to most spectroscopic gratings. Diffraction gratings are formed by ruling engines, which are precise setups that determine the quality of grating product. Hence, there are three fundamental types of ruling engines: the Michelson engine, the Mann engine, the MIT 'B' engine. The ruling process is performed on the substrate, which is carefully selected and prepared by polishing and coating by thin reflective film of aluminium or gold.

Another important factor determining the quality of produced grating are fabrication conditions. Hence, they highly important to keep relevant pressure and temperature of fabrication area. The ruling process desires a constant value of pressure, and temperature. Hence, their variations should be compensated. Fluctuations of pressure are undesired because they induced changes in the refractive index of air affecting monochromatic light, which is used in interferometric control. Not compensated fluctuations of atmospheric pressure result in variations of groove spacing. Furthermore, the ruling engine should be isolated from

any vibrations of the range of (2÷60) Hz, which are well-transmitted by the diamond element that is responsible for the surface shape. Frequencies out of this range cause negligible effects.

Fabrication of ruled master gratings is a long, slow and painstaking process (Loewen and Palmer 2004). It is often supported by a high-power interference microscope, or an electron microscope for more finely spaced grooves. Upon microscopic examination, the diamond tool is readjusted to match the groove shape to the particular grating being ruled. One of the representative ruled product is a blazed diffraction grating. Its high precision of performance refers to the high-energy efficiency and its ability to concentrate the light selectively at a certain part of the spectrum.

Holographic gratings

In general, manufacture principles of holographic gratings refer to two steps: formation of pattern and formation of grooves. A standing wave pattern is created in a photographic plate by interference of two coherent and monochromatic plane waves with the equal polarization and intensity. The pattern consists of bright and dark fringes set alternatively. The contrast between them and the minimal intensity of pattern depend on the intensities of interfering beam. The non-equal intensities result in lower contrast and the non-zero value of minimal intensity of pattern.

The distance, d , between the centres of adjacent fringes (adjacent lines of maximum intensity) can be calculated with respect to the formula:

$$d = \frac{\lambda}{2\sin\theta} \quad (3.20)$$

Here, λ refers to the wavelength of illuminating light beams, and θ is the half of angle between them.

The grooves are formed by the interaction between a laser light and photoresist. Photoresist is a material whose intermolecular bonds are strengthened or weakened by exposure to light. Currently available photoresists are more sensitive to some wavelengths than to the others. Hence, the type of photoresist should be matched to the recording wavelength.

There are two types of photoresist: positive and negative. In positive photoresist, the part of material exposed to light is dissolved, whereas in negative photoresist the unexposed part of material is dissolved. Upon

immersion in the chemical developer, a surface relief is formed as follows: valleys are formed at the places of bright fringes, and ridges are formed at the places of dark fringes.

There are two methods to record a fringe pattern: the single-beam interference and the double beam interference. Each of them provides a related type of diffraction gratings i.e. a single-beam holographic grating (also called Sheridan grating) and classical equivalent holographic grating (classical equivalents), respectively (Loewen and Palmer 2004). Fabrication of holographic gratings with spectroscopic quality requires following conditions:

- optical bench and laser should be stable, and optical instruments should be high-quality;
- ambient light should be eliminated completely to keep the high contrast of fringes;
- due to influence the refraction index by thermal gradients and air currents, they should be avoided;
- during recording, all optical components of experimental setup must be of nearly diffraction-limited theory. Hence, they should be adjusted as carefully as possible. Any objects receiving laser illumination may scatter the light and be potential source of straight light distorting the record.

Replicated gratings

The fabrication process of replicated gratings (the replication process) refers to the following steps

- submaster selection refers to the choice of suitable sub master grating with respect to its properties (e.g. the groove frequency, the blaze angle, the size, etc.). A submaster grating is a grating used not as a final product, but is used for replication of final product grating. Thus, it does not have to possess the same performance details as product grating, e.g. a suitable reflecting coating.
- application of parting agent aids separation of sub master surface and a product grating surface. Thus, it should be negligible thin and should serve no deleterious optical effects.
- application of transfer coating usually involves aluminium for covering the surface of sub master. It serves as a coating on the product grating. To obtain high-quality optical coating, this step

is performed in a vacuum deposition chamber. Since, the coating is applied directly onto the sub master surface and then, transferred onto the product grating by via separation, it is called transfer coating;

- cementing refers to deposition of product resin layer onto the top of transfer coating. This layer holds the grooves profile and replicates it from the sub master to the product. Since the transfer coating is too thin for such purposes, the product resin is suitable for this application even considering its thickness, which is amounts about tens of microns. Primary, the resin is in the liquid state. However, to enable the adequate shape of grooves and a high-quality surface of product grating, it must be cured by heating or lasting at the room temperature for hardening. An alternative technique to produce a replicated grating involves a UV-curable resin
- separation is performed after the resin is fully cured. The profile of product grating is the inverse of the grooves on the sub master surface. Otherwise, the efficiency characteristics of product grating and sub master are different. In that case, there is desired to perform replication once again, whose product grating will possess profile identical to the sub master. In case of product grating with transmission properties, the transfer coating is removed, leaving the intact grooves in the transparent resin
- inspection is the final step of replication process. It is performed to detect any damages in the sub master surface or in the product grating surface. However, it can provide a characteristic of product grating surface, which refers to the efficiency, wavefront flatness (or curvature), a scattered light, alignment of grooves to a substrate edge.

Replication process can be hired as an alternative technique to produce diffraction gratings with spectroscopic quality. It is low-cost and providing thousands of replicas of master gratings. Hence, product gratings are commercially available. However, there are some hazards relating to this technique, such as: scratching, which disturbs significantly the regular profile of grooves in a grating replica, or surface contamination from fingerprints, which can be fixed by cleaning or recoating the damage surface to recover the original conditions.

3.2. Mathematical description of diffraction influenced by deformation of diffraction grating

The initial approaches to detect strain in a deformable structure were proposed independently by J.F. Bell (Bell 1956) and A. Asundi (Asundi and Zhao 2000). Both approaches refer to the two-dimensional theory of diffraction, which involves angular variations of 1st order diffracted beam to assess surface variations of control structure. Hence, information about the direction of normal surface is desired, what limits an application of both approaches only to the laboratorial conditions. Alternative approach, the conical theory of diffraction, requires information about the orientation and the pitch of diffraction grating. Both theories are suitable for investigations at laboratorial conditions, whereas an application of strain gauge requires to solve following reverse problem (Alcock et al. 2004): for arbitrary incidence of the probe beam, can the pitch be uniquely determined by measuring the position of the diffracted orders from a grating that has arbitrary orientation in three-dimensional space?

The approaches proposed by Bell and Asundi involved a one-dimensional grating interacting with a monochromatic, coherent laser light. The pitch variations tuned the diffracted angle of the 1st order beam as describes the principle equation of diffraction grating (Hecht 2002):

$$d \cdot (\sin\beta_m - \sin\alpha) = m \cdot \lambda \quad (3.21)$$

In general, eq.3.21 and eq.3.1 are equal. The only one difference is that Loewen and Palmer respect the sign of incident and diffracted angles as ($\beta_m > 0$ and $\alpha < 0$), whereas Hecht considers only their absolute values. The engineering strain of the surface, perpendicular to the ruling of diffraction grating is defined by:

$$\varepsilon = \frac{(d-d_0)}{d_0} \quad (3.22)$$

Here, d refers to the pitch of stretched grating, whereas d_0 is the pitch of nonstretched diffraction grating. This equation can be expressed by the diffracted angles of first order ($m = 1$ and $m = -1$) as follows:

$$\varepsilon = \frac{\sin\beta_{+1}^0 - \sin\beta_{-1}^0}{\sin\beta_{+1} + \sin\beta_{-1}} - 1 \quad (3.23)$$

The superscript ‘0’ refers to the nonstretched diffraction grating. Hence, the ε is independent from the incident angle α .

Assuming, the initial pitch of diffraction grating is given, the error of strain can be defined by the relation to the errors of angular position of the diffracted orders, $\Delta\beta_{+1}$ and $\Delta\beta_{-1}$, as follow:

$$\Delta\varepsilon = \frac{(\sin\beta_{+1}^0 - \sin\beta_{-1}^0)(\Delta\beta_{+1}\cos\beta_{+1} - \Delta\beta_{-1}\cos\beta_{-1})}{(\sin\beta_{+1} - \sin\beta_{-1})^2} \quad (3.24)$$

Such calculations performed at laboratorial conditions (Wileman et al. 1994) provide results with the precision of 10^{-6} . However, their application is limited only to the case of defined surface normal and the near-normal light incidence.

Although, this method exhibits advantages over conventional strain gauges (i.e. remote measurements without electrical connections in hostile environments, no creep problems and measurements performed over the lifetime of object), its serious drawback for practical applications is non-defined normal incidence of the probe beam, which prevent the use of hand-held instrumentation. According to consideration in (Alcock et al. 2004), this case corresponds to the measurements of diffracted angle with a ‘correlated’ error $\Delta\beta_{+1} = \Delta\beta_{-1} = \Delta\beta$. This problem can be avoidable, if the incident beam overlaps the surface normal. Then, $\cos(\beta_{+1})$ and $\cos(\beta_{-1})$ are equal. Nevertheless, the angular error of 0.03 rad (2°) results in the strain error of the order of 10^{-3} .

To solve this problem Alcock et al. proposed mathematical formalism that can solve the reverse problem and be a suitable alternative even for application in a hostile environment They considered a plane incident beam, defined by the wave vector \mathbf{k}_i , that illuminates the reflection grating at the top (Fig.3.3.)

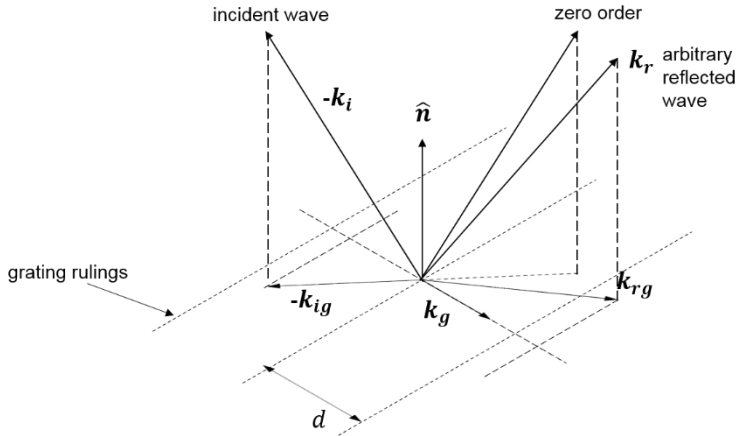


Figure 3.3. Wavevector geometry at the diffraction grating (Alcock et al. 2004). The notation refers to the notation used in the equations describing the phenomenon.

The electric field of incident beam in plane of the grating at a position \mathbf{a}_g are defined by its scalar complex amplitude $\underline{U}_i(\mathbf{a}_g)$ as follows:

$$\underline{U}_i(\mathbf{a}_g) = \underline{U}_{i0} \exp(j(\mathbf{k}_{ig} \cdot \mathbf{a}_g)) \quad (3.25)$$

Here, \mathbf{k}_{ig} is the projection of \mathbf{k}_i onto the plane of diffraction grating and \underline{U}_{i0} is a constant value.

A diffraction grating is characterized by the two-dimensional complex reflection coefficient operating in the plane of grating. If the reflection coefficient is represented by a function $\underline{r}(\mathbf{a}_g)$, the reflected amplitude in the diffraction grating plane is defined as:

$$\underline{U}_{rg}(\mathbf{a}_g) = \underline{r}(\mathbf{a}_g) \underline{U}_{ig}(\mathbf{a}_g) \quad (3.26)$$

Approaching the diffraction grating as an infinite periodic structure, the reflection coefficient can be written as Fourier series as follow:

$$\underline{r}(\mathbf{a}_g) = \sum_{m=-\infty}^{m=+\infty} r_m \exp[j \cdot m \cdot (\mathbf{k}_g \cdot \mathbf{a}_g)] \quad (3.27)$$

r_m is Fourier coefficient and \mathbf{k}_g refers to the grating vector, which lies in the plane of grating and is perpendicular to its ruling. Its relation to the pitch (d) of grating is defined by:

$$d = \frac{2\pi}{|\mathbf{k}_g|} \quad (3.28)$$

The reflected field in the plane of the grating can be estimated as:

$$\underline{U}_{rg}(\mathbf{a}_g) = \underline{U}_{i0} \sum_{m=-\infty}^{m=+\infty} \underline{r}_m \exp[j(m\mathbf{k}_g + \mathbf{k}_{ig}) \cdot \mathbf{a}_g] \quad (3.29)$$

In order to find the vector directions of the diffracted orders, there is needed to decompose the field in the plane of grating regarding following equation:

$$\underline{U}_{rg}(\mathbf{a}_g) = \iint_{S_g} \underline{A}(\mathbf{k}_{rg}) \exp[j(\mathbf{k}_{rg} \cdot \mathbf{a}_g)] d\mathbf{k}_{rg} \quad (3.30)$$

Where \mathbf{k}_{rg} is the projection of an arbitrary reflected wave vector onto the plane of the grating, and $\underline{A}(\mathbf{k}_{rg})$ is the plane wave spectrum of $\underline{U}_{rg}(\mathbf{a}_g)$, which is defined by following relationship:

$$\underline{A}(\mathbf{k}_{rg}) = \iint_{S_g} \underline{U}_{rg}(\mathbf{a}_g) \exp[-j(\mathbf{k}_{rg} \cdot \mathbf{a}_g)] d\mathbf{a}_g \quad (3.31)$$

In order to calculate the integral over the whole surface of the diffraction grating (S_g), the eq. 3.29 should be modified into the form:

$$\underline{A}(\mathbf{k}_{rg}) = \underline{U}_{i0} \sum_{m=-\infty}^{m=+\infty} \underline{r}_m \iint_{S_g} \exp[j(m\mathbf{k}_g + \mathbf{k}_{ig} + \mathbf{k}_{rg}) \cdot \mathbf{a}_g] d\mathbf{a}_g \quad (3.32)$$

Considering the orthogonality of complex exponentials, eq. 3.31 can be expressed as:

$$\underline{A}(\mathbf{k}_{rg}) = 2\pi \underline{U}_{i0} \sum_{m=-\infty}^{m=+\infty} \underline{r}_m \delta(m\mathbf{k}_g + \mathbf{k}_{ig} + \mathbf{k}_{rg}) \quad (3.33)$$

Equation 3.29 refers to the decomposition of reflected field into plane-wave components propagating in the plane of diffraction grating. In case of isotropic and linear media, a difference between the components exists only in the phase, whereas the power is invariant and can be calculated as:

$$P_A(\mathbf{k}_{rg}) = \underline{A}(\mathbf{k}_{rg}) \cdot \underline{A}^*(\mathbf{k}_{rg}) = P_0 \sum_{m=-\infty}^{m=+\infty} \underline{r}_m \delta(m\mathbf{k}_g + \mathbf{k}_{ig} - \mathbf{k}_{rg}) \quad (3.34)$$

Hence, there is clear that the power is non-zero for the fulfilled term:

$$\mathbf{k}_{rg} = m\mathbf{k}_g + \mathbf{k}_{ig} \quad (3.35)$$

In the above equation, the components of incident (\mathbf{k}_{ig}) and reflected (\mathbf{k}_{rg}) wave vectors in the plane of grating correlate with the fundamental grating vector (\mathbf{k}_g) and its harmonics. Using the grating normal (\hat{n}) to define both components as follow:

$$\mathbf{k}_{rg} = \mathbf{k}_r - (\mathbf{k}_r \cdot \hat{\mathbf{n}}) \cdot \hat{\mathbf{n}} \quad (3.36a)$$

$$\mathbf{k}_{ig} = \mathbf{k}_i - (\mathbf{k}_i \cdot \hat{\mathbf{n}}) \cdot \hat{\mathbf{n}} \quad (3.36b)$$

By applying eq. 3.36a and eq.3.36b to substitute \mathbf{k}_{rg} and \mathbf{k}_{ig} in eq. 3.35, the following formula was obtained:

$$\mathbf{k}_r - (\mathbf{k}_r \cdot \hat{\mathbf{n}}) \cdot \hat{\mathbf{n}} = m\mathbf{k}_g + \mathbf{k}_i - (\mathbf{k}_i \cdot \hat{\mathbf{n}}) \cdot \hat{\mathbf{n}} \quad (3.37)$$

Equation 3.37 includes only two unknowns: $\hat{\mathbf{n}}$ and \mathbf{k}_g . They can be easily estimated by measuring two reflected beams \mathbf{k}_{rA} and \mathbf{k}_{rB} , which correspond to the first order of reflected light, $m = 1$ and $m = -1$, respectively. Writing eq.3.37 for \mathbf{k}_{rA} and \mathbf{k}_{rB} result in the set of equations:

$$\begin{cases} \mathbf{k}_{rA} - (\mathbf{k}_{rA} \cdot \hat{\mathbf{n}}) \cdot \hat{\mathbf{n}} = \mathbf{k}_g + \mathbf{k}_{iA} - (\mathbf{k}_{iA} \cdot \hat{\mathbf{n}}) \cdot \hat{\mathbf{n}} \\ \mathbf{k}_{rB} - (\mathbf{k}_{rB} \cdot \hat{\mathbf{n}}) \cdot \hat{\mathbf{n}} = -\mathbf{k}_g + \mathbf{k}_{iB} - (\mathbf{k}_{iB} \cdot \hat{\mathbf{n}}) \cdot \hat{\mathbf{n}} \end{cases} \quad (3.38)$$

whose solution corresponds to the solution of reverse problem, i.e.:

$$\hat{\mathbf{n}} = \frac{(\mathbf{k}_{iA} + \mathbf{k}_{iB}) - (\mathbf{k}_{rA} + \mathbf{k}_{rB})}{|(\mathbf{k}_{iA} + \mathbf{k}_{iB}) - (\mathbf{k}_{rA} + \mathbf{k}_{rB})|} \quad (3.39)$$

$$\mathbf{k}_g = (\mathbf{k}_{iB} - \mathbf{k}_{rB}) - [(\mathbf{k}_{iB} - \mathbf{k}_{rB})\hat{\mathbf{n}}]\hat{\mathbf{n}} \quad (3.40)$$

Furthermore, both values allow assessing the strain value based on following formula:

$$\varepsilon = \frac{\Delta d}{d_0} = -\frac{|k_{g0}|}{\Delta|k_g|} \quad (3.41)$$

This approach was verified experimentally. The experiment is briefly described in the next subchapter.

3.3. State of the art in diffraction gratings as applied to SHM

A diffraction grating is one of those optical instruments, whose structural geometry affects its optical response. In fact, any structural changes affected by external stimulations (e.g. interaction with other waves, loading applied by compression or stretching) can be detected by control parameters of diffracted light. However, measurements with optical techniques require several steps including design and mounting an experimental setup with relevant instruments and devices, deep analysis of observations based on mathematical relationships.

3.4b, it is depicted by t and confined between normal to the current surface and diffracted beam (GE'). The total angular motion of diffracted beam was determined as $\Delta y = t + y - t_0 - \Delta t$.

The proposed setup included following elements (depicted in Fig.3.4a by numbers 1 – 9): 1 – the specimen; 2 – the mass inducing strain in the specimen; 3 – the light source; 4, 5 - lenses focusing the diffracted and the reflected light. 6 and 7 – the V-slits; 8 and 9 - photo-multipliers

Here, the light was generated by the source and illuminated the grating attached to the surface. The interaction between the grating and the light provides two beams: reflected and diffracted. Each of them passed the lens through and interacts with the one of V slits, which constituted the light of certain intensity. The intensity was measured by the photo-multiplier, which was connected to the oscilloscope.

The main objectives of Bell's invention were:

- to avoid drawbacks of conventional wire strain gauge;
- to measure the strain, the slope of surface and the linear displacement, with a high degree of accuracy;
- To create setup with instruments enabling strain measurements based on angular variations of diffracted beam.

Further experiments involved more sophisticated measurement instruments, and were supported by detailed calculations and an error analysis.

For instance, A. Asundi and B. Zhao (Asundi and Zhao 2000) performed an experiment, which involved a linear diffraction grating to assess strain sensitivity of deformable sample based on monitoring two symmetrical diffracted light beam of the first order ($m = 1$ and $m = -1$, m is the order value). In their approach, the grating was fixed to the surface of deformable sample. The grating (its resolution amounted 1200 lines/mm) was illuminated by the monochromatic, coherent light coming from He-Ne laser ($\lambda = 632.8$ nm). The light was propagating vertically to the surface of diffraction gratings. Each reflected beam was registered by two separated, position-sensitive detectors (PSD). Their main advantages over CCDs are:

- small sizes;
- high (relative) resolution of 1/5000;
- insensitivity to light intensity variations, which enables an accurate position measurement even the light intensity varies;

- compatibility with the wide range of wavelength (from 300 nm to 1100 nm);
- dynamic strain measurements (the first measurements occurred after 20 μ s).

To eliminate noises, two bandpass filters were applied before the PSD sensors.

Figure 3.5 shows two schemes. The first one explains the methodology and the second one depicts the experimental setup.

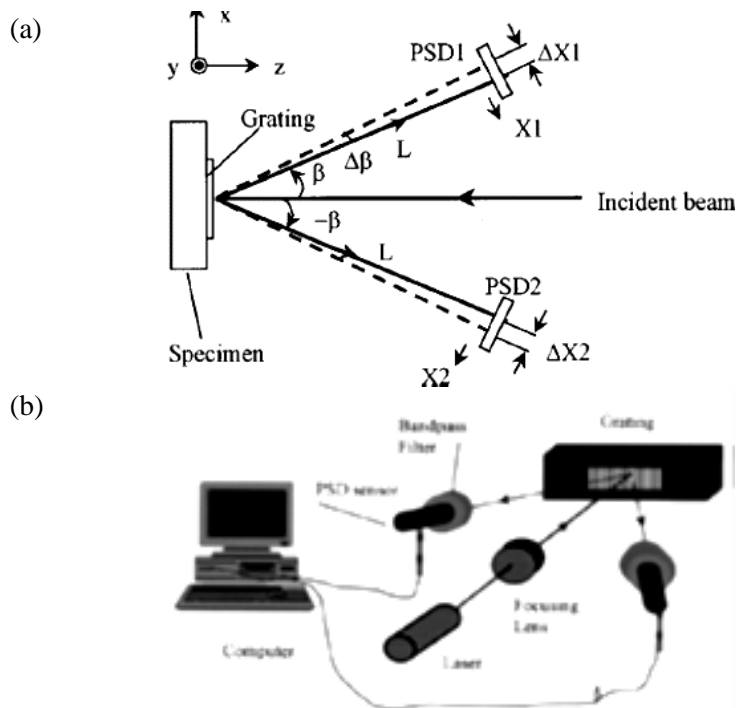


Figure.3.5. a) The methodology of measurements; b) the experimental configuration of setup elements. (Asundi and Zhao 2000)

The collected data were used to calculate ϵ_x (the normal strain in x direction), $\Delta\epsilon_x$ (the strain error), and errors of diffraction angles, $\Delta\beta_1$ and $\Delta\beta_2$.

The method proposed by Zhou and Asundi, provide following results

- sensitivity of 1 $\mu\epsilon$
- variable spatial resolution from 0.1 to 2mm;
- measuring position flexibility i.e. any point in the grating area

can be measured;

- range of strain up to 15%;
- dynamic strain measurement capability and continuous measurement;
- automatic data acquisition and processing;
- user friendly visual instrument interface;
- compact size.

This approach exhibits several advantages over conventional optical techniques (moiré interferometry technique, speckle techniques and holography techniques), i.e.:

- no fringe pattern interpretation is required;
- there is no need to use the master grid;
- the system is simple and easily integrated;
- it doesn't require any special high-resolution recording system

Another approach to develop a strain sensor based on diffraction grating was proposed by Chandra et al. (Chandra, Yang and Lin 2007), who fabricated an easily stretchable sample by using (polydimethylsiloxane) (PDMS). The fabrication referred to the following actions (depicted schematically in Fig. 3.5 (a-e).):

- the thin PDMS layer was stretched bidirectional in plane;
- the top of elastomeric layer was covered by a hard oxide;
- the bilayer film was released resulting in buckling effect, which forms wrinkled patterns spontaneously; for oxidation and buckling effect limited to an area smaller than the wavelength of unconfined wrinkles, the final effect corresponds to the microlens structure.

The experimental sample was prepared in two variants. The first one was a concave structure composed of PDMS matrix with semispherical elements arranged hexagonally into a two-dimensional array. The second sample was manufactured by the replication of the first one i.e. by moulding PDMS layer onto the concave substrate. The final product possessed repeatable convex elements (i.e. semispheres instead of voids) arranged similar to the master sample.

The data provided by the stretching test supported calculations of such parameters as: diameter (D), thickness (h), radius of curvature (R), curved surface area (A), and focal length (f).

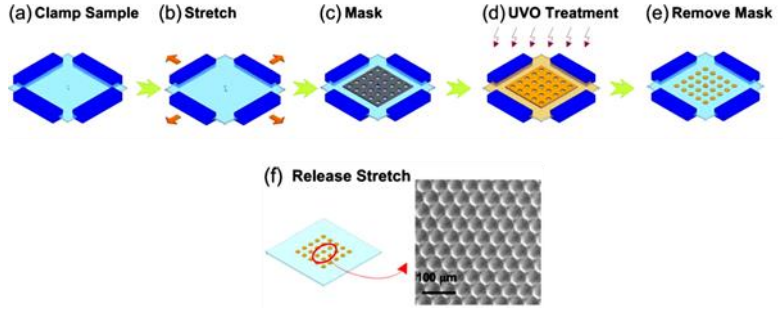


Figure 3.6. The fabrication of concave microlens array. The letters (a) – (f) refer to the subsequent steps of fabrication. (Chandra, Yang and Lin 2007).

In case of concave microlens array, the applied stress caused increase of the base surface, and of the curved surface. In fact, the focal length increased with respect to the following formula:

$$f = \frac{A}{2\pi(n-1)\sqrt{\frac{A}{\pi} \frac{D^2(1+\varepsilon)^2}{4}}} \quad (3.42)$$

where n is the refractive index of lens material.

The stretching limit corresponded to the term ε_p , ε_p is prestrain applied to the PDMS layer during fabrication to cause buckling effect. In fact, when the limit was achieved, the curved surface disappeared completely, and got equal to the base area. This effect appears, when the relation between strain and the curved surface, A , satisfied eq.3.43.

$$A = \frac{\pi D^2}{4} \left(1 + \frac{\varepsilon_p - \varepsilon_0}{\varepsilon_p} \varepsilon + \varepsilon_0 \right)^2 \quad (3.43)$$

where the value of ε_0 is estimated from initial lens profile by comparison of the base area and the curved surface area as shown in Fig. 3.7.

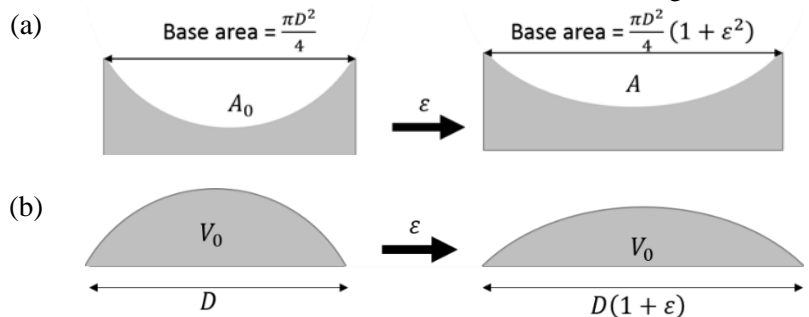


Figure 3.7. Deformation of a) the concave surface, b) the convex surface, during stretching. Based on (Chandra, Yang and Lin 2007).

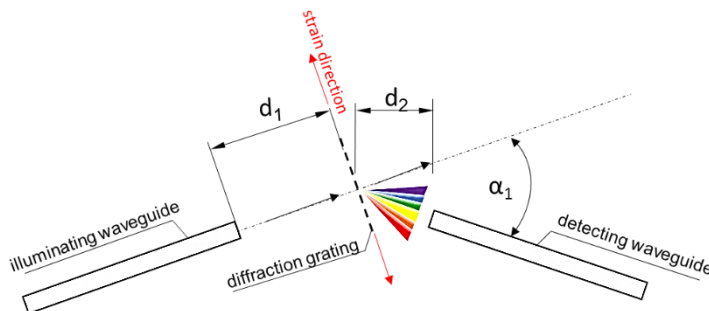
In case of stretching the convex array, the diameter of lens, D , increased and its thickness h decreased (the total volume V_0 is conserved). The focal length can be estimated as a function of strain based on the following equation:

$$f^3 - \left[\frac{\pi D^4 (1+\varepsilon)^4}{64(n-1)V_0} \right] f^2 - \left[\frac{\pi D^6 (1+\varepsilon)^6}{768(n-1)^3 V_0} + \frac{3V_0}{4\pi(n-1)^3} \right] = 0 \quad (3.44)$$

The differences in fabrication procedure result in different response to stretching of both specimens. Larger range of focal length tunability was obtained from concave lens array than that from convex lens array. The experiment provides valuable results for sensing application in optical microdevices and MEMS.

Kelb et al. (Kelb, Reithmeier and Roth 2014) demonstrated a full-optical setup as a potential component of MOEMS. The experimental principles referred to the spectral properties of diffraction grating. A diffraction grating illuminated by monochromatic light separates different wavelengths. The diffracted wavelength depends on parameters of diffraction gratings, which are tuneable by structural deformation. The authors present two fundamental concepts. The first one involved two waveguides set in front of each other. The first waveguide focused the guided light into single spot at the entrance of the second one, which was a detecting waveguide. For stress applied along the waveguide configuration, the distance between the waveguides increased. In fact, the intensity of coupled light decreased. The measurement of light intensity as a function of varying distance enabled determination of strain, direction of elongation and its magnitude.

(a)



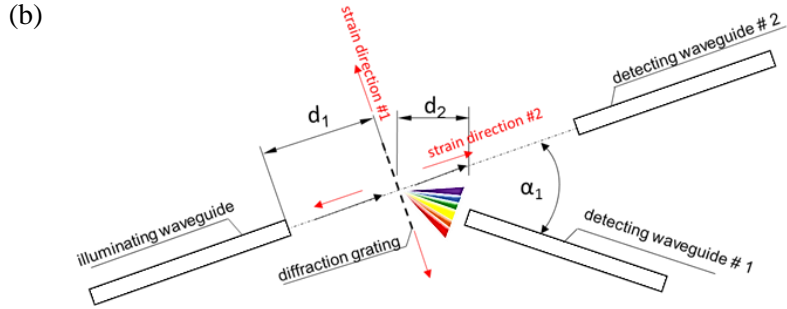


Figure 3.8. a) The strain detecting setup involving the chromatic approach; b) the experimental setup to assess two-dimensional strain. (Kelb, Reithmeier and Roth 2014).

In the second approach, the experimental setup was composed of three elements: the illuminating waveguide, the diffraction grating and the detecting waveguide. The components were arranged on the PMMA substrate ($n_{PMMA} = 1.49$) (Fig.3.8a). The rib waveguide structure was made of cyclic olefin copolymer (COC, $n_{COC} = 1.53$). The pitch (spatial period) of diffraction grating amounted $2\mu\text{m}$ and the numerical aperture of both waveguides was equal to $NA = 0.348$. The illuminated wavelength used in the experiment ranged from 380nm to 780nm. The detecting waveguide was set about 1mm from the grating and at the angle $\alpha_1 = 11.25^\circ$, and centred within the maximum of the 1st order diffraction spectrum. The width of grating slit was calculated as $s = 0.5 \cdot p$ to prevent a record of 2nd order diffraction beam.

The third proposed setup was a combination of two previous setups. It hired another one waveguide to register the intensity of the non-diffracted 0 order beam. It was placed along the optical axis of illuminating beam. The setup was designed to detect the two-dimensional strain. Hence two directions of strain appearance were considered, as depicted in Fig. 3.8b. For the first case (“strain direction #1”), the changes in diffracted light spectrum were registered by the detecting waveguide #1, whereas the second waveguide was independent, and registered the optical response also in the second case (strain direction #2)

The proposed setups exhibit following advantages:

- they are easily scalable thanks to;

- they are suitable to apply in micro-opto-electro-mechanical systems (MOEMS) because of its small size, polymeric components (PMMA and PDMS) resulting in light weight, and fabrication technique i.e. hot embossing, which is compatible with MOEMS fabrication.
- The chromatic sensor allows detecting 1% of strain resulting in 0.5nm of wavelength shift.

The theoretical approach described in section 3.2, proposed by Alcock et al. was verified experimentally (Alcock et al. 2004). The experimental aim was to measure the creep (the relaxation of sealing force) in a high-pressure gasket assembly. It consisted of four bolts (M10), 5mm-thick Perspex gasket placed between two, square mild steel plates. Creep was detected by measuring the tension in bolts. Hence, the top of each bolt was polished and the reflective diffraction grating was imprinted on it by using an excimer laser. The experimental setup mounted to perform measurements included following components: the helium-neon laser, which generated two collimated probe beams (\mathbf{k}_{iA} , \mathbf{k}_{iB}) that intersected at the angle of 60° illuminating the bolt head. In fact, the surface of diffraction grating was in the intersection area. The measurements referred to two reflected beams (\mathbf{k}_{rA} and \mathbf{k}_{rB}) of the first order ($m = 1$ and $m = -1$), which pass the imaging lens reducing the aberration effects. Both beams were controlled by the charge-coupled device (CCD) camera. To determine the grating normal, the directions of reflected beams should be calculated based on direction cosines (α, β, γ) defined as:

$$\alpha = \frac{x}{\sqrt{x^2 + y^2 + f^2}}, \quad (3.45a)$$

$$\beta = \frac{y}{\sqrt{x^2 + y^2 + f^2}}, \quad (3.45b)$$

$$\gamma = \sqrt{1 - \alpha^2 - \beta^2} \quad (3.45c)$$

Here, f is a distance between the imaging lens and the CCD camera and x, y are coordinates of the beam position on the CCD array.

The calculations of strain (ε) and force providing by each bolt (F) hired the following equations:

$$\varepsilon = bT, \quad (3.46a)$$

$$F \cong \frac{5T}{D}, \quad (3.46b)$$

where T terms the torque, D refers to the diameter of bolts, and b is a constant equal to $30\mu\epsilon/(\text{N}\cdot\text{m})$ for each bolt.

In the first approach, the strain values were computed for the constant room temperature, affected just by the various values of torque. In the second approach, the specimen was heated inside the oven in the temperature range of $(20\div 130)$ °C and the strain was calculated as a function of applied temperature. In both approaches, the data were collected for each bolt.

Chapter 4

Photonic crystals (PhCs)

4.1 Definition and classification of photonic crystals

Photonic crystals (PhC) are optically active media with periodic, internal structure. They consist of at least two components differing from each other with refractive index. The simplest case of photonic crystals includes a sequence of layer with different refractive index, laying on each other alternatively and creating so called multilayer stack. More complicated structures, such as two- and three-dimensional photonic crystals, exhibit the periodicity distributed in two and three dimensions, respectively (Fig.4.1.)

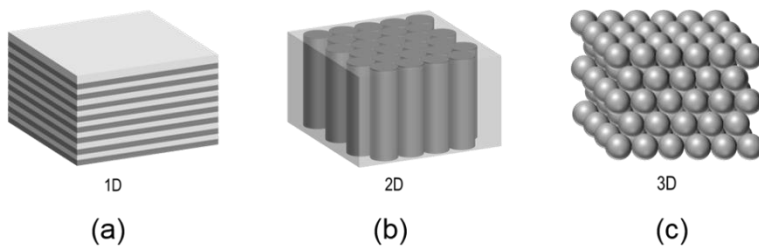
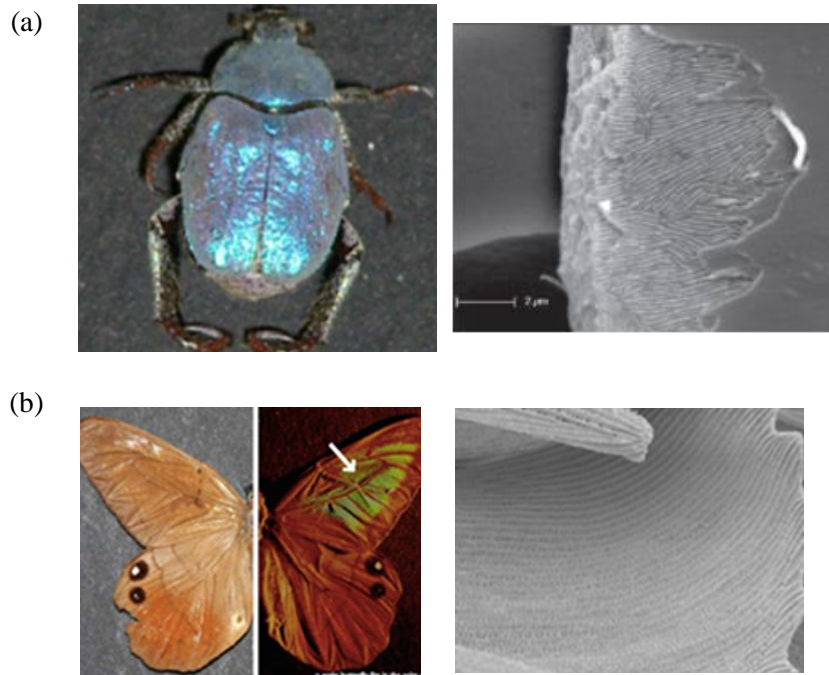


Figure 4.1. Three types of photonic crystals: a) one-dimensional (multilayer stack); b) two-dimensional (PhC slab) c) three-dimensional (colloidal crystals, opals). The selection refers to the dimension of periodicity.

The common feature for all photonic crystals is the photonic band gap. It is an optical analogue of the electronic bandgap in semiconductors. In semiconductor crystals, an atomic lattice possesses the periodic potential. If it is too high for electrons to pass them through, they are scattered by atoms. We say then, the structure exhibits an energy band gap for those electrons not allowed propagating inside the structure.

In photonic crystals, instead of atoms there are microscopic dielectric media with different dielectric constants (alternatively refractive indexes). The difference between dielectric constants (refractive indexes) works as periodic potentials in semiconductors. If it is enough, the photons are reflected at the interface. It means that for these photons exists photonic band gap. For the white light, this phenomenon is visible with the naked eye as one, desired reflected light colour.

Now a day, all three structures are fabricated at laboratorial conditions and their properties have been deeply investigated respecting their future and related applications. Moreover, photonic crystals exist around us as components of animal bodies like wings, skin and feathers. The best – known example of natural storage of photonic crystals is a blue butterfly from Morpho-family. Less known are some of tropical fishes, hummingbirds, moths, beetles and peacocks. Nevertheless, the natural photonic crystals have been steel inspiring the researchers for further investigations and looking for new materials and fabrication methods of their artificial counterparts with similar optical properties. (Bartl 2014).



(c)

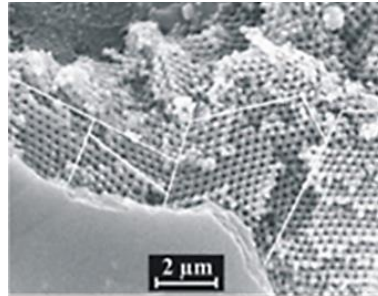


Figure 4.2. The natural storages of photonic crystals a) *Hoplia coerulea* (Deparis 2008), b) *Pierella luna* (Grant 2004), c) weevil *Pachyrrhynchus congestus pavonius* (Welch 2007).

Since the selection in Figure 4.2. is nowadays valid and commonly applied in numerous publications, there is worthy to mentioned here that photonic band gap materials and photonic structures are terms that can be used alternatively. Many structures, metallic or dielectric, that exhibit one – dimensional, two – dimensional or three – dimensional periodicity can be called photonic crystals (J.-M. Lourtioz 2005), whereas the former definition of photonic band gap materials refers only to those that exhibit omnidirectional photonic band gap. This definition was proposed by Yablonovitch in 1990, whose publication (Yablonovitch 1990) initiated intensive investigations on photonic crystals. In 2007, he proposed two criteria to define photonic crystals as structures possessing (Yablonovitch 2007):

- high index contrast (at least 2);
- 2D or 3D periodicity.

Since early 90's, both definition has evaluated, what has been a result of intensive investigations, theoretical as well as experimental, on photonic crystals properties. Thus, photonic band gap is not the only one light phenomenon observable in photonic crystals. There are optical phenomena such as super lens, or super prism effects, which were confirmed experimentally (Luo *et al.* 2004) and enable new promising applications for photonic crystals.

Below, there are listed the fundamental terms referring to photonic crystals. They are intensively used to describe the structure and light phenomena within photonic crystals:

- **unit cell** (the Wigner-Zeiss cell) is a spatial domain where each

point is closer to the selected base point than to any other neighbour base points (Sukhoivanov and Guryev 2009). It is defined by the shape and the permittivity or refractive index distribution inside the cell. The shape of unit cell determined the type of lattice and features can be expanded over whole lattice. It is stipulated by the simplicity of the mathematical definition.

- **the lattice vectors** transformed the defined unit cell into the similar one. In fact, the whole lattice is created by such transformation. The lattice vector is defined by the primitive lattice vectors; whose number is the same as the dimension of structure. They are termed by a_1 , a_2 , a_3 , and relate to the lattice vector R as follows:

$$\mathbf{R} = l\mathbf{a}_1 + m\mathbf{a}_2 + n\mathbf{a}_3 \quad (4.1)$$

where l , m , n are integers.

- **reciprocal lattice;**
- **the reciprocal lattice vector (G)** is defined by relation to R as:

$$\mathbf{G} \cdot \mathbf{R} = n2\pi \quad (4.2.)$$

By analogy to the lattice vector, the reciprocal lattice vector can be defined as linear combination of reciprocal basic vectors, i.e.:

$$\mathbf{G} = l\mathbf{b}_1 + m\mathbf{b}_2 + n\mathbf{b}_3 \quad (4.3)$$

G substitution in eq. 4.2 by applying eq.4.3 provides following interacting between G and R

$$\mathbf{G} \cdot \mathbf{R} = (l\mathbf{a}_1 + m\mathbf{a}_2 + n\mathbf{a}_3) \cdot (l'\mathbf{b}_1 + m'\mathbf{b}_2 + n'\mathbf{b}_3) = N \cdot 2\pi \quad (4.4)$$

With respect to the scalar multiplication, i.e. $a_i \cdot b_i = \delta_{i,j}2\pi$ ($\delta_{i,j}$ is called Kronecker delta and equal to 1 for $i = j$, or 0 otherwise), the relation between b_i and a_i are determined by following formulas:

$$\mathbf{b}_1 = 2\pi \frac{a_2 \times a_3}{a_1 \cdot a_2 \times a_3} \quad (4.5a)$$

$$\mathbf{b}_2 = 2\pi \frac{a_3 \times a_1}{a_1 \cdot a_2 \times a_3} \quad (4.5b)$$

$$\mathbf{b}_3 = 2\pi \frac{a_1 \times a_2}{a_1 \cdot a_2 \times a_3} \quad (4.5c)$$

- **Brillouin zone** is the counterpart of the Wigner-Zeits cell in a reciprocal lattice.

The photonic band gap phenomenon has been confirmed experimentally and described theoretically. The theoretical description involves complicated calculations, which usually are supported by advanced, numerical techniques.

The principles of photonic band gap refer to Helmholtz formalism derived from the Maxwell's equations. The next subchapter highlights the mathematical aspects of photonic bandgap theory. The deep mathematical analysis was performed for one-dimensional case and further expanded to two-dimensional and three-dimensional case by brief analysis of light interactions with 2D and 3D periodic structure.

4.1.1 Light interaction with 2D photonic crystals

Although, 2D photonic crystals do not possess the complete photonic band gap, they exhibit other important characteristic of photonic crystals such as nontrivial Brillouine zones, topological sensitivity to minimum index contrast, and they can be used in most photonic-crystal devices (Johnson and Joannopoulos, 2003). In two-dimensional structure, there are two possible modes of light propagating in-plane of periodicity: TM (transverse magnetic), when the magnetic field is in $(x-y)$ plane that is the plane of periodicity, and the electric field is perpendicular to it, and TE (transverse electric), which corresponds to in-plane electric field and the vertical magnetic field. The propagating mod relates to the topology of 2D structure. There are two basic two – dimensional topology: high index rods surrounded by low-index matrix, and low-index holes in a high-index matrix. Figure 4.3. shows both structures with the associated band diagrams. Both structures exhibit the hexagonal lattice, which provides the largest gap.

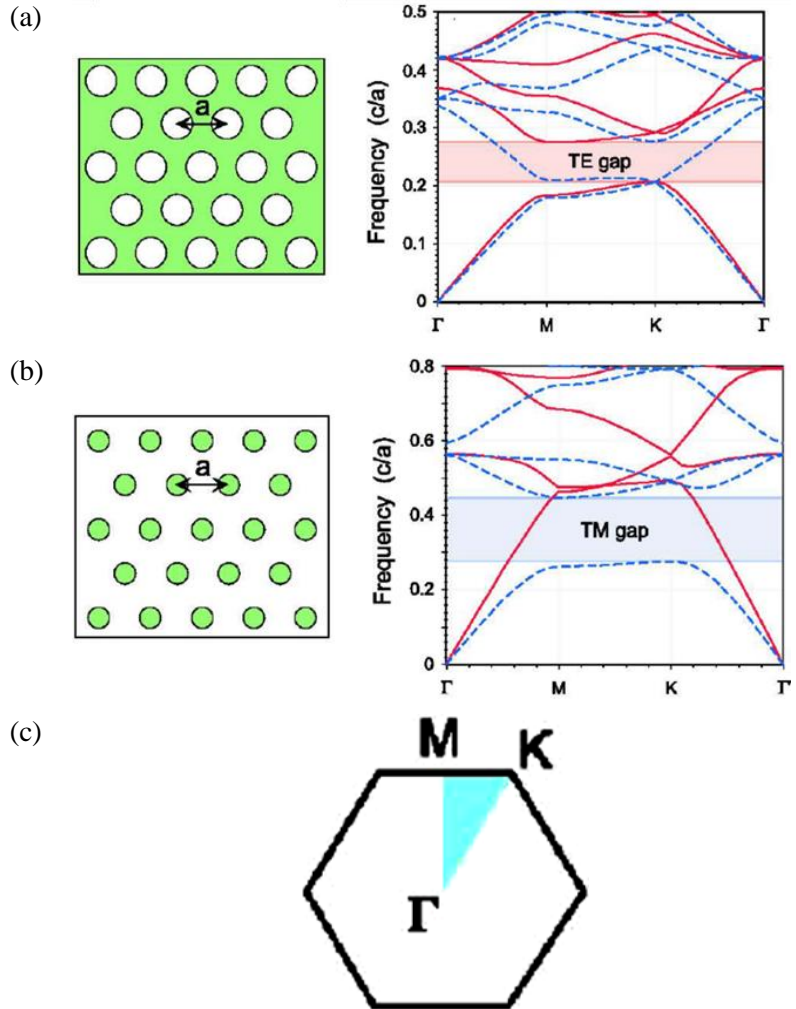


Figure 4.3. Schemes of two fundamental photonic crystals structure a) low-index holes in a high-index matrix b) high-index rods array embedded in a low-index matrix; c) the hexagonal unit cell with depicted light-grey area referring to the light-grey area in the band diagrams. Also, the letters Γ , M, K refer to the letters at the horizontal axes. (Johnson and Joannopoulos 2003).

Figure 4.3.c shows the hexagonal unit cell. The light-grey area depicts the first Brillouin zone, whereas the letters Γ , M, K. The propagating mode within a structure relates to its type. Hence, the array of low-index holes in a high-index matrix supports TE light propagation, whereas the

high-dielectric rods in low-index matrix support TM light propagation. However, there is possible to design a structure that will exhibit the photonic band gap for one desired frequency (ω)/wavelength (λ). For instance, the period of structure that possesses photonic band gap for TM mode with mid-gap frequency $\omega = 0,36$ ($\omega = 2\pi c/a$) and the wavelength 1,55 μm , refers to $a = 0,56\mu\text{m}$.

Photonic crystal slab

The simplest way to realize two-dimension photonic-crystal phenomena in three dimensions is to produce photonic crystal slab i.e. a crystal with two-dimensional periodicity and finite height (Johnson and Joannopoulos 2003). It is called quasi-three-dimensional photonic crystal. Its singularity refers to the light propagation within the structure. The light is confined vertically and guided based on index guiding phenomenon, which is generalization of total internal reflection (Johnson and Joannopoulos 2003). The point of index guiding phenomenon corresponds with the fact that the Bloch wave vector $k_{||}$ is a conserved quantity.

Assuming a PhC slab suspended in the air, light interact with its periodic structure in two ways: for frequencies $\omega \geq c \cdot |k_{||}|$, it is reflected, whereas for other frequencies, due to the higher permittivity of the slab than of air, the light is guided through the structure. As in ordinary two-dimensional photonic crystals, there are two modes. In a photonic crystal slab, these is even (TE-like) mode, and odd (TM-like) mode. For PhC slab with a hexagonal arrangement of holes, there exists 26% band gap in even TE-modes, which ranges no guided frequencies. It corresponds not only to odd modes, but to the radiating modes.

Photonic crystal slabs possess two important parameters which influence the existence of photonic band gap: mirror symmetry and the thickness/high of slab. The mirror symmetry allows to consider the photonic band gap separately for even (TE-like) and odd (TM-like) modes. This symmetry can be easily broken by the presence of asymmetric substrate. Nevertheless, this effect is weak for the enough high index contrast, which confines the modes strongly inside the structure.

The high (thickness) of photonic crystal slab cannot be too small (then, the propagating modes will be weakly confined) neither too large (higher-order modes will fill the gap). Its optimal value should

correspond to the half of propagating wavelength (comparable with an averaged index that depends on the polarization) (Johnson and Joannopoulos 2003).

4.1.2 Light interaction with 3D photonic crystals

There are three available topologies supporting complete 3D photonic band gap: diamond-like arrangements of high dielectric “atoms” surrounded by low dielectric matrix, exhibiting dielectric contrast $\varepsilon = 12/1$ and 20% gaps between 2nd and 3rd band; fcc “inverse opal” with low dielectric holes in high dielectric matrix, with the 10%-gap between 9th and 10th band and dielectric contrast $\varepsilon = 12/1$; and the cubic “scaffold” lattice of rods along cube edges, which provide about 7% gap between 2nd and 3rd. The first two topologies refer to fcc (face-centred cubic) lattice, whose fabrication involve various techniques such as layer-by-layer, colloidal self-assembly and holographic lithography.

In layer-by-layer fabrication, crystal layers are deposited one-by-one, and etched via standard lithographic methods (their major advantage is fine control over placement of defects).

In colloidal self-assembly, the surface forces arrange dielectric spheres into three -dimensional array. To obtain a structure with complete band gap (inverse opal), the spheres are dissolved.

The holographic lithography involved four laser beams interfering with each other to harden light-sensitive resin.

The above two last techniques are particularly noteworthy, due to they provide large-scale 3D crystals (thousands of periods) in a short time.

Colloidal crystals (opals)

The other names for three dimensional photonic crystals are colloidal crystals or opals. ‘Opals’ refers to the natural structure of photonic crystals. It is a milky colored gemstone that illuminated by white light blazes with multicolor pattern. It consists of silica (SiO_2) spheres grouped into domains called crystallites. Such domains differ from each other with a shape and a dimension of spheres. They are embedded in amorphous silica matrix with disordered silica spheres.

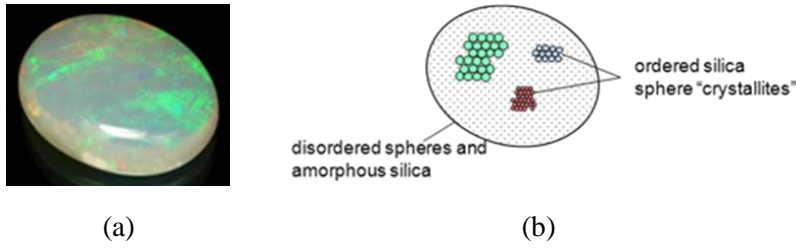


Figure 4.4. (a) natural opals (<http://www.gemselect.com/gem-info/opal/opal-info.php>); (b) schemes of silica spheres arrangement inside matrix of disordered silica spheres (Tilley 2011)

$$m\lambda = 2d\sin\theta_B \quad (4.6)$$

where, λ is a light wavelength in optical medium, d – interplanar distance, m - order of reflecting layer; θ_B is the Brewster's angle.

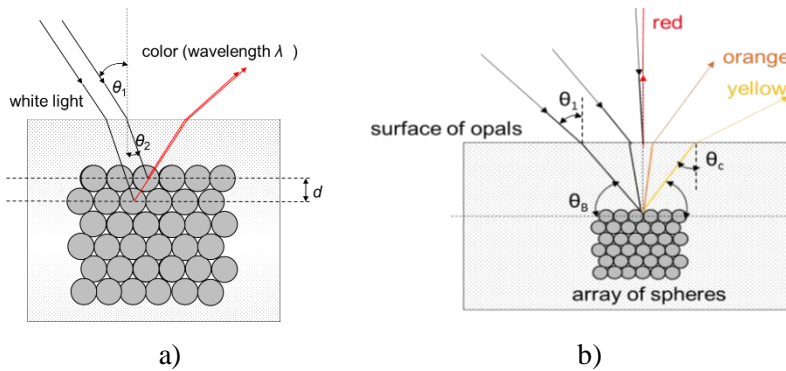


Figure 4.5. White light interaction with opals. Based on (Tilley 2011).

In general, the light interaction with opal-like materials can be explained on the base of natural opals. First, we need to introduce principal relationships and notations uniform with these showed at Fig.4.5. The wavelength propagating in the silica matrix ($n_s = 1.45$) is determined as follow:

$$\lambda = \lambda_0/n_s \quad (4.7a)$$

Here, λ_0 is a wavelength in vacuum

$$\theta_2 = 90^\circ - \theta_B \quad (4.7b)$$

Hence, the Bragg's equation can be written down as:

$$m\lambda_0 = 2n_s d \cos\theta_2 \quad (4.8a)$$

$$m\lambda_0 = 2n_s d \sqrt{1 - \sin^2(\theta_2)} \quad (4.8b)$$

Using the Snell's law given by:

$$\frac{\sin\theta_2}{n_1} = \frac{\sin\theta_1}{n_2} \quad (4.9)$$

For $n_1 = 1$ and $n_2 = n_s$, the wavelength propagating in the air is determined as:

$$m\lambda = 2d \sqrt{n_s^2 - \sin^2(\theta_1)} \quad (4.10)$$

For light passing the interface between two media with arbitrary refractive indexes n_1 and n_2 eq. (4.10) takes the form:

$$m\lambda = 2d \left(n_2^2 - n_1^2 \sin^2(\theta_1) \right)^{1/2} \quad (4.11)$$

The maximal length of reflected light beam corresponds with the incident angle equal to 0° and $m = 1$.

The natural opals illuminated by white light, usually reflect view colors simultaneously. It is possible because crystallites differing from each other with diameter of silica spheres.

The internal structure of artificial opals is more ordered then in their natural counterparts (Fig.4.6)

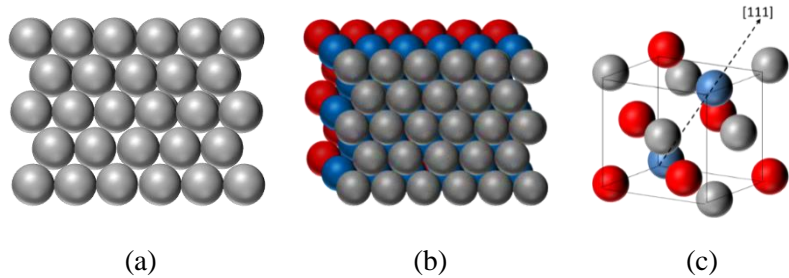


Figure 4.6. a) A single layer with a hexagonal arrangement of spheres b) the multilayer structure, c) the cubic unit cell of an artificial opal. Based on (Tilley 2011)

For the structure with rigid spheres, the interplanar distance d_{111} refers to the diameter of spheres D as follows:

$$d_{111} = D \sqrt{\frac{2}{3}} \quad (4.12)$$

d_{111} defines the plane parallel to the surface of the film. There are other meaningful planes participating at the interaction with white light. These are: (220), (200), (-111). The interplanar distance is determined by Miller's indexes (h, k, l) and diameter of colloids as follow:

$$d_{111} = D \sqrt{\frac{2}{h^2+k^2+l^2}} \quad (4.13)$$

Regarding the at least two structures of 3D photonic crystals, there is necessary to define effective refractive index:

$$n_{eff} = \sum f_i n_i = \frac{\lambda_1}{\lambda_2} = \frac{\cos\theta_1}{\cos\theta_c} \quad (4.14)$$

Here, λ_l and λ_n are light wavelengths in the air and in the direction that is determined by the angle θ_c , respectively; n_i is the refractive index of each component, and f_i is the filling factor (the volume fraction) of each component.

Equations 4.15 describe the response of the plane d_{111} to the incident light:

$$\lambda_{111}(\theta) = 2d_{111} \sqrt{n_{eff}^2 - \sin^2\theta_1} \quad (4.15a)$$

$$\lambda_{111}^{max} - \lambda_{111}^{min} = \left(1 - \sqrt{1 - \frac{1}{n_{eff}^2}}\right) \lambda_{111}^{max} \cong 0.25 \lambda_{111}^{max} \quad (4.15b)$$

The wavelengths λ_{111}^{max} and λ_{111}^{min} correspond to the reflected beams leaving the opal structure in the parallel and horizontal direction to the interface. Equation 4.15b determines the range of reflected wavelengths.

4.2. Mathematical description of photonic band-gap effect

The photonic band gap refers to the range of frequencies, which cannot propagate through a periodic structure. The periodicity determined the range of wavelengths that are prohibited to propagate inside it. The photonic band gap can be assessed based on the photonic band diagram depicted the band structure of photonic crystals.

To find the band structure of photonic crystal means the same as to find the eigenfrequencies and associated eigenmodes of the Helmholtz equation. Its general formula takes the following form (Sukhoivanov and Guryev 2009):

$$\nabla^2 \mathbf{E}_0(\mathbf{r}) + \varepsilon_r(\mathbf{r}) \frac{\omega^2}{c^2} \mathbf{E}_0(\mathbf{r}) = \mathbf{0} \quad (4.16)$$

Here, ω is the radiation angular frequency \mathbf{k} is the radiation wave vector, ε_r is the relative permittivity. The relationship between $\mathbf{E}_0(\mathbf{r})$ and the electric field vector is described as:

$$\mathbf{E}(\mathbf{r}, t) = \mathbf{E}_0(\mathbf{r}) \exp(i(\mathbf{k}(\mathbf{r}) \cdot \mathbf{r} + \omega t)) \quad (4.17)$$

1D structure

For one-dimensional periodic structure illuminated by electromagnetic wave, which propagates along OX axis, equation 4.1. can be written as follow:

$$\frac{\partial^2 E_z(x)}{\partial x^2} + \varepsilon_r(x) \frac{\omega^2}{c^2} E_z(x) = 0 \quad (4.18)$$

This equation allows determining the electric field distribution in subsequent layers of one-dimensional periodic structure. To determine the associated band structure, following steps should be overtaken:

- To find the band structure; there is better to use the magnetic field instead of the electric field. Hence, eq. (4.18) can be written as:

$$\frac{\partial}{\partial x} \frac{1}{\varepsilon(x)} \frac{\partial}{\partial x} \mathbf{H}(x) + \frac{\omega^2}{c^2} \mathbf{H}(x) = 0 \quad (4.19)$$

- Regarding the Bloch theorem, $\mathbf{H}(x)$ should be defined as:

$$\mathbf{H}(x) = h_{k,n}(x) \exp(i \cdot \mathbf{k} \cdot x) \quad (4.20)$$

$h_{k,n}(x)$ is a periodic function with periodicity of lattice corresponding to wave vector \mathbf{k} and the state number n .

- because $\varepsilon(x)$ and $\mathbf{H}(x)$ are periodic functions, both of them should be expanded to Fourier series as follows:

$$\mathbf{H}(x) = \sum_G h_{k,n}(\mathbf{G}) \cdot \exp(i \cdot (\mathbf{k} + \mathbf{G}) \cdot x) \quad (4.21)$$

$$\frac{1}{\varepsilon(x)} = \sum_{G'' \in G} \chi(\mathbf{G}'') \cdot \exp(i \cdot \mathbf{G}'' \cdot x) \quad (4.22)$$

Here, $\chi(\mathbf{G}'')$ are Fourier expansion coefficients of the inverted dielectric function.

In the next step, eq.4.21 and eq.4.22 are applied to eq. 4.19. In fact, eq. 4.19. takes the form (Sukhoivanov and Guryev 2009):

$$\sum_{G''} \frac{\partial}{\partial x} \chi(\mathbf{G}'') \cdot \exp(i \cdot \mathbf{G}'' \cdot x) \frac{\partial}{\partial x} \sum_{G'} h_{k,n}(\mathbf{G}') \exp(i \cdot (\mathbf{k} + \mathbf{G}') \cdot x) + \frac{\omega^2}{c^2} \sum_G h_{k,n}(\mathbf{G}) \cdot \exp(j \cdot (\mathbf{k} + \mathbf{G}) \cdot x) = 0 \quad (4.23)$$

By taking the derivatives, combining the exponents, and with respect to $G = G' + G''$, eq.4.5 can be modified as follow (Sukhoivanov and Guryev 2009):

$$\sum_G \sum_{G'} \chi(\mathbf{G} - \mathbf{G}') \cdot h_{k,n}(\mathbf{G}') \exp(i \cdot (\mathbf{k} + \mathbf{G}) \cdot x) \times (i \cdot (\mathbf{k} + \mathbf{G}') \cdot i \cdot (\mathbf{k} + \mathbf{G})) + \frac{\omega^2}{c^2} \sum_G h_{k,n}(\mathbf{G}) \cdot \exp(i(\mathbf{k} + \mathbf{G}) \cdot x) = 0 \quad (4.24)$$

The projection to the basis $\exp(i \cdot (\mathbf{k} + \mathbf{G}) \cdot x)$ results in final equation determined as follow:

$$-\sum_{G'} \chi(\mathbf{G} - \mathbf{G}') ((\mathbf{k} + \mathbf{G}') \cdot (\mathbf{k} + \mathbf{G})) \cdot h_{k,n}(\mathbf{G}') + \frac{\omega^2}{c^2} h_{k,n}(\mathbf{G}) = 0 \quad (4.25)$$

Equation 4.25. is called master equation for one-dimensional photonic crystals. Its main peculiarity is the independence from the coordinates. All variables depend on the reciprocal lattice. To find the right solution of eq.4.25, the differential operator should be represented in the matrix form (eq.4.27). Then, the final solution of the problem corresponds to its eigenvalues.

$$\hat{\theta}_{G,G'} = \chi(\mathbf{G} - \mathbf{G}') ((\mathbf{k} + \mathbf{G}') \cdot (\mathbf{k} + \mathbf{G})) \quad (4.26)$$

$$\hat{\theta} = \begin{vmatrix} \hat{\theta}_{G_1 G'_1} & \cdots & \hat{\theta}_{G_N G'_1} \\ \vdots & \ddots & \vdots \\ \hat{\theta}_{G_1 G'_N} & \cdots & \hat{\theta}_{G_N G'_N} \end{vmatrix} \quad (4.27)$$

The set of \mathbf{G} and \mathbf{G}' should be identical, what enables the square $\hat{\theta}$ -matrix. Moreover, the $\hat{\theta}$ -matrix is Hermitian matrix. It means that following relationship is valid:

$$\hat{\theta}_{G,G'} = \hat{\theta}_{G,G'}^* \quad (4.28)$$

It means that diagonal-symmetric matrix elements are complex conjugated.

2D and 3D structure

Similar approach can be applied to define band structure for two-dimensional, and three-dimensional cases. Two-dimensional case is a

simplicity of three dimensional. Hence, there is reasonable to derive general equations from three-dimensional structure, and modify them for a two-dimensional. The Helmholtz (wave) equation in three dimensions, for the electric and magnetic field, is defined as:

$$\frac{1}{\varepsilon(\mathbf{r})} \nabla \times \{ \nabla \times \mathbf{E}(\mathbf{r}) \} = \frac{\omega^2}{c^2} \mathbf{E}(\mathbf{r}) \quad (4.29a)$$

$$\nabla \times \left\{ \frac{1}{\varepsilon(\mathbf{r})} \nabla \times \mathbf{H}(\mathbf{r}) \right\} = \frac{\omega^2}{c^2} \mathbf{H}(\mathbf{r}) \quad (4.29b)$$

where \mathbf{r} is a 3D vector in the coordinate space.

Since the considerations are performed for periodic structure, $\mathbf{E}(\mathbf{r})$ and $\mathbf{H}(\mathbf{r})$ are periodic functions, which should be described with respect to Bloch theorem as:

$$\mathbf{E}(\mathbf{r}) = \mathbf{E}_{kn}(\mathbf{r}) \cdot e^{i\mathbf{k}\mathbf{r}} \quad (4.30a)$$

$$\mathbf{H}(\mathbf{r}) = \mathbf{H}_{kn}(\mathbf{r}) \cdot e^{i\mathbf{k}\mathbf{r}} \quad (4.30b)$$

The indices indicate, that the periodic functions are different for each wave vector \mathbf{k} and number of eigenstate n . Because of periodicity, the functions satisfy following equations:

$$\mathbf{E}_{kn}(\mathbf{r} + \mathbf{R}) = \mathbf{E}_{kn}(\mathbf{r}) \quad (4.31a)$$

$$\mathbf{H}_{kn}(\mathbf{r} + \mathbf{R}) = \mathbf{H}_{kn}(\mathbf{r}) \quad (4.31b)$$

where \mathbf{R} is the lattice vector.

As in 1D case, the periodic functions (eq.4.19) should be expanded to Fourier series over reciprocal lattice vectors. Then, eq. 4.19 can be defined in the wave vectors space instead of coordinate space as follow:

$$\mathbf{E}_{kn}(\mathbf{r}) = \sum_{\mathbf{G}} \mathbf{E}'_{kn}(\mathbf{G}) \exp(i(\mathbf{k} + \mathbf{G}) \cdot \mathbf{r}) \quad (4.32a)$$

$$\mathbf{H}_{kn}(\mathbf{r}) = \sum_{\mathbf{G}} \mathbf{H}'_{kn}(\mathbf{G}) \exp(i(\mathbf{k} + \mathbf{G}) \cdot \mathbf{r}) \quad (4.32b)$$

where \mathbf{G} is the reciprocal lattice vector.

Moreover, the dielectric function should be expanded to the Fourier series as:

$$\frac{1}{\varepsilon(\mathbf{r})} = \sum_{\mathbf{G}} \chi(\mathbf{G}) \exp(i\mathbf{G} \cdot \mathbf{r}) \quad (4.33)$$

$\chi(\mathbf{G})$ are Fourier expansion coefficients, which depend on the reciprocal lattice vectors. Applying eq. 4.33 and 4.32 to eq.4.29, the Helmholtz equations for the electric and magnetic field in vector representation of reciprocal lattice are defined as follows:

$$-\sum_{\mathbf{G}'} \chi(\mathbf{G} - \mathbf{G}')(\mathbf{k} + \mathbf{G}') \times \{(\mathbf{k} + \mathbf{G}') \times \mathbf{E}_{kn}(\mathbf{G}')\} = \frac{\omega_{kn}^{(E)2}}{c^2} \mathbf{E}_{kn}(\mathbf{G}) \quad (4.34a)$$

$$-\sum_{\mathbf{G}'} \chi(\mathbf{G} - \mathbf{G}')(\mathbf{k} + \mathbf{G}') \times \{(\mathbf{k} + \mathbf{G}') \times \mathbf{H}_{kn}(\mathbf{G}')\} = \frac{\omega_{kn}^{(H)2}}{c^2} \mathbf{H}_{kn}(\mathbf{G}) \quad (4.34b)$$

These equations are called master equations for 3D photonic crystals. Their solutions refer to the eigenstates of photonic crystal, and can be determined by creating the matrix differential operator and searching its eigenvalues.

In two-dimensional photonic crystals, light propagation in-plane of structure is considered based on *the couple modes theory*. The theory assumes two possible light modes: TE and TM. For each of them, the band structure should be calculated separately by following the procedure below. The Helmholtz equations for 2D case are defined as follow:

$$-\left\{ \frac{\partial}{\partial x} \frac{1}{\varepsilon(\mathbf{r}_{||})} \frac{\partial}{\partial x} + \frac{\partial}{\partial y} \frac{1}{\varepsilon(\mathbf{r}_{||})} \frac{\partial}{\partial y} \right\} H_Z(\mathbf{r}_{||}) = \frac{\omega^2}{c^2} H_Z(\mathbf{r}_{||}) \quad (4.35a)$$

$$-\frac{1}{\varepsilon(\mathbf{r}_{||})} \left\{ \frac{\partial^2}{\partial x^2} + \frac{\partial^2}{\partial y^2} \right\} E_Z(\mathbf{r}_{||}) = \frac{\omega^2}{c^2} E_Z(\mathbf{r}_{||}) \quad (4.35b)$$

Here, it was assumed that the light propagates in-plane of periodic structure. It means, that the propagation direction is determined by the vector $\mathbf{r}_{||}$ (X,Y). Hence, only the Z-component of electric field, E_z , and magnetic field, H_z , doesn't vary during propagation.

$$-\sum_{\mathbf{G}'_{||}} \chi(\mathbf{G}_{||} - \mathbf{G}'_{||}) |\mathbf{k}_{||} + \mathbf{G}'_{||}|^2 \mathbf{E}_{zk_{||}n}(\mathbf{G}'_{||}) = \frac{\omega_{k_{||}n}^{(E)2}}{c^2} \mathbf{E}_{zk_{||}n}(\mathbf{G}_{||}) \quad (4.36a)$$

$$-\sum_{\mathbf{G}'_{||}} \chi(\mathbf{G}_{||} - \mathbf{G}'_{||}) (\mathbf{k}_{||} + \mathbf{G}_{||}) (\mathbf{k}_{||} + \mathbf{G}'_{||}) \mathbf{H}_{zk_{||}n}(\mathbf{G}'_{||}) = \frac{\omega_{k_{||}n}^{(H)2}}{c^2} \mathbf{H}_{zk_{||}n}(\mathbf{G}_{||}) \quad (4.36b)$$

By analogy to two previous cases, each of equations 4.36 is called master equations for 2D photonic crystal.

The photonic band gap relates to a periodic structure of optical medium and results in a reflected wavelength comparable with the periodicity.

The complete photonic band gap refers to the range of frequencies (ω) in which there are no solution (real \vec{k}) satisfying (eq.4.1) for any \vec{k} above and below the band gap. There is also incomplete photonic band gap that exist over a subset of all possible wave vectors, polarization, and/or symmetries (Johnson and Joannopoulos 2003).

To find the photonic band structure means the same as to find eigenfrequencies and associated eigenmodes of the wave equation for the perfect photonic crystal, i.e. an infinitely extended periodic array of dielectric material. The equations given below were derived

In this subchapter, the main mathematical aspects of photonic band gap will be highlighted only for one-dimensional structure. The other two cases, a two-dimensional structure and three-dimensional structure will be only briefly described. Here, the general theoretical overview of photonic band gap will be performed only in one-dimensional problem, assuming the origin of photonic crystals are the same for all three structures, and the its main problem can be easily understandable by analysing the simplest one – dimensional case. The 2D and 3D cases will be briefly discussed later with references to the one-dimensional analysis.

The above considerations highlight only the origin of photonic band gap and provide the theoretical back ground. In practice, present advanced photonic devices desire precise and fast calculations, which currently can be performed by using advanced numerical methods, such as:

- transfer matrix techniques;
- *finite-difference time domain* (FDTD) and *finite-difference frequency-domain* (FDFD) simulations;
- photonic band-gap calculations on plane wave expansion;

For some particular cases, there is allowed to apply analytical or semi-analytical approach. One of possible semi analytical approach refers to semi – *perturbation theory*.

4.3. Photonic crystals as strain sensors

4.3.1 Strain – sensitivity of photonic crystal slabs (PhCSs)

Most experiments referring to opto-mechanical properties of photonic crystal slabs were designed considering their future application as components of micro-opto-electro-mechanical systems (MOEMS). Park and Lee (Park and Lee 2004) used a photonic crystal slab prepared with polydimethylsiloxane (PDMS) matrix and silicon pillars arranged into

hexagonal lattice. Thanks to the high-symmetrical configuration, high index contrast and high-dielectric contrast (the refractive index of PDMS is $n_{PDMS}=1.5$ and for silicon $n_{Si}>3$, the dielectric constants are 2.4 and 12, respectively) the structure was able to create photonic band gap. The sample was stretched and released alternatively by two nano-/microelectromechanical system actuators placed at the both sides of the sample.

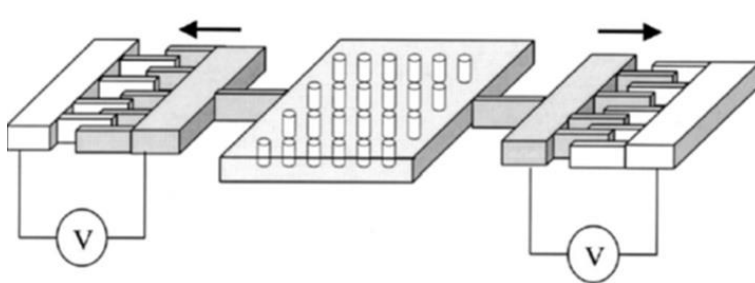


Figure 4.7. The experimental setup to test strain-sensitivity of photonic crystal proposed in (Park and Lee 2004). The sample is placed between two actuators, which stretch it symmetrically.

The external force was applied along Γ -K direction. The visible changes of light behaviour were observable in the perpendicular direction (Γ -M). Additionally, the experimental results were supported by numerical calculations with finite-difference time-domain (FDTD) method.

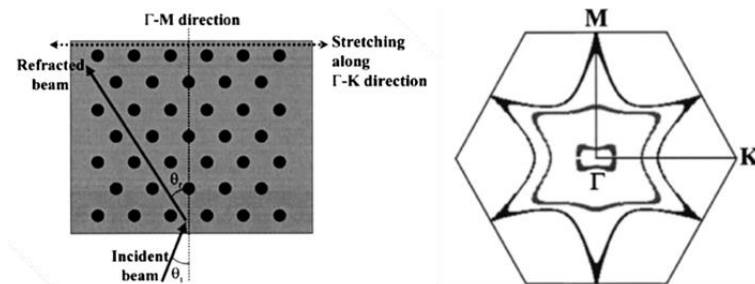


Figure 4.8. a) Light propagation outside and inside the experimental structure; θ_i is the incident angle and θ_r is the refractive angle; b) the first Brillouine zone of the experimental structure with three dispersion curves inside: the outer curve (non-elongated sample), the

middle curve (sample with the 5% elongation) and the inner curve (sample with 10% elongation). (Park and Lee 2004)

The non-deformed photonic crystal slab exhibits extremely negative refractive angle for small incident light angles (Fig. 4.9.a). The elongation motions changed the period of the photonic crystal structure. In fact, the light behaviour inside the sample changed. For the 5% of elongation, the refractive angle decreased significantly, while for the 10% elongation was close to 0° . Also, the difference between refractive angles for different incident angle decreased significantly by stretching the sample.

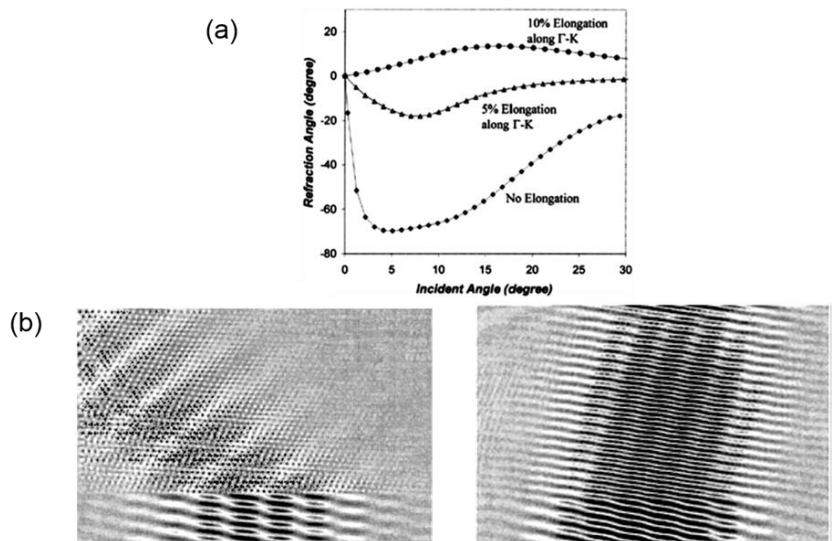


Figure 4.9. a) Results of numerical computations; b) the simulations of Gaussian beam diffraction inside the perfectly triangular structure (left) and the distorted structure after 10% elongation (right). (Park & Lee 2004).

Another approach is demonstrated in (Suh et al. 2003). The authors designed a photonic crystals system for the application as sensitive component for nanoscale deformations in MOEMS. The system comprised two identical photonic crystal slabs with parallel arrangement against each other (Fig.1.10 a). Each of them included the array of

cylindrical holes aggregated into the square lattice. Both structures had high-dielectric contrast equal to 12 and thickness of $0.55a$ (a is the shortest distance between centres of two holes). The radius of holes is equal to $0.4a$ and the space h between the slabs is of $1.35a$. The maximum displacement sensitivity corresponds to the maximum reflectance of each slab i.e. minimum transmittance and minimum optical losses. Hence, the values of the parameter should be fitted to these conditions.

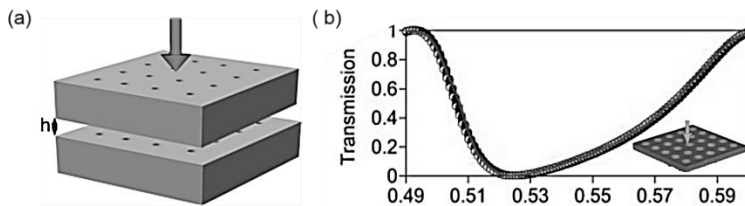


Figure 4.10. a) The experimental system comprised of two slabs set parallel to each other, b) transmission spectrum regarding the light frequency illuminated the single slab (the inset picture). (Suh et al 2003)

The authors introduced a definition of the sensitivity for displacement. It is defined as the minimum displacement δh needed to switch the transmission coefficients from 20% to 80%.

Despite papers about experimental investigations on strain sensitivity photonic crystal slabs, several papers consider the same aspect theoretically (Kim and Gopalan 2001; Bermel and Warner 2002; Jun and Cho 2003). For instance, Jun and Cho consider the optical response of 2D photonic crystal with applied uniaxial tension. They performed numerical calculations based on the least-square (MLS) method. Hence, they confirmed the relationship between optical response and structural deformation induced by distortion of interfaces between inclusions and matrix. The considered model was a two-dimensional triangular photonic crystal. It consisted of silicon matrix and cylindrical air rods. The strain sensitivity was assessed for three types of deformations: pure shear, simple shear and uniaxial tension. Each deformation induced structural changes as depicted below (Fig.4.11):

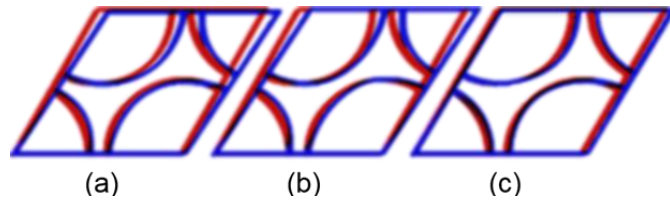


Figure 4.11. Non-deformed (red) and deformed (blue) unit cells of 2D triangular photonic crystal with cylindrical air rods: a) pure shear, b) simple shear, c) uniaxial tension. (Jun and Cho 2003).

Further, to find the optical response they prepared schemes of symmetrical points and zones in the reciprocal lattice of non-deformed and deformed photonic crystals.

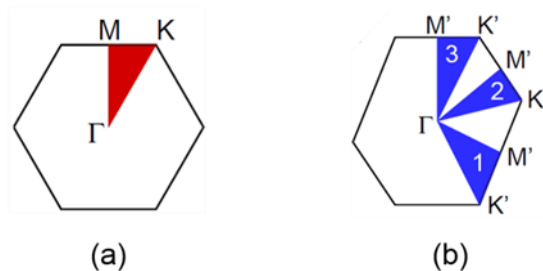


Figure 4.12. Schematic diagrams of symmetry points and zones in the reciprocal lattice of (a) non-deformed and (b) deformed photonic crystals. (Jun and Cho 2003).

The simulations showed, that only the uniaxial tension influenced significantly the photonic band gap and introduced the change of filling factor over 2% (from $f = 100\%$ to 97.61%).

Several papers present two-dimensional photonic crystals as active optical media with abilities to light beam manipulation e.g. Tandon et al. described superprism effect (Tandon et al. 2005), Kosaka et al. (Kosaka et al. 1998). observed self-collimating laser beam. All of these papers describe investigations performed with monochromatic, laser light. Unlike them, Popov et al. present the other approach (Bonod et al. 2006). They analyse a two-dimensional periodic structure as a diffraction grating. They observed that the interaction with white light results in the

multicolour blazing pattern on the illuminated surface. This effect is called blazed effect and refers to the photonic structures obtained by wet-etching.

4.3.2 Mechanochromic properties of colloidal crystals

There are many external factors affecting the optical response of colloidal crystals such as: temperature, electric field (Zhao *et al.* 2012), mechanical stress (Zonta *et al.* 2009) and solvents (Chiappini *et al.* 2013). The easiest way to influence the optical response is stretching/compression. It was described by numerous papers, in which the experimental results were verified by simulations. The calculations were summarized by examples of potential applications of photonic crystals.

In 2005, Pursiainen and Baumberg published one of the first papers about strain-sensitivity of artificial opals providing the visible optical response. Their investigations were a response to a rapid progress in investigations on the strain-sensitivity of two-dimensional photonic crystals. They applied the fabrication method of polymeric spheres proposed previously by (Ruhl, Span and Hellmann 2003). The particles consisted of rigid, polystyrene core covered by the double-layer shell. The internal layer was made of poly (methyl methacrylate) (PMMA). The PMMA layer fixed the core to the external layer that was made of polymethylacrylate (PEA). In the compression-moulding process, they obtained hexagonal arrangement of core-shell particles (with diameter of $D = (100\div 300)$ nm) embedded in the PEA matrix. The oval shaped sample possessed diameter equal to 10 cm. Its thickness amounted 250 μ m.

The meaningful parameters like the interplanar distance (d_{111}), the Poisson's ratio, the lattice periodicity and the effective reflective index were determined experimentally. Increasing the applied stress (from 0% to 2%, 4%, 8% and 13%) they measured the transmission and the reflection for the wavelengths ranging from 560nm to 680 nm.

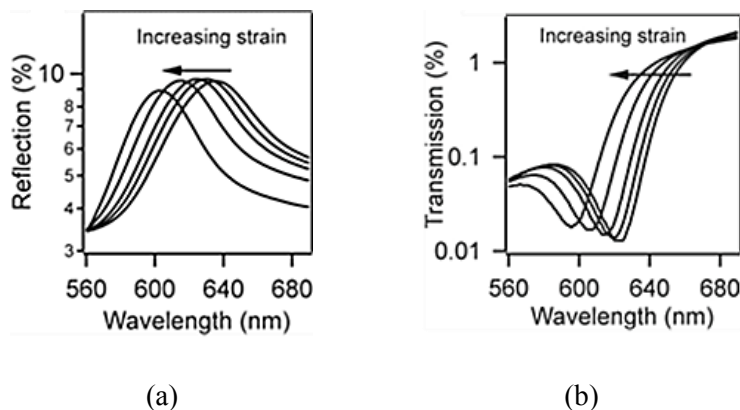


Figure 4.13. The strain influence on: (a) reflection, (b) transmission of sample. (Pursiainen and Baumberg 2005).

Based on the transmission measurements, they determine the strain sensitivity. The sensitivity S refers to the fractional change in transmission for 1% of strain increase. The graph below shows two plots of the sensitivity vs. normalized wavelength for two samples i.e. with absorbing matrix and non-absorbing matrix. It shows the sample with absorbing matrix exhibit the higher sensitivity for strain then the sample with the non-absorbing matrix (the 50% transmission decrease for the 1% strain).

Another approach was presented in (Zonta et al. 2009). The photonic crystal structure contained PS spheres embedded in PDMS matrix. The fabrication ran in three steps (Zonta et al. 2009): the fabrication of PS spheres, self-assembly of PS spheres onto Viton substrate through vertical deposition, infiltration with PDMS matrix. In fact, the photonic crystal sample was composed of PS spheres ($d = 230\text{nm}$) arranged hexagonally (the filling factor for hexagonal arrangement is $f = 0.74$) and PDMS matrix (the mixture of base and curing agent with in the mass ratio 3:1). Next, the sample was elongated. The maximum elongation was $\Delta l = 12\text{ mm}$, which refers to maximum strain $\Delta\varepsilon = 21.4\%$. During elongation, the sample was controlled by two fibres, set above the sample, vertically to its surface (the light incident angle was $\theta = 0^\circ$). One of them illuminated the sample with white light, while the other registered the reflected wavelength. The registered optical signal was converted into the electrical and sent to the computer. The graphs below present the results of measurements.

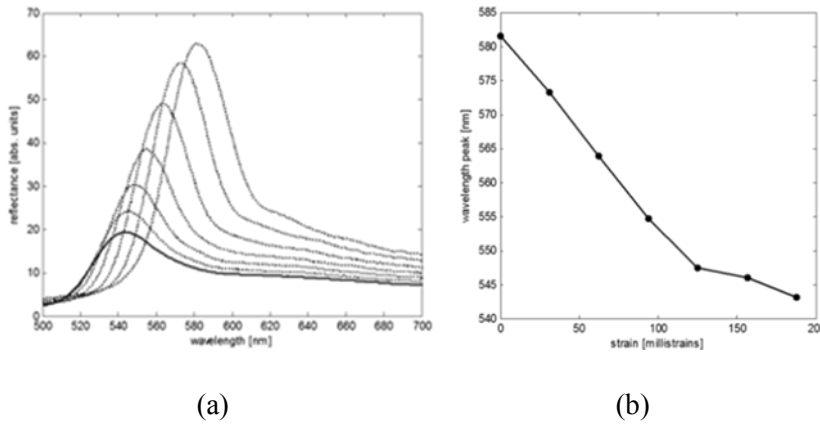


Figure 4.14. a) The dependence between reflectance and reflected wavelength, each curve corresponds to the next step of elongation i.e. the highest reflectance corresponds to the initial state and the lowest reflectance refers to the state with the maximum strain b) the reflected wavelength as a function of the applied strain (Zonta et al. 2009).

Chapter 5

Fabrication of 2D slab

5.1 Introduction

The samples' fabrication is the crucial step of investigations. It is meaningful with respect to a strong relationship between the quality of structure and the results of measurements. The samples' quality is strongly influenced by the techniques, conditions and the materials used. Hence, the detailed procedure described in section 5.2. was proceeded by the description of key features and properties of involved materials, such as: colloidal spheres, monolayer colloidal crystals (MCC), and polydimethylsiloxane (PDMS). The theoretical issues are supported by examples of experiments, which significantly have supported developing their fabrication techniques. These examples could be particularly valuable for optimization the procedure presented in section 5.3.

The current procedure involves three subsequent steps: fabrication of MCC with PS colloidal spheres, fabrication of the MCC replica on the PDMS substrate, and fabrication of inverse MCC replica by wet etching with dimethylformamide (DMF). The fabrication of MCC employ the protocol developed by Sun et al. (Sun et al. 2010), which refers to the self-assembly of polystyrene (PS) spheres. The self – assemble is desired alternative for lithography techniques, since it is low-cost, not demanding special conditions (e.g. clean-room conditions) and suitable for mass production. Furthermore, it is compatible with polymeric colloidal spheres, which are commonly available and non-toxic materials, whose synthesis required only water as a natural solvent (it decreases significantly the total cost of fabrication). High transparency of PDMS matrix enables visibility of effects corresponding to the optical properties of sample, and investigations on the transmission properties of it. Their results were described in the last section as an important source of information about the geometry of the structure.

The sample evaluation was supported by the atomic force microscope (AFM) and the scanning electron microscope (SEM). However, only the AFM provided the exhausting analysis of the sample morphology including images of structure, its 3D simulations, and the measurements of structural parameters such as: the pitch and the depth of grooves. The AFM images and the optical effects observable with the naked eye allowed approaching the sample as a diffraction grating, which structural features can be determined based on the experimental results.

5.2 Materials properties

5.2.1 Monodispersed colloidal spheres

Monodispersed colloidal spheres refer to particles which diameters range from 10nm to 1 μ m. Nowadays, thanks to well-developed fabrication techniques, it is possible to produce them in large quantities and with a uniform size and shape. This is particularly important in investigations on their optical, magnetic, electronic and electrokinetic properties. A recent progress in material science provides many examples of applications of monodispersed colloidal spheres suspension more complex structures created by self-assembly of colloidal spheres. Colloidal spheres can be used for drug delivery, biodiagnostic and combinatorial systems, whereas the more complex structure e.g. a two-dimensional array of nanospheres arranged into hexagonal lattice have been already successfully tested in image processing as an ordered array of microlenses, as a physical mask for evaporation lens, or as a patterned arrays of relief structure to cast elastomeric stamp in soft lithographic techniques (Xia 1996). Moreover, the three-dimensional structures are interesting objects for investigations with regard to their applicability as diffractive elements to fabricate filters, switchers, sensors and PBG, or just to study various, fundamental phenomena such as crystallization, phase transition, melting, fracture mechanics. Such many applications of monodispersed colloidal spheres are resulted from:

- cost-efficient fabrication based on self-assembly techniques
- easily available and low-cost materials such as silica and polymers;
- high-quality, large-domain structure as product of fabrication;

- a tight control over the degree of perfection on the 3D structure, which is significant in electronic applications of crystalline arrays of colloidal spheres.

The spherical shape is not the only one of nanocolloids. However, it is the most appreciated with regard to the following issues:

- most theoretical models that deal with properties of colloidal particles and the interactions between them are usually based on the spherical shape;
- the spherical shape of colloids enables easily tuneable properties by changing parameters such as: the diameter (D), a chemical composition, the bulk structure, the crystallinity (polycrystalline, single crystalline, or amorphous), the surface functional group (thus the interfacial free energy and surface charge density).

Another advantage of spherical shape is its easy adoptability into nucleation and growth process by minimization of interfacial energy. There are three main types of colloidal spheres with respect to their composition i.e. a) solid spheres, b) a core-shell sphere, c) a hollow sphere. Solid spheres exhibit an ability to attach surface groups. In case of silica solid spheres, it is usually terminated in silanol groups ($-\text{Si}-\text{OH}$). For polymer latexes, the surface group span over a diverse range that includes $-\text{NH}_2$, $-\text{COOH}$, $-\text{SO}_4\text{H}$, $-\text{SO}_3\text{H}$, $-\text{OH}$, $-\text{CONH}_2$, $-\text{CH}_2\text{Cl}$.

Fabrication of monodispersed colloidal spheres

There are several techniques invented to fabricate monodispersed colloidal crystals. Up to date, the most effective and prospective seem to be two of them i.e.: controlled precipitation for inorganic (hydrous) oxides, and emulsion polymerization for polymer latexes.

The controlled precipitation is commonly applied for inorganic spheres. It involves two independent steps: the nucleation and growth of the nuclei. To obtain monodispersity of spheres, these steps should be separated from each other i.e. the nucleation should be avoided during the period of growth. The fundamental criteria to fabricate monodispersed colloidal particles were given by LaMer et.al (Zaiser and LaMer 1948). The monomer (a solid or a complex precursor) should be added carefully at a well-controlled rate to avoid passing the level of supersaturation during the growth period. The model proposed by LaMer assumes the growth of nanospheres at the same time and at the same rate until the desired size was attained. Further, this model was

improved and developed with attempt to apply it for silica colloids, what was done by Ströer and Fink. They produced silica spheres with diameter from 50 nm up to 2 μ m by hydrolysing a dilute solution of tetraethyl orthosilicate (TEOS) in ethanol at high pH. Another improvement was proposed by Matijevic and co-workers (Ohmori and Matijevic 1992), (Hsu, Yu and Matijevic 1993), who applied the Ströber's and Fink's technique to obtain monodispersed colloids with various shapes such as: rods, ellipsoids, cubes, using various materials e.g. metal oxides and carbonates. For successful fabrication, control of reaction conditions i.e. the temperature, the pH, the method of mixing the reactants, the concentration of reactants and counterions, plays the crucial role.

Emulsion polymerization is applicable for polymer colloids. This technique involves following components: a monomer, a dispersion medium (usually water), an emulsifier (surfactant), and an initiator (usually water-soluble). The monomer is dispersed as an aqueous emulsion (\sim 1- 100 μ m in diameter) assisted by the emulsifier. Most surfactant molecules exist as micelles (\sim 10nm in diameter). Most of them are swollen by the monomer. Formation of polymer latexes is initiated by decomposition of water-soluble initiator, during which burst of primary free radicals are generated. These radicals polymerize the small amount of monomer that is dissolved in the aqueous phase to form the nucleioligomers in the form of tiny particles. Then, these particles enter the micelles and eventually grow into larger particles until the monomer dissolved in each micelle has been consumed. At the same time, the monomer encapsulated in emulsion droplets provides a supply of repeating units to the growing polymer chains through diffusion (Xia et al. 2000). For latex nanoparticles with diameters equal to 100nm, there are around 1000 macromolecular chains entangled as coils in the spheres. Each of them attracts and ends with a functional group formed by the decomposition of radical initiator. (Xia et al. 2000)

Both techniques are applicable to produce monodispersed polymer colloids of poly (methyl methacrylate) (PMMA) and polystyrene (PS) in large quantities. However, Ward and Friberg tested successfully this method for inorganic colloidal spheres (Ward and Friberg 1989). Generally, the diameter of spheres ranges from 20nm to \sim 1 μ m, but there is possible to obtain polymer colloids with the diameter over 1 μ m by applying methods proposed in (Ugestad et al. 1982) and (Sheu, Asser and Vanderhoff 1987). In their approach, the submicrometer-sized polystyrene beads were obtained in two-step procedure. The first step involved the classical emulsion polymerization method, which was followed by swelling with another monomer supported by aprotic solvent miscible with water. Subsequent polymerization of the encapsulated monomer provides monodispersed latex spheres with

diameters up to several hundreds of micrometers (Xia *et al.* 2000). Moreover, introducing an immiscible monomer into the polymer beads allows fabricating non-spherical particles due to phase separation. In the emulsion polymerization, the properties of latex particles are easily manipulated by changing conditions. For instance, using potassium persulfate as the water-soluble initiator provides latex particles with the negatively charged sulphate group attached at their surface. Alternatively, adding an appropriate component to the monomer provides surface groups such as (-COOH) or (-NH₂).

Interactions between colloidal spheres suspended in liquids

For two centuries, interaction between colloidal spheres has been intensively investigated due to their profound effect on the colloidal dispersion, especially with respect to its stability, crystallization, and flow (Hunter 1993). In case of hard colloidal spheres whose surfaces are electrically neutral, the pairwise potential energy of interaction consists of two terms: the short-range, steric repulsive interaction (Fig. 5.1 a), and long-range (existing over distances of 100nm) attractive interaction that is related to the van der Waals force. The sum of them is plotted in Fig. 5.1 b as a function of distance between two centres of spheres. Additionally, for spheres embedded in a solution containing stray electrolytes, another component should be added. It is called Yukawa potential and refers to the long-range Coulomb repulsion shielded by electrolytes. It is defined by the following formula:

$$U(r) = \frac{(Ze)^2}{(\varepsilon)} \left(\frac{\exp(\kappa a)}{1 + \kappa a} \right)^2 \frac{\exp(-\kappa r)}{r} \quad (5.1)$$

where r is the centre-to-centre distance between the two spheres, Z is the number of charges per sphere, a is the radius of sphere, and ε is the dielectric constant of the dispersion medium.

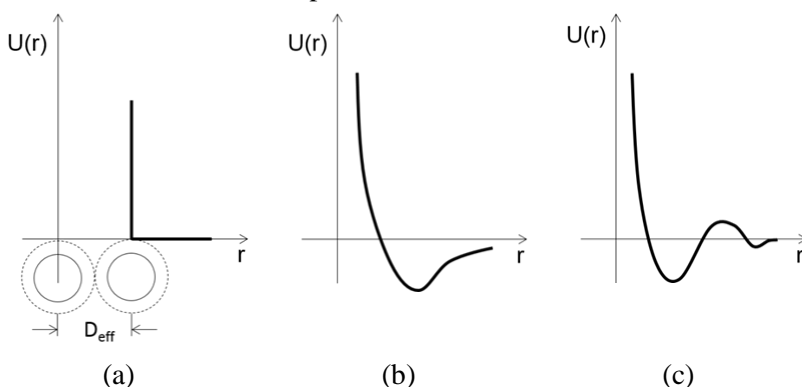


Figure 5.1. The pairwise potential of interaction between

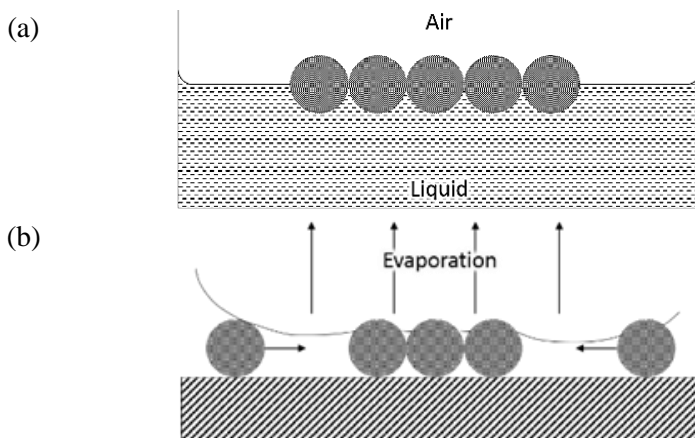
two colloidal spheres: a) hard spheres, b) electrically neutral spheres, c) highly charged spheres or soft spheres. In the ideal model, hard spheres model, there is essentially no interaction between two colloidal spheres until the distance gets equal to D_{eff} , and then the potential energy of repulsion goes effectively to infinity. The curve depicted at (b) refers to the Sogami potential. (Xia et al.2000).

The combination of all three potentials is called Derjaguin-Landau-Vervey-Overbeek (DLVO) potential, which was plotted at Fig. 5.1.c as a function of distance between centers of spheres.

Creation of two-dimensional crystalline array by monodispersed colloidal spheres

Capability of colloidal spheres to self-assembly has been intensively exploited to fabricate two-dimensional and three-dimensional crystalline arrays.

Generally, there are two available substrates to create two-dimensional array of colloidal spheres i.e. liquid and solid, and three techniques to obtain their hexagonal arrangement (all three depicted in Fig. 5.2).



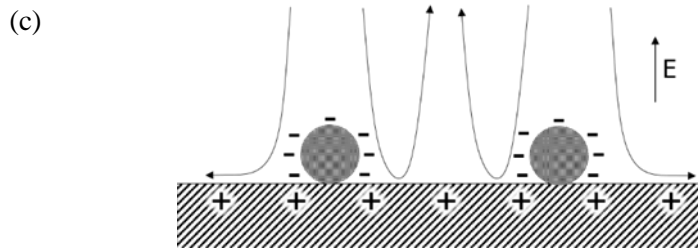


Figure 5.2. Three techniques that provide two-dimensional hexagonal arrays of colloidal spheres: a) at the air-liquid interface via long-range attractive interactions (Wickman & Korley 1998) b) in a thin liquid layer spread on a solid substrate via attractive capillary forces (Denkov et al. 1992); c) on the surface of electrode via electrophoretic deposition (Trau, Saville & Aksay 1996).

In the first approach, colloidal crystals are fabricated as a thin layer of colloidal spheres at an air-liquid interface. Before spreading the spheres onto a liquid surface, the spheres surfaces should be partially modified to obtain them partially immersed into the liquid. The most commonly used liquid to spread the spheres is alcohol. The attractive interactions between spheres are very strong to force the spheres to arrange into two-dimensional hexagonal lattice. The morphology of arrangement usually exhibits the fractal characteristic. However, there are several ways to modify it by tuning e.g. the surface hydrophobicity, the charge density, the size of particles or the electrolytic properties of the underlying liquid. Kondo et al. (Kondo et al. 1995) obtained two-dimensional arrangement of silica spheres with the diameter equal to $1\mu\text{m}$ by controlling the degree of immersion of spheres in the liquid. Another approach was reported by Deckman et al. (Deckman, Dunsmuir and Gruner 1989) and Lenzman et al. (Lenzman et al. 1994), who applied additionally the Langmuir-Blodgett film technique to obtain a large-domain area of hexagonally arranged latex spheres.

The second self-assembly technique (Fig.5.2b) was intensively developed by Nagayama and his co-workers, who exploited the strong attractive interactions between colloidal spheres in a thin, liquid film to arrange them into a two-dimensional, hexagonal array on a solid, flat substrate. They spread the liquid suspension of colloidal spheres onto a solid substrate. At controlled conditions, the liquid was evaporating

slowly causing a hexagonal two-dimensional arrangement of colloidal spheres. The effect was observed by using an optical microscope. The observations confirmed that the spheres organize first in the region where the thickness of liquid layer is comparable to the diameter of colloids (the nucleus). Due to the attractive capillary forces, other colloids were moving toward the nucleus and continuing the arrangement on the flat substrate. The flat, clean and chemically homogeneous surface is desired to obtain highly ordered array with relatively large domain sizes. Other investigations performed by Lazarov and his co-workers (Lazarov et al. 1994) show that liquids can be involved as substrates, as well. Their investigations involved perfluorinated oil (F – oil) or mercury. The method proposed by Lazarov et al. was tested successfully for three dimensional structures by Colvin and his associates (Jiang et al. 1999).

There are many methods to accelerate liquid evaporation. One of them is spin-coating a colloidal dispersion onto a solid substrate. Nevertheless, this method desires adequate conditions to provide a uniform monolayer structure. First, a colloidal dispersion should be able to wet the surface completely. Second, the electrostatic repulsion should exist between the colloidal spheres and the solid substrate. There are two ways to enhance wetting of solid substrate. One is adding a surfactant to the colloidal dispersion. The other relies on pre-coating the substrate with a thin layer of surfactant. Both techniques have been intensively exploited by Van Duyne and his co-workers, which involved them to fabricate single – and double layered structure of colloidal spheres (Hulteen et al. 1999). The valuable observation on this technique were performed by Deckman et al. who noticed that the surfactant introduces the residuals on the substrate, and the domain size decreases with dimension of colloidal spheres (below 50 nm of diameter, the ordering never appears) (Deckman et al. 1988). Multilayer can be obtained at high solid concentration and low spin speed. However, these conditions result in many structural defects.

In the third self-assembly method, colloidal spheres are arranged by external field appearing between two parallel electrodes such as indium tin oxides (ITO)-coated microscope coverslips. Initially, randomly deposited on the anode colloidal spheres influenced by the electrical field, move toward each other and organize into stable, two-dimensional, hexagonal array. This process can be controlled by changing the amplitude of the electric field. It has been approached that

the long-range attractive interaction between colloidal spheres are a result of electrodynamic flows caused by applied electric field, and the passage of ionic current through the structure. This method involves the silica colloids and latex colloids, as well. Nevertheless, it was also tested for three-dimensional structure of silica colloids (Holgado et al. 1999). All three methods described above exhibits some limits. Up to now, each of them provides two-dimensional hexagonal structures with relatively tiny sizes. The largest sample has included fewer than 10000 spheres, which were in physical contact (Xia et al. 2000). Furthermore, there is very hard to tune independently the lattice constant and the size of colloidal spheres. However, the solution for this problem was found by (Hu et al. 1995). In their approach, a high-ordered two-dimensional colloidal structure has been obtained by creating optical standing wave pattern having a regular array of intensity antinodes. The colloidal spheres are driven to the antinode maxima by the optical forces. The investigations performed by Mio and Marr (Mio and Marr 1999) found that the number of involved laser beams determines the dimension of colloidal spheres arrangement.

5.2.2 Monolayer colloidal crystals (MCCs) and their derivatives

Monolayer colloidal crystals (MCCs) are two-dimensional array of monodispersed colloidal spheres. Typical arrangement of micro-/nanospheres of silica or polymers in MCCs refers to the hexagonal close packed (hcp) structure. However, there are examples of MCC with non-close-packed (ncp) structure. The major advantage of hcp arrangement is its thermodynamical stability. The hcp lattice is typical for self-assembly products, which possess a large-area of well-organized micro-/nanospheres with “tolerable defect densities” (Zhang et al. 2010). The other advantage refers to the fabrication techniques based on the self-assembly. Self-assembly techniques are cost-efficient due to low-cost and easily available involved materials (e.g. polymers and silica), for which natural solvent is water. The self-assembly effect is a consequence of balance of three types of interaction between monodispersed colloidal spheres in a liquid suspension i.e. van der Waals forces, steric repulsions, and Coulombic repulsions.

The quality of two-dimensional colloidal crystal depends on experimental conditions. Hence, controlling the temperature, air pressure, solvent, humidity and the contact line has resulted in various

methods to obtain 2D colloidal crystals such as: self-assembly during solvent evaporation (Micheletto, Fokuda and Ohtsu 1995), (Dimitrov and Nagayama 1996) (Kim, Im and Park 2005), self-assembly during spin-coating (Hulteen and VanDuyne 1994), self-assembly at interface, self-assembly in electric field.

Self-assembly assisted by solvent evaporation is the most commonly involved technique to fabricate MCCs. This effect was observed for the first time by Nagayama and his co-workers (Denkov et al. 1992), who remarked self-organizing latex nanoparticles into hexagonal monolayer array in the drop of their suspension put onto a surface. This effect appeared when the thickness of suspension was comparable with the diameter of nanoparticles. Furthermore, they found out that attractive capillary forces and convective transport of nanospheres have the major influence on the self-assembly process, whereas the quality and ordering of nanospheres array is affected by the rate of solvent evaporation and the meniscus shape. The same effect was observed by Micheletto and his associates at a tilted substrate (Micheletto, Fokuda and Ohtsu 1995). Further improvements were reported in (Dimitrov and Nagayama 1996) and, more recently, in (Kim, Im and Park 2005). Moreover, Nagayama with his collaborators developed the dip-coating procedure, which controls the rates of water evaporation and substrate withdrawal. In fact, they fabricated centimetre-sized, homogeneous 2D colloidal crystals. Park et al. proposed new technique “confined convective self-assembly”. They added another glass substrate at a small distance from the substrate. The suspension of nanospheres was injected between the surfaces. When the substrate was lifted up, the hot air was blown toward the meniscus causing water evaporation in the colloidal suspension. Controlling the lift-up rate, they controlled the rate of the meniscus thinning, which influenced the convective assembly and the final colloidal crystal structures.

Derivative structures of monolayer colloidal crystals

MCCs can be involved as a mask or a template in natural (colloidal) lithography to produce derivative structures. Although, the size and shape do not influence the choice of fabrication technique, the usual diameter of colloidal spheres in a template ranges from 200nm to 1000nm. Large sizes of spheres increase the pitch of derivative structure, and weaken the advantages of nanofabrication method. On the other

hand, small sizes make difficulties with colloidal preparation and the self-assembly process. One of available lithographic techniques applied to a MCC template/mask provides one type of following arrays: nanowire arrays, nanoparticles arrays, nanohole arrays, nanodisks, nanopore and nanobowl arrays.

The classification of derivative structures proposed by Zhang et al. (Zhang et al. 2010) respects one of following lithographic techniques applied to a MCC template/mask

- **evaporation**, for which there are two possible approach. One of them refers to direct deposition of functional material on the top of hemispheres of colloidal nanoparticles, what results in Janus particles (particles including bicompartments with different chemical composition). The other one relies on created the top pattern by the particles, which functions as a mask. The major advantage of evaporation refers to the variety of deposited materials, and easily controllable parameters of derivative structure, which depend on the conditions of process and the diameters of involved colloidal particles. Hence, Van Duyne and Haynes performed investigations, which aimed to determine the relationship between particle sizes, shape, interparticle spacing and LSPR (Van Duyne and Haynes 2001).
- **deposition** of functional material covers its physical deposition, and its grow by chemical reaction. Moreover, the material can be deposited selectively on the top surface of colloidal nanospheres, or by infiltration the interspace between adjacent nanospheres. One of the representative techniques is electrodeposition, which is a feasible approach to deposit materials selectively onto electrodes with a MCC template. The application of electrodeposition was demonstrated by Cai et al., who run the process in few steps, as follow: first, they transferred the colloidal crystal onto a conductive substrate such as ITO glass, then they heated the substrate at a certain temperature to enhance the adhesion between the nanospheres and the substrate, and to increase the contact area. In their experiment, the substrate was used as a working electrode in the three-electrode electrolytic cell for electrodeposition. The morphology of product was influenced by the parameters of MCC template and conditions of electrodeposition (Sun et al. 2004). This approach was involved to fabricate an Au Nano

pore films with the various thickness and the various nanopore shape. However, it is also applicable for other metals and metal oxides e.g. Ag, ZnO, CdS, Fe₂O₃, IrO_x (Abdelsalam et al.2007). Another deposition technique is the electrochemical polymerization, which is suitable to prepare an ordered array of conductive polymers (Valesia et al.2006)

- **etching** can be performed in two ways i.e. by reactive ion etching (RIE) (dry etching) and by etching with etchants (wet etching). RIE involves 2D colloidal crystals as a mask, which is treated by relevant ions, e.g. a carbon and polymer template requires oxygenous ions, whereas fluorine ions are appropriate for silica or silicon template. This approach was successfully applied to polymers (Jang et al. 2006), carbon materials (Cong et al.2009), fused silica (Hsu et al. 2008), silicon (Kim et al. 2009) and metals (Weekes et al. 2007) providing various types of pattern, e.g. nanopip array, nanopillar arrays, or nanodisk array. The feature size of prepared nanostructures ranges from 10nm to 100nm.
- **imprinting** is a pattern transfer technique to create a desired pattern on a substrate by its mechanical deformation. The substrate is usually a polymer with regard to its exposure to UV light or heating. If 2D colloidal crystals are involved as a mould, then the parameters of derivative structures are strongly influenced by the parameters of the mould i.e. its geometry, the diameter of spheres. Furthermore, the parameters can be tuned by adjusting experimental conditions. It was confirmed by several papers, which referred to various techniques removing the spheres at different conditions. For instance, Yang et al. (Jang et al. 2008) involved silica nanospheres as a mould, which were deposited on the PS substrate by spin-coating. After heating and removing the spheres, their place was taken by nanovoids, whose arrangement was the same as the arrangement of silica nanospheres, and their parameters (i.e. the depth and the diameter) were influenced by the heating time and the heating temperature. Alternative approach was demonstrated by Sun et al. (Sun, Gonzales et al. 2008), and Jiang (Jiang 2005), who embedded the spheres entirely in the polymer film and applied plasma ion etching to remove its top layer. Subsequently, they removed the nanospheres. In fact, they

obtained an array of voids, whose depth and diameter depend on etching conditions.

- **dewetting** corresponds to the effect supporting the mechanism of evaporation. During evaporation, solvent molecules located at the interface of two contact media are released as the last because of acting capillary forces. Dewetting employs this effect to arrange molecules of easily soluble material (e.g. polymers) around the nanospheres of suspension. After removing the nanospheres, an array of nanorings is created. The parameters of derivative structure depend on the colloidal crystal template i.e. the arrangement of spheres, their embedding depth, but also on the solution concentration. Although, most published papers involved polymer molecules, there are also some examples of investigations on large-area nanoarray created by molecules of Fe_3O_4 , Au, Si (Sun, Li, Zhang et al. 2008).

The parameters (the shape and the diameter) of derivative structures are strongly influenced by the related parameters of template. Up-to-date, most products of colloidal lithography exhibit spherical shape features. However, their fabrication desires high controllability, which in case of colloidal lithography is limited. Hence, the recent investigations have been aiming to enhance it. Simultaneously, other efforts have been focused on developing alternative techniques to fabricate nanostructures with non-spherical shape features such as non-spherical building blocks and multifaceted microsphere arrays. In particular, RIE, ion milling and annealing are intensively hired to fabricate nanoarrays of non-spherical shapes. For instance, Yang et al. (Choi et al. 2004) fabricated well-organized layers of non-spherical colloids by applying the anisotropic RIE to multi-layered PS colloidal crystals. They obtained a derivative structure with parameters depending on template features (the number of colloidal layers, the crystal orientation), and the RIE conditions.

Another approach based on the modified colloidal lithography was demonstrated by Goedel and his co-workers, who obtained the 2D array of nanocrescents by etching 2D PS colloidal crystals (partly embedded in polymeric coating) with hydrofluoric acid vapors (Xu and Goedel 2003; Marczewski and Goedel 2005).

Mentioned above RIE were intensively exploited by Yang and his collaborators to fabricate nanostructures with various morphology. In fact, they proved that precise control of experimental conditions allows

influencing the morphology of nanostructures. For instance, they obtained derivative structures of silica microspheres embedded in the polymer whose morphology varies from nanobowl arrays to nanoring arrays, depending on time of etching supported by RIE (Ren et al. 2009). The anisotropic RIE occurred suitable to fabricate another derivative structure with non-spherical features i.e. multifaceted microsphere arrays (Choi et al. 2006).

Considering the fabrication of MCC inverse replica described in section 5.3, there is worthy to mention about the impact of chemical etching on the colloidal lithography development. Chemical etching for the fabrication of silicon nanowire arrays with controlled diameter, length, and density was performed gradually by Zhu and his co-workers (Huang, Fang and Zhu 2007). First, the template was fabricated by self-assembly of PS spheres on the Si substrate. Their diameter was reduced by RIE, in fact the ncp structure was obtained from hcp structure. In the next step, a silver film was thermally evaporated onto the silicon substrate as a catalyst. Because the PS structure was used as a mask, this step resulted in hexagonal array of holes distributed in silver film, which was etched in a mixture of deionized water, HF, and H₂O₂. The silver catalyzed the silicon etching. After removing the PS spheres and the silver layer completely, the silicon material created two-dimensional array of nanowires. Its parameters (i.e. the diameter, height of individual nanowires, and distance between their neighboring centers) were easily controllable by changing the experimental conditions. This procedure can be applied to fabricate an array of tilted nanowire supported by Si (110) and Si (113) wafers instead of Si (100) wafers. (Peng et al. 2007) Although, the hcp arrangement of spheres is fundamental and privilege, there are some alternatives. Expect for non-close-packed colloidal crystals, other examples referred to binary colloidal crystals with two types of spheres differing from each other with diameters, and hcp structures with controllable defects.

Non-close-packed (ncp) colloidal crystals are important for application in optics, photonics, sensing, and surface patterning. There are fabricated by applying etching, template-directed assembly, or transfer printing to hexagonal close packed 2D colloidal crystals.

Etching is the most natural technique to obtain 2D ncp colloidal crystals from highly ordered 2D close-packed colloidal crystals by reducing the size of spheres without changing their positions (Zhang 2010). The reduction of diameter as well as distance between spheres can be

controlled by adjusting the time and the conditions to obtain the desired size of spheres. The well-controlled etching is enabled by isotropic plasma etching (Yan et al. 2006), the anisotropic reactive ion etching (RIE) (Tan et al. 2004) and the electron beam irradiation (Li et al. 2008). Anisotropic reactive ion etching enables the shape changes from spheres into oblate ellipsoids or oblate smooth spheres. In non-close-packed two-dimensional colloidal crystals, the morphology and photonic band-gap can be modified by etching because of decrease of interparticle photon coupling (Zhang 2010).

An alternative approach to fabricate ncp colloidal crystals is the template-directed assembly. This process runs with assistance of pattern silicon substrate with nanohole arrays, which is placed vertically in a slowly evaporating dispersion. Due to convective assembly, nanospheres from the evaporating dispersion will stay at the template surface, creating a 2D ncp array (Hoogenboom et al 2004). However, recent investigations (Jin et al. 2006) reported the application of slightly tapered nanopillar array as the template. Furthermore, Vancso et al. proposed the stimulation of spheres arrangement by the applied electrical field (Dziomkina, Hempenius and Vancso 2005). In their approach, the charged polymer nanospheres were deposited on topologically electrode substrate. The thin film of dielectric silica with patterned nanoholes was deposited on the ITO glass used as the electrode for electrophoresis of colloidal nanospheres. Turning on the electrical field induced moving the charged nanospheres toward opposite charged electrodes. In fact, they were deposited selectively into the nanoholes of patterned electrodes. The period and the lattice of their arrangement were determined basically by the pattern on the electrodes. Alternatively, a silicon wafer was tested as the patterned substrate, which was removed after the nanospheres had been arranged. In fact, the final product referred to a 2D ncp colloidal crystal on a flat substrate.

Transfer printing as a fabrication technique of ncp MCC was developed by Yan and his collaborators (Yan et al. 2005). In this method, they combined soft lithography with controlled deformation of PDMS to obtain ncp arrangement of silica spheres from close-packed silica colloidal crystals. First, a 2D colloidal crystal was fabricated by the self-assembly. Then, the arranged spheres were transferred onto the surface of PDMS stamp by using the lift-up technique. By stretching, or solvent swelling, the arrangement of silica spheres changed from close-packed into non-close-packed. Such ncp structure can be transferred onto a thin

polymer film. After calcination of polymer film, the ncp array of spheres could be again lifted up, deformed, and transferred by another PDMS stamp. By combining isotropic solvent swelling and anisotropic mechanical stretching, there is possible to obtain full-dimensional ncp colloidal crystal with all five 2D Bravais lattice, including hexagonal, oblique, rectangular, square, and centred rectangular lattices (Zhang 2010).

There are also other techniques to fabricate ncp MCCs. One of them is spin-coating, which was developed by Jing et al. They involved monomers of silica nanospheres and polymerized them on a flat surface (Jiang et al. 2006). By gradually increasing the spin speed, they obtained directly a ncp two-dimensional array of colloidal crystals embedded in thin polymer layer. By removing the polymer layer, waver-scale 2D colloidal crystals can be fabricated. However, this procedure can be modified by adding additional step of substitution of silica spheres by spheres of other materials. Moreover, investigations performed by Jiang et al. (Venkatesh, Jiang and Jiang 2007) show that there is possible to fabricate with this method two-components MCC structure with a complex pattern.

5.2.3 Polydimethylsiloxane (PDMS)

The other name used for calling polydimethylsiloxane is dimethicone or just the abbreviation, PDMS. It is a polymer commonly involved in fabrication and prototyping of microfluidic chips. It is classified as a mineral-organic polymer belonging to the siloxane family (“siloxane” is a derivative of “silicon”, “oxygen” and “alkane”), which contains carbon and silicon in its structure. It is non-toxic and environmental friendly. Hence, it is commonly exploited as a food additive (E900), in shampoos, and an anti-foaming agent in beverages or in lubricating oils.

Molecular features and related properties

The empirical formula of PDMS is $(C_2H_6OSi)_n$, where n is the number of monomers repetitions. The related fragmented formula takes the form of $CH_3(Si(CH_3)_2O)_n Si(CH_3)_3$. The number of monomers influences the state of non-crossed-linked PDMS, which is almost liquid for a low n , and semi solid for a high n . The structural formula of PDMS is shown in Fig. 5.3.c. Figures 5.3.a and 5.3.b refer to two components of the monomer.

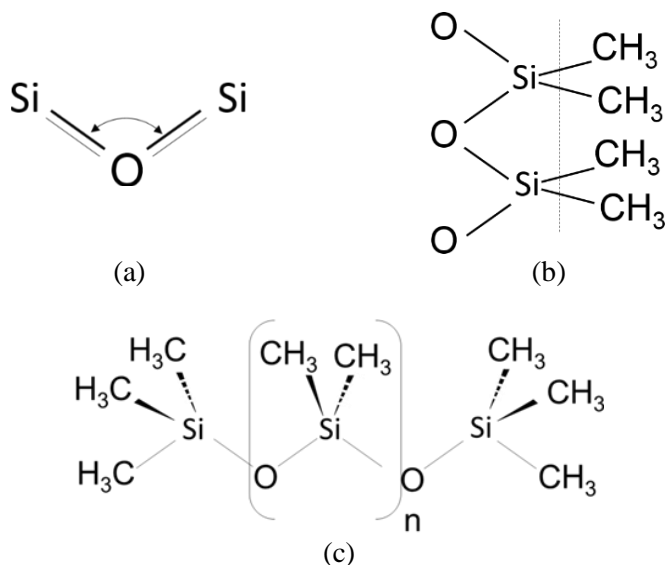


Figure 5.3. a) Polar inorganic backbone of the monomer (<http://www.dowcorning.com/content/discover/discoverchem/properties.aspx>), (b) nonpolar organic substituents and (c) structural formula of PDMS (<http://www.elseflow.com/microfluidic-tutorials/microfluidic-reviews-and-tutorials/the-poly-di-methyl-siloxane-pdms-and-microfluidics/>.)

The monomer possesses two major inclusions: non-polar organic substituents and polar inorganic backbone. Two types of bonds yield valuable properties for PDMS applications. In the polar inorganic backbone, long and strong Si – O bond supported by the wide bond angle, and a low barrier to rotation yield outstanding flexibility, internal mobility and a large free volume of PDMS. (<http://www.dowcorning.com/content/discover/discoverchem/properties.aspx>)

The other component, methyl group (- CH₃), is directly connected with the backbone by the shorter Si – C bond. It exhibits following features: weak intermolecular forces, opportunity to substitute other functional groups, easy to reorientation, no steric hindrance for the methyl group. Such molecular architecture of PDMS, with two types of bonds, the polar inorganic backbone and non-polar organic substituents, refers to an open molecular structure, which provides several benefits, such as:

- **strength and stability** are provided by the siloxane backbone exhibiting high bond energy (~ 445 kJ/mol), combined with the methyl (-CH₃) functional groups; strength and stability relate to

non-irritating properties of PDMS and to its resistance to temperature extremes, weathering, aging, oxidation, moisture, many chemicals, and UV radiation.

- **surface activity**, which corresponds to two capabilities of PDMS: film forming and wetting/ water repellence/ release; film forming is a natural consequence of higher critical surface tension of wetting (~ 24 mN/m) than the surface tension of PDMS, and make PDMS “greatly outperforming hydrocarbon in forming extremely thin (monomolecular) self-levelling films; wetting/ water repellence/ release relates to the low surface tension equal to 20.4 mN/m, what makes PDMS wetting most surfaces. Additionally, the arrangement of methyl groups yields capabilities to create water-repellent films, and good release properties.
- **rheological advantages** relate to all-temperature performance, easy spreading and flow; PDMS is very shear stable, due to very little internal friction; comparing with other hydrocarbon fluids with the same viscosity, PDMS spreads and flows more easily. The all-temperature performance relates to the low glass transition temperature, the high thermal stability, and less temperature-dependent viscosity. In fact, it saves its properties and features in the broad range of temperature (from below -40°C to 150°C);
- **breath-ability** is a common feature for all silicones, which exhibit highly permeable to oxygen, nitrogen, and water vapour (but not to water molecules). Hence, silicone elastomers create a water barrier to prevent its entrance, but release the internal moisture. This makes silicones suitable for applications as raincoats materials, and to prevent buildings from moisture inside. The singularity of PDMS polymers among other silicones refers to their high permeability to the diffusion of various substances, gases or active drugs, what makes them desired for healthcare applications.
- **high flexibility** is typical for all silicones. As they are easily deformable by stretching, compression, spreading and smashing, they recover the initial properties and volume after release as well. In fact, they are perfect materials to create

moulds and coatings, and for sealing expansion joints in buildings and bridges.

- **adaptability** is affected by the presence of groups other than the methyl group in the molecular chain of PDMS. It results in easily modified properties.

Valuable properties of PDMS and their applications

Commercially available polydimethylsiloxane (PDMS Sylgard®184, Dow Corning Corporation) is a mixture of two components: the base (pre-polymer) and the curing agent (cross-linker). The recommended mass ratio between them is 10:1, which is an optimal value applicable in microfluidic devices.

The key advantages of PDMS refer to its physical features, and fabrication benefits such as: low-cost due to no special conditions required, a capability for mass production, compatibility with MEMS fabrication techniques such as: micro-contact printing, replica moulding, micro-transfer moulding, micro-moulding in capillaries, and solvent-assisted micro-moulding (Xia and Whitesides 1998)

Table 5.1. lists eight categories of PDMS properties: optical, electrical, mechanical, thermal, inter-facial, permeability, reactivity, toxicity. The second column includes their short characteristic, and the third column refers to the benefits provided by them.

Table 5.1. Eight categories of PDMS properties and the benefits provided by them (McDonald and Whitesides 2002).

Property	Characteristic	Consequences
optical	transparent; UV cut-off, 240nm	optical detection from 240nm to 1100nm
electrical	insulating; breakdown voltage, 2×10^7 V/m	allows embedded circuits; intentional breakdown to open connections conforms to surfaces; allows actuation by reversible deformation
mechanical	Elastomeric; tuneable Young's modulus, typical value of 750 kPa	conforms to surfaces; allows actuation by reversible deformation; facilitates release from moulds

thermal	insulating; thermal conductivity, 0.2W/(m·K); coefficient of thermal expansion, 310µm/(m·°C)	can be used to insulate heated solutions; does not allow dissipation of resistive heating from electrophoretic separation
interfacial	low surface free energy ~20 erg/cm ²	replicas release easily from moulds; can be reversibly sealed to materials
permeability	impermeable to liquid water; permeable to gases and nonpolar organic solvents	contains aqueous solutions in channels; allows gas transport through the bulk material; incompatible with many organic solvents
reactivity	inert; can be oxidized by exposure to a plasma; Bu ₄ N ⁺ F ⁻ ((TBA)F)	non-reactive toward most reagents; surface can be etched; can be modified to be hydrophilic and also reactive toward silanes; etching with (TBA)F can alter topography of surfaces
toxicity	nontoxic	can be implanted in vivo; supports mammalian cell growth

With respect to the potential applications of PDMS in microfluidic devices, MEMS and bioMEMS, Mata with his collaborators tested its compatibility with various biomedical, microfabrications, and micromachining processes (Mata, Fleish and Roy 2005). The investigations have showed that the structural response and the surface properties depend on the design, fabrication and development of PDMS micro- and nanostructures. Although, the recommended ratio between the prepolymer and the curing agent is 10:1, they fabricated five samples with different amounts of cross-linker, i.e.: PDMS1 (5.7% of cross-linker), PDMS2 (10% of cross-linker, which corresponds to the recommended ratio), PDMS3 (14.3% of cross-linker), PDMS4 (21.4% of cross-linker), PDMS5 (42.9% of cross-linker). The tests referred to their sensitivity to spin coating, chemical immersion, oxygen plasma exposure, and culture media exposure. Increasing amount of cross-linker

in the sample induced the thickness decrease obtained at the spin-coating speed of 200rpm.

Immersion in buffered hydrofluoric and nitric acids resulted in little microtexture distortion. Potassium hydroxide, sulphuric, and hydrofluoric acids resulted in total damage of micro-textures. However, chemical immersion didn't affect the PDMS surface hydrophilic significantly.

Oxygen plasma exposure increased the surface hydrophilicity of PDMS2. Its hydrophobic properties were recovered after its exposure to the air.

In general, the sterilization did not influence the PDMS surface micro-textures, element concentration, or hydrophilicity. Only UV sterilization increase the contact angle of PDMS2 from 113.5° to 119.0°

Ethanol, and UV treatment did not affect changes in mechanical properties, whereas autoclave sterilization affects the storage modulus and the ultimate tensile stress, which values were influenced by the composition of PDMS, e.g. for PDMS1 the ultimate tensile stress was equal to 3.9 MPa, whereas for PDMS3 its values amounted 10.8 MPa.

The investigations have shown that the sample with recommended ratio (PDMS2) is resistant to the most of used chemicals, and behaved similarly to the other samples.

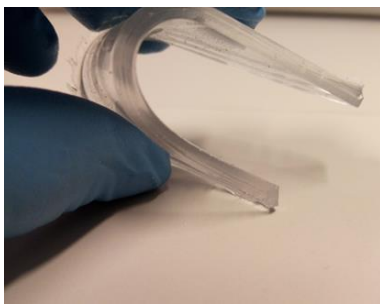
The highest tensile strength and the storage modulus referred to PDMS3. It showed that the mechanical properties of PDMS can be altered without an influence surface chemistry, but only by changing the amount of cross-linker.

There are several papers that describe various technique to tune properties of PDMS. For instance, Xu *et.al* increased the static friction between PDMS and embedded silica nanowires by ultraviolet/ozone treatment (Xu et al. 2011). However, more appealing issue seems to be methods to tune the value of Young modulus. Its typical value is given it Table 5.1. However, the recent investigations have shown that the value of Young modulus varies depending on techniques involved for PDMS fabrication (Thangawng *et al* 2007) (Wong 2010) (Balaban 2001).

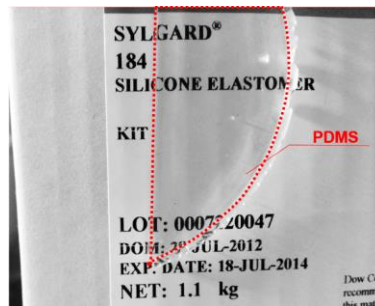
Easily tunable mechanical properties of PDMS are not the only advantages intensively exploited in medicine, microfluidic devices or bioMEMS/MEMS. Also, the transparency (Fig.5.4a) and flexibility (Fig.5.4b) are valuable especially for medical applications such as:

- microlens/microlens arrays (Shih et al. 2006);

- oxygenate membranes (durable);
- shunts (non-toxic);
- prosthesis;
- breast implants;
- joints;
- tracheal reconstruction;
- bladder reconstruction;
- maxillofacial reconstruction;
- heart pacemaker leads;
- heart valves;
- burn dressings;
- catheters;
- drainage tubing material;



(a)



(b)

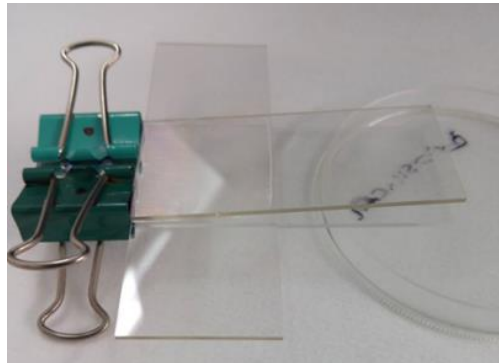
Figure 5.4. The PDMS features observed during the investigations (chapters 6 – 8): a) high flexibility; b) high transparency (the dotted line depicts the contour of PDMS layer; behind the sample there is a box with PDMS components used in the fabrication).

5.3 Process

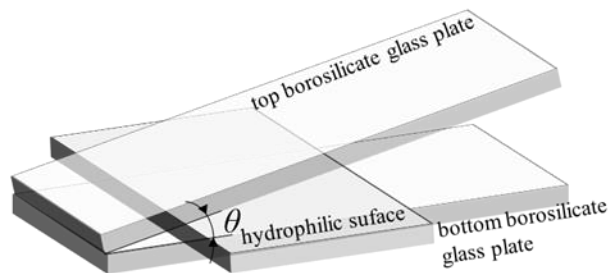
The fabrication was started by preparing the equipment. The bottle of water suspension of PS spheres ($D = 1.6\mu\text{m}$ or $D = 1\mu\text{m}$) was placed in the ultrasonic bath, where water motion stimulated by ultrasounds, split the PS spheres stack to each other. At the same time, two borosilicate glass slices were treated with UV inside the UV ozone cleaner to improve their wet-ability. Both processes took about 45 min. Further, the bottle and the borosilicate glass slices were taken to the clean room,

where the experimental set-up was mounted with respect to the procedure proposed in (Sun et al. 2010). The set-up (Fig.5.6a, b) was composed of two external glass slices supporting the wedge shape. The angle between them was equal to 2° . The internal side of top slice was prepared previously in the ozone cleaner. The second slice prepared simultaneously in the UV ozone cleaner was placed inside the configuration, transversally to the bottom glass slice. The top layer of this slice was a support for the convective self-assembly of the PS spheres. The suspension was injected between the top slice and the internal slice. The setup was left in the clean room at the temperature about 20°C for 24h. After this time, the water evaporated completely remaining a white, rectangular mould parallel to the common edge (Fig.5.5c). The mould was a monolayer colloidal crystal with PS spheres arranged into hcp array.

a)



b)



c)

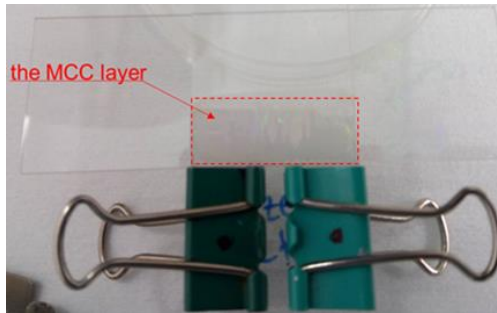


Figure 5.5. The wedge-shaped configuration: a) the real look, b) the scheme, c) the top view on the sample of MCC (the dotted line).

In the next step, the sample was used as a template for PDMS deposition. PDMS was produced with respect to the producer's recommendation i.e. two components (the base and the curing agent) were mixed together in the mass ratio 10:1. The desired mass of the PDMS to cover the sample completely was 10g. After 3 min of intensive mixing, the elastomer mixture was left for 90 min to release the air bubbles. Meanwhile, the MCC template was placed in the Petrie dish with chlorotrimethylsilane for 90 min to silanize the glass surface (Fig.5.6 a). Generally, the silanization supports the increasing hydrophobicity of glass surface. In the fabrication, the silanization allowed to remove easily the dried PDMS from the glass slice.

After 90 minutes, the PDMS was dropped onto the template. The template with the PDMS top layer was transferred into the oven with the temperature 65°C for 8h. After this time, PDMS layer was dragged out from the glass surface. In fact, the hexagonal array of PS spheres was moved into the PDMS layer. The template embedded in the PDMS matrix is called PDMS replica of MCC. The inverse replica was obtained by etching the replica with dimethylformamide (DMF) over 60 min. The top edge of sample was hold by the paper clips so that the sample was dipped vertically in dimethylformamide (Fig.5.6b).

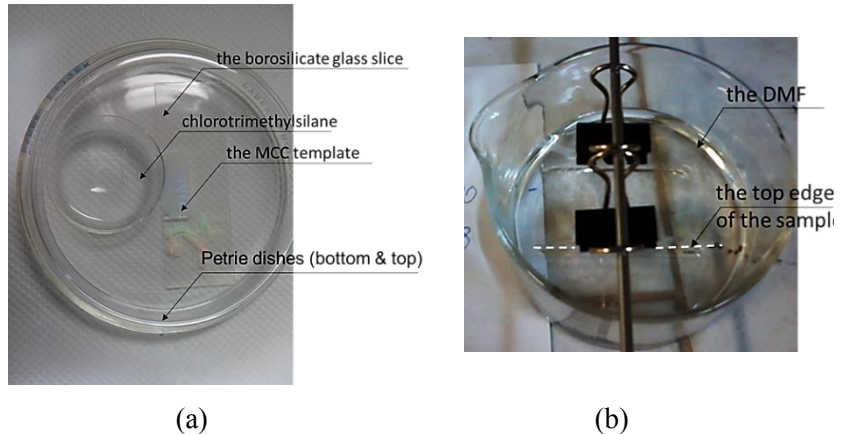


Figure 5.6. a) Silanization of borosilicate glass slice with MCC template; b) the sample etching in DMF.

Figure 5.7 shows the scheme of entire fabrication. The fabrication can be divided into three steps. Each of them refers to other product i.e. the first step involved wedge-shape approach to obtain the monolayer colloidal crystal. In the next step, the MCC was used as a template for PDMS deposition. Further, the PDMS was removed with the embedded array of PS spheres. This step resulted in the PDMS replica of MCC. Finally, by etching the PDMS replica of MCC in DMF, the inverse replica of MCC in PDMS was produced.

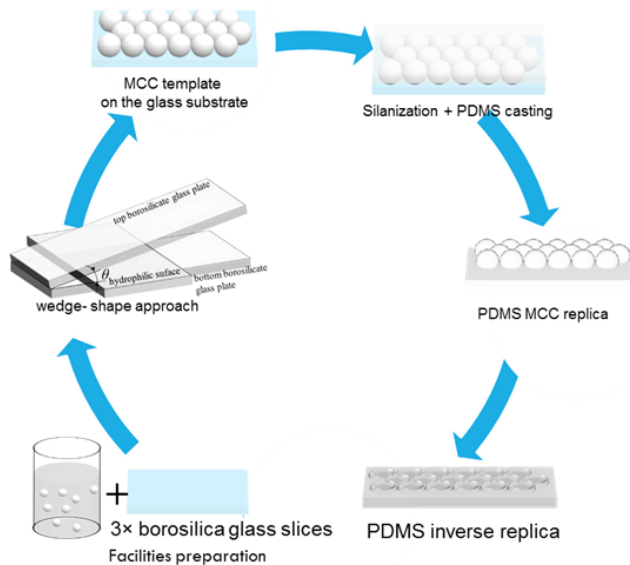


Figure 5.7. Schematic representation of the MCC inverse replica fabrication.

5.4 Results

The fabricated sample is a slice of PDMS with multicolour blazing pattern at the top surface illuminated by polychromatic light (Fig. 5.8 a). The volume parameters of sample and the size of blazing layer are given in Fig. 5.8 b.

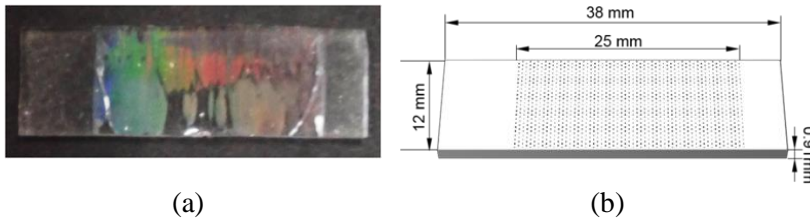


Figure 5.8. a) The view of sample top surface with multicolour blazed effect, b) The volume parameters of sample.

The blazing effect refers to the inverse replica of MCC. Its fabrication involved two types of template. The first one was composed of PS spheres with the diameter equal to $1,6 \mu\text{m}$. The second type of template included the spheres with the diameter equal to $1 \mu\text{m}$.

Before measurements, the structural characteristics was performed by the atomic force microscope (AFM) and the scanning electron microscope (SEM).

The AFM analysis was performed for the sample fabricated with the template diameter of $1.6 \mu\text{m}$. It provided the three-dimensional visualization of sample (Fig.5.9 a), the top image of sample surface (Fig.5.6 b), and the sample profile with depicted measurements of depth of grooves, and of the distance between the centres of adjacent grooves (the pitch).

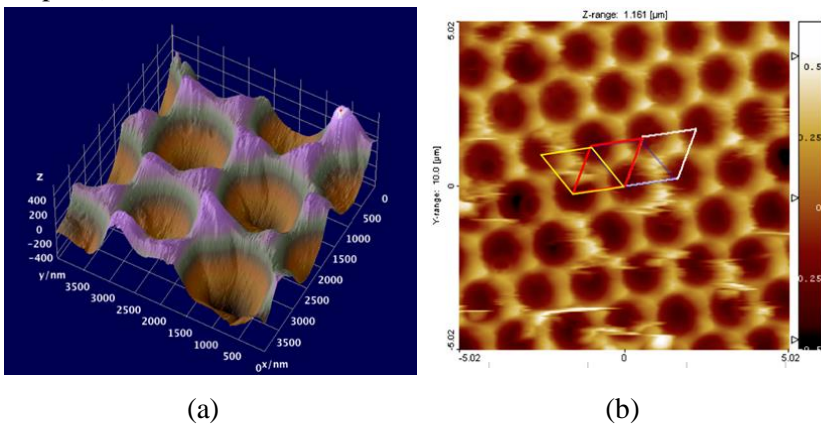


Figure 5.9. a) Three-dimensional visualization of sample,

performed by the AFM; b) The top view of sample surface.

Based on the data, the average values of depth of grooves, and the pitch were calculated. They were equal to (434 ± 71) nm and (1625 ± 110) nm, respectively.

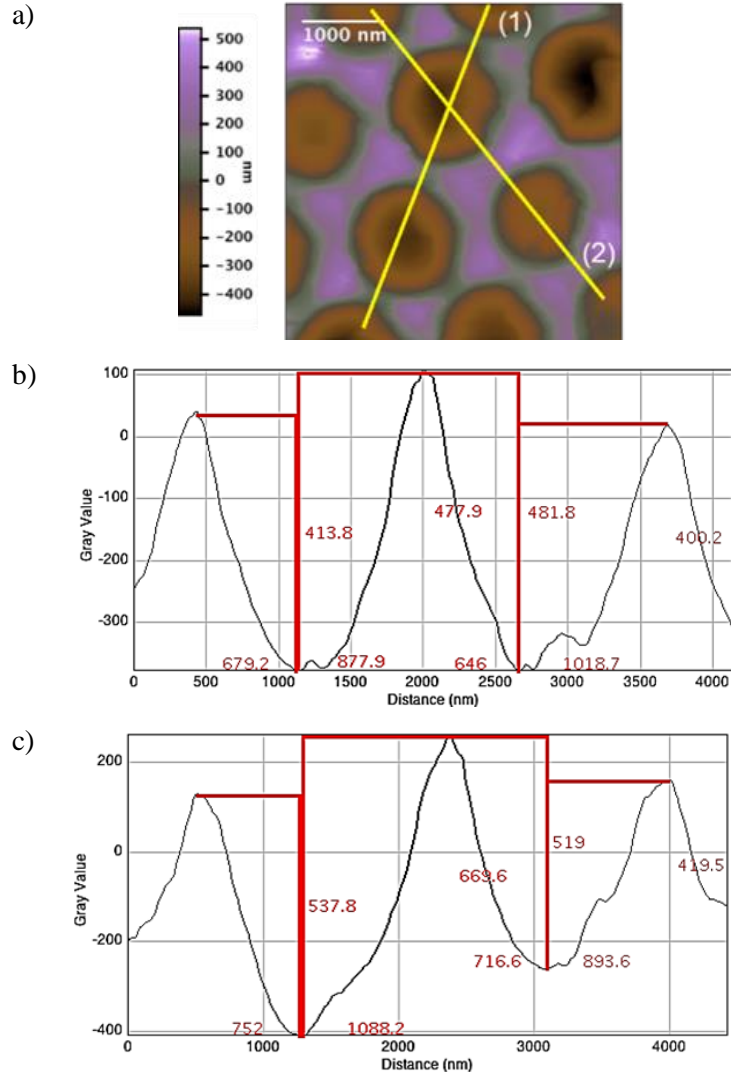


Figure 5.10. a) Top view of the sample top surface; b), c) the profiles of grooves corresponding with lines (1) and (2), with the depicted details about depth and pitch.

The SEM images were taken for the sample whose fabrication was supported by the template with the spheres diameter equal to $1\mu\text{m}$. The top view image (Fig.5.11 a) confirms the hcp arrangement of holes at the sample surface. Unlike AFM images, the SEM images refer to larger sample areas. Hence, they registered discontinuities and dislocations in the hcp arrangement of holes, which are typical for products of self-assemble fabrication (Ng, Koh and Wong 2012).

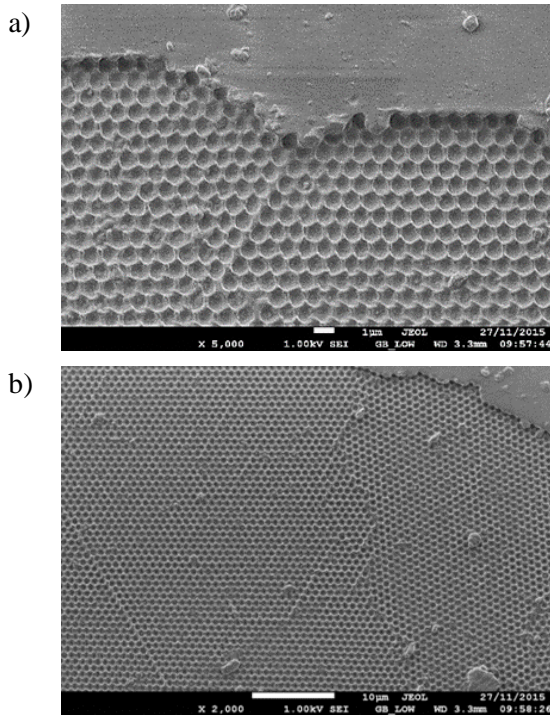


Figure 5.11. SEM images of a) top surface of surface with hcp arrangement of holes; b) dislocations/discontinuities at the sample surface, resulted from the self-assemble fabrication.

Further investigations involved an optical approach, and referred to interaction between the sample and an incident light.

The first experimental setup (Fig.5.9 a) was mounted to illuminate the top surface of sample. The incident light induced two beams propagating immediately under the top surface. The angle between them was tunable by switching the wavelength of incident beam from 400 nm to 700nm (Fig. 5.9 c)

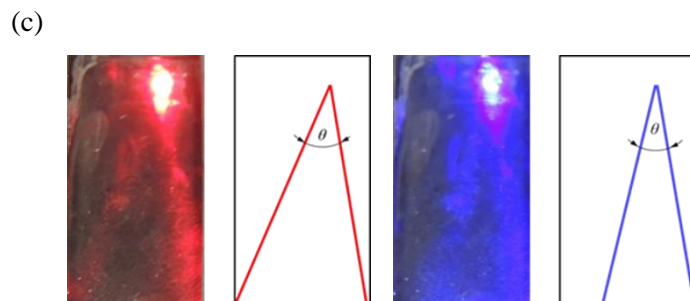
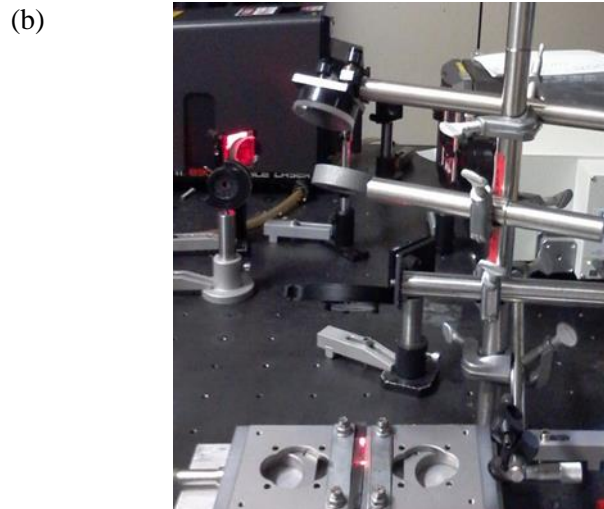
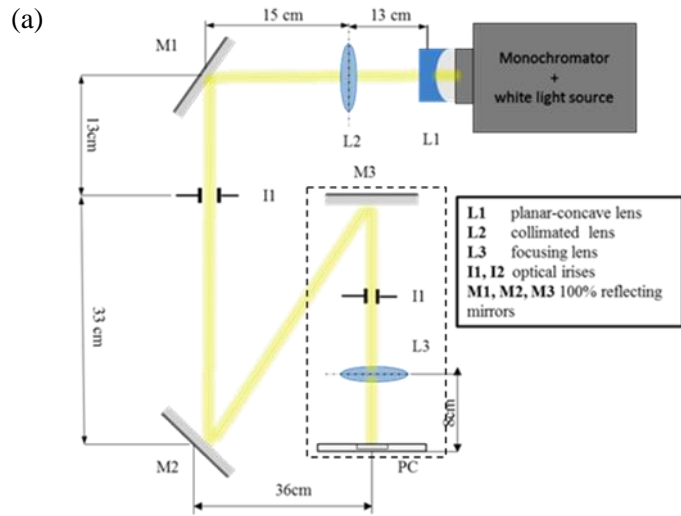


Figure 5.12. a) The experimental set-up to illuminate the sample top surface, the dashed line selects the part of set-up shown in the image b); c) two beams induced by

incident beam with different wavelength ($\lambda = 470\text{nm}$ and $\lambda = 630\text{nm}$) inside the structure; different wavelengths correspond to different angle between the propagating beams i.e. $\theta = 32^\circ$ for the red light, and $\theta = 23^\circ$ for the blue light.

The next experiment involved the laser diode to illuminate the sample with the monochromatic, coherent light with the wavelength 405nm . Initially, the light was polarized vertically. The detailed arrangement of optical elements in the experimental set-up is shown in Fig.5.13b (Fig.5.13 a. presents the real view of experimental set-up).

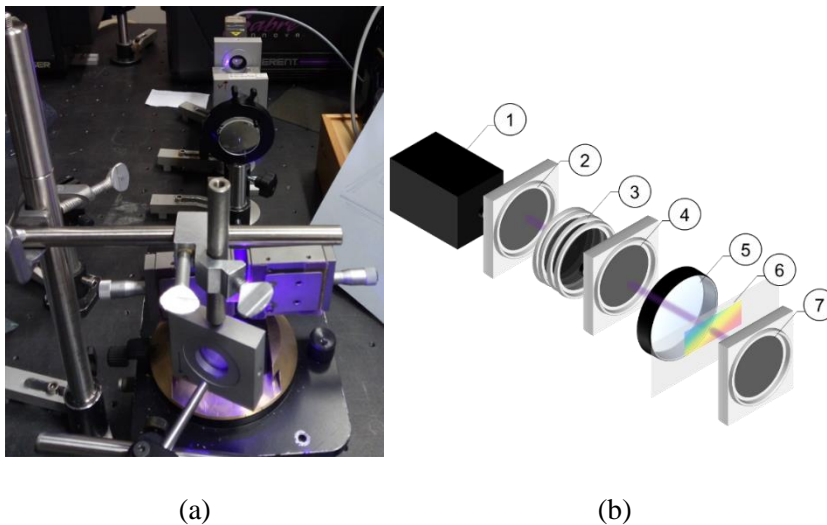


Figure 5.13. The experimental setup a) in reality and b) its scheme, the numbers refer to the optical elements as follow: 1 – laser diode, 2 – depolarizer, 3 – set of filters, 4 – polarizer (V/H), 5 -focusing lens, 6 – sample, 7 – polarizer (V/H);

The observable with the naked eye results were projected onto the screen set after the sample. For two-dimensional array of circular holes arranged into a hexagonal lattice, the diffraction pattern is composed of six 1st order diffraction spots crating the hexagonal shape around the central spot (the 0th order spot). Any structural changes indicate mechanically result in changes of brightness and shape in the diffraction pattern.

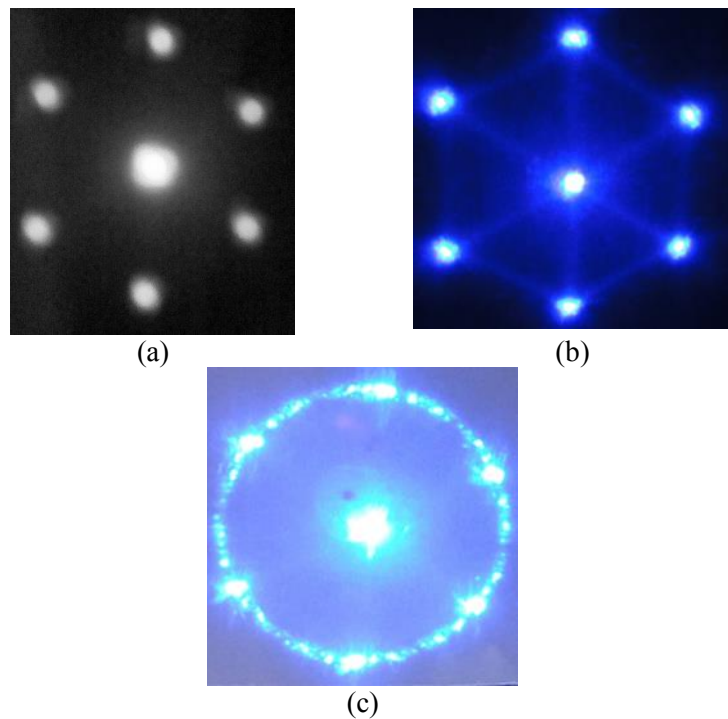


Figure 5.14. Three different diffraction patterns provided by the sample illuminated at three different points of structure.

Figure 5.14 (a-c) shows the diffraction images (the diffraction patterns) provided by the same sample, but illuminated at three different point of its structure. Following the analysis performed in (Tan and Chen 2012), the differences between the images can be related to the hexagonal arrangement of holes. Hence, the Fig. 5.14a refers to the perfectly arranged holes into hexagonal lattice, without defects, dislocations, or any other structural imperfections. Figure 5.14 b is a combination of ideal diffraction pattern containing six spots, and the bright lines between them. These lines are resulted from interference between light coming from aligned holes. Figure 5.14 c refers to the most disordered structure. The visible bright ring around the central spot refer to *ghost diffraction* (Tan and Chen 2012), which is a combination of ghost fringes and regular hexagram pattern (the hexagonal set of six spots around the central one) provided by an array without imperfections.

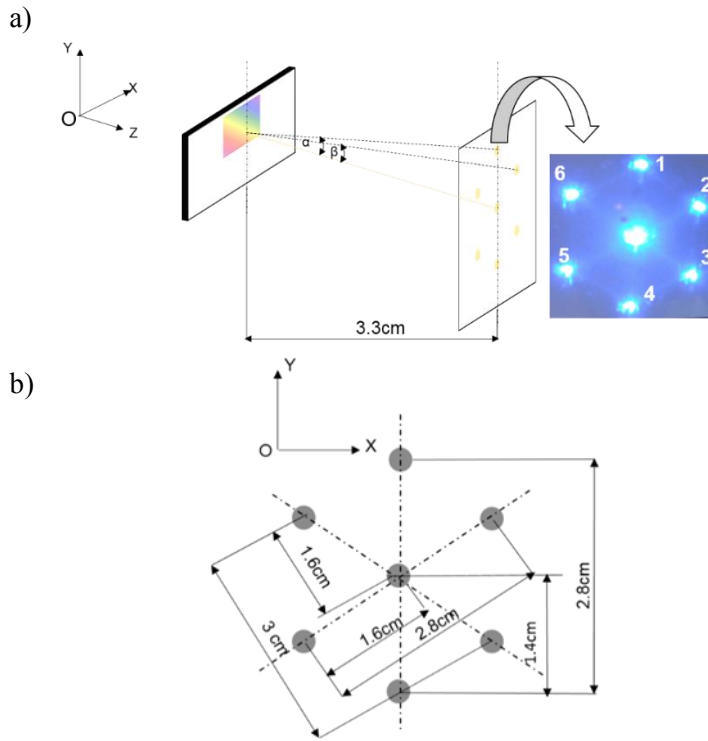


Figure 5.15. (a)The screen-sample arrangement in the experimental set-up (d_{ss} is the distance between the screen and the sample equal to 3.3cm), and the real view of diffraction pattern (the numbers 1 – 6 refer to the diffraction spots, and d_{0-i} terms the distance between each 1st order spot and the central spot), β_i is diffraction angle corresponding to each spot (b) the scheme of diffraction pattern with the depicted distance from the central spot to each 1st order spot;

Figure 5.15 a shows the screen – sample arrangement and the real view of diffraction pattern. Figure 5.15 b presents the scheme of diffraction pattern with depicted distance measured between the centres of central spot and each 1st order spot on the projection of (Fig.5.12 a) diffraction pattern.

Knowing the distance between the screen and the sample, measured from the screen surface to the central spot on the parallel screen (Fig.5.12 c), possibility to determine the diffraction angle, β_i

($i = 1,2,3,4,5,6$) for each diffracted beam relating to one of six 1st order spots, as follow:

$$\tan \beta_1 = \frac{d_{0-1}}{d_{ss}} = 0.42 \rightarrow \beta_1 = 23^\circ \quad (5.1)$$

$$\tan \beta_2 = 0.36 \rightarrow \beta_2 = 20^\circ \quad (5.2)$$

$$\tan \beta_3 = 0.42 \rightarrow \beta_3 = 23^\circ \quad (5.3)$$

$$\tan \beta_4 = 0.42 \rightarrow \beta_4 = 23^\circ \quad (5.4)$$

$$\tan \beta_5 = 0.48 \rightarrow \beta_5 = 26^\circ \quad (5.5)$$

$$\tan \beta_6 = 0.48 \rightarrow \beta_6 = 26^\circ \quad (5.6)$$

However, assuming the ideal hcp arrangement of voids in the sample, the diffraction pattern should exhibit the symmetrical, hexagonal shape. Therefore, the distance from the central spot for each 1st order spot should be the same, and the diffraction angles (eq. 5.1. – 5.6) should be equal. Hence, there is reasonable to compute their average value which is equal to $\beta_{ave} = (23 \pm 2)^\circ$.

Concluding, the AFM images and SEM images confirmed the hcp structure of sample. The top images present the array of circular holes arranged at the common lines that correspond to the diagonal lines in the diffraction pattern. Furthermore, because the SEM images were taken for larger sample areas than the AFM images, they registered also the imperfections typical for self-assembly products, such as: discontinuities/ dislocations, veins (Fig.5.8).

On the other hand, the AFM images emphasis the strongly non-uniform profile of grooves in the PDMS matrix. The non-uniformity of structure was also confirmed experimentally. The diffraction pattern resulted from the interaction between the monochromatic coherent light ($\lambda = 405\text{nm}$) transmitted through the structure varied for different points of light illumination. If the illuminated area exhibits ideal, non-defective arrangement of circular holes, the diffraction pattern refers to the hexagonal arrangement of six spots with three diagonals. The visible diagonals are a result of light interference between identical circular holes at the common line that can relates to the veins, or discontinuities. In case of more serious imperfections e.g. non-regular period or not aligned holes, the diffraction pattern is a combination of ideal hexagonal

pattern and ghost diffraction fringes that create a ring around the central spot (Fig.5.11c).

Above observations refer to the diffractive properties of sample. However, the observations of two beams induced by illuminating the sample top surface with the monochromatic light (Fig.5.12) are also noteworthy with respect to its similarity to the effect described by Tandon et al. (Tandon et al. 2005; Luo et al. 2004). The described phenomenon was termed as the super-prism effect and related to two beams propagating in a periodic structure of photonic crystal slab. The common angle between them was tuneable by switching the illuminated wavelength at the certain angle between them. Nevertheless, in our case, this approach requires measurements repeated at well-defined conditions relating to:

- the polarization of illuminated beam;
- the incident angle at the top surface of sample;
- the thickness of periodic structure.

Chapter 6

Strain sensitivity assessed by analysing the light spectrum of diffracted incoherent light transmitted by the sample

7.1 Introduction

As described in the previous chapter, the fabricated samples exhibit a periodic structure with semivooids hexagonally arranged. The AFM and the SEM images confirmed the presence of long order semispherical shape voids and allowed determining their structural features. Some differences in their profiles and depth due to the polydispersity of the spheres used as well as to the presence of punctual defects and dislocation are also present.

Initially, the interaction of an incoherent light (white light) with the structure produces a hexagonal diffraction pattern, indicating that the sample acts as diffraction grating.

Furthermore, the two-dimensional distribution of the semivooids permits to classify the structure as a biperiodic diffraction grating.

Many papers have performed theoretical studies on optical properties of diffraction gratings (Gaylord and Moharam 1985; Moharam, Grann and Pommet 1995; Antonakakis et al. 2012). Usually, they report on the interaction between an incident light and the periodic structures, and disregard the formalism of Maxwell's equations, which adopts the electromagnetic theory of light. Additionally, the papers describe the theoretical behaviour applying numerical approaches. An example is the paper of Tamulevičius et al., which assess a complete study involving theoretical considerations experimentally validated (Tamulevičius et al. 2013).

In this chapter are reported the experimental conditions applied to investigate the optical response of the grating under a uniaxial strain and to determine its sensitivity.

First of all, the diffraction patterns have been obtained in transmission mode, with an incoherent light passing through the sample. Due to the hexagonal arrangement of the semivooids the diffraction pattern is constituted by six spots surrounding a central one (zero order). Each of them refers to one of three symmetrical axes of hexagonal unit cell.

From a mathematical point of view, the main equation that describes the optical response of the diffraction grating as a function of its structural properties is eq. (6.1)

that correlates the dimension of the pitch (d) and the diffracted wavelength (λ):

$$d \cdot (\sin\alpha + \sin\beta_m) = m\lambda \quad (6.1)$$

Here, d is the pitch (the distance between neighbouring grooves), α is the incident angle, β_m the diffracted angle of m order beam and λ is a diffracted wavelength. Now the application of an external stimulus (uniaxial strain) produces a variation in the optical response due to a modification of the structural and morphological features of the grating. This allows determining the sensitivity of the 2D structure.

In our case the variation in the optical response can be revealed investigating the change in the diffracted wavelength of the 1st order spots as a function of the applied strain.

Experimentally the variation was monitored using a fibre connected to a silicon CCD detector (fiber-detector) as sketched in Figure 6.1 b

Initially (for non-elongated sample) the position of the fiber has been set to a specific angle in order to collect only green light (the centre of visible light range).

As evidenced and sketched in Fig.6.1 b, the angle position of fiber-detector has to be chosen carefully; due to the fact that the wavelength of the diffracted light, as reported by the equation 6.1, depends on the incident angle and detection one.

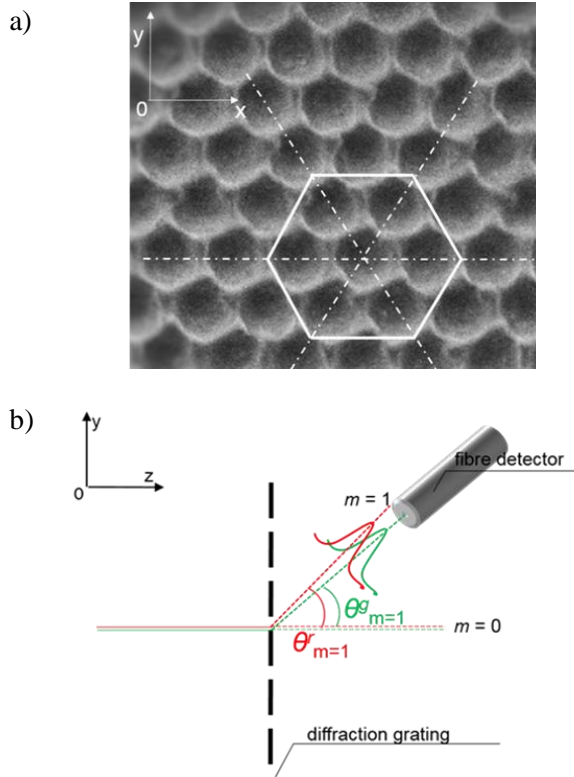


Figure 6.1. a) The hexagonal arrangement of semiovoid holes in the sample: the hexagonal unit cell (depicted by the continues, white line), the symmetrical axis (the white, dashed lines), b) the alignment of the fibre detector with respect to the propagation direction of diffracted beam; β_g and β_m are the diffraction angles of green and red light, respectively.

In order to remove one grade of freedom, the incident light was impinging on the surface of the grating with a theta equal to 0° , in this condition, the equation 6.1 can be written as follow:

$$d \cdot \sin\beta_m = \lambda \quad (6.2a)$$

$$\sin\beta_{m=1} = \frac{\lambda}{d} \quad (6.2b)$$

Equation 6.2 b shows the relation between the pitch, the diffracted angle and the diffracted wavelength; hence, the application of an axial stress produces a variation in the pitch dimension inducing a variation in the diffracted wavelength (m order). In this case monitoring the wavelength

diffracted as a function of the applied strain the sensitivity of the system can be determined.

7.2 Experimental set up and acquisition program

Initially, a dedicated experimental set up has been implemented and an acquisition program that allows selecting the excitation wavelength and acquiring the intensity of the diffraction wavelength has been developed. The entire experimental set up is reported in Figure 6.2 where the main elements are the following:

- Xe lamp + monochromator (FL 1039/40 +FL 1039-1409-0614, HORIBA JOBIN YVON, EDISON);
- optical elements such as plano-convex lens, collimated lens, focusing (positive) lens, iris diaphragm to control the “propagation” of the light;
- linear stage to stretch the sample along the OX axis

As excitation source a Xe lamp was used, where a specific wavelength can be selected by means of a monochromator. The selection of the wavelength was controlled by a dedicated program developed in LabVIEW, whose typical main “screen” is shown in Figure 6.5, where different options can be selected:

- selecting the illuminating wavelength;
- switching the illuminating wavelength automatically;
- setting the time step, the wavelength step;
- data acquisition

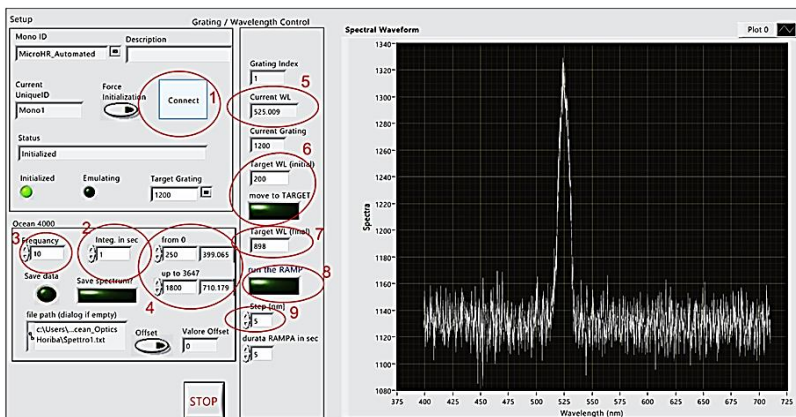


Figure 6.2. Main screen of the program developed in LabVIEW to select the excitation wavelength and collect the data.

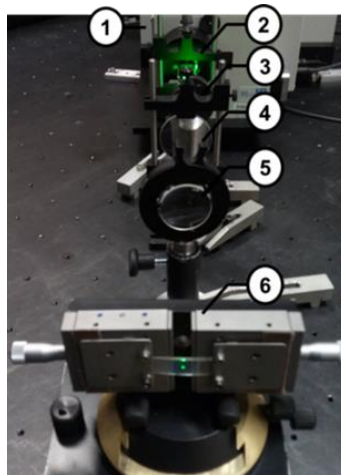
After the wavelength selection, the light beam presented a spherical wavefront. To maintain intensity and provide uniform illumination to the sample, the spherical wavefront was transformed into planar beam by a plano-concave lens assisted by the collimated one.

Finally, the light has been focused by the positive lens on the sample. The interaction of the beam with the sample produced a diffraction pattern as reported in Figure 6.4 a

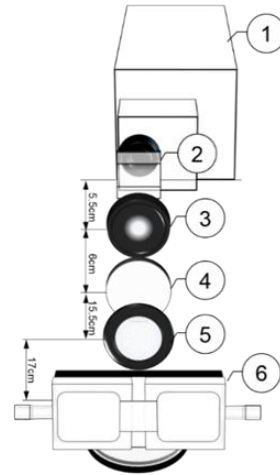
The application of an axial stress was obtained fixing the sample on a linear stage as shown in Fig.6.3 a, equipped with two micrometers, that produce a longitudinal elongation of the sample (see Fig 6.3 c).

After the wavelength selection, the light beam presented a spherical wavefront. whose intensity decreased during propagation. To maintain intensity and provide uniform illumination to the sample, the spherical wavefront was transformed into planar beam by the a plano-concave lens assisted by the collimated one. Finally, the light has been focused by the positive lens on the sample. The interaction of the beam with the sample produced a diffraction pattern as reported in Figure 6.3 a.

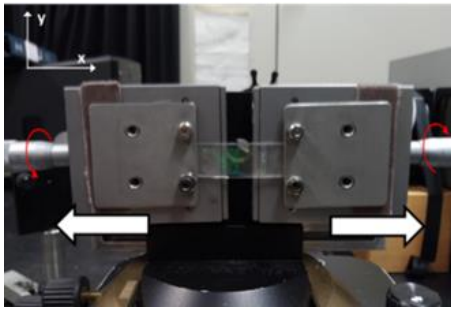
The application of an axial stress was obtained fixing the sample on a linear stage as shown in Fig.6.1 c, equipped with two micrometers that produce a longitudinal elongation of the sample (see Fig 6.2 c).



(a)



(b)

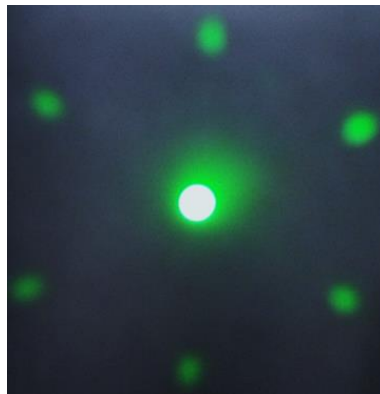


(c)

Figure 6.3. Measurements set-up: a) photograph, b) scheme; the numbers refer to the components as follow: **1** – Xe lamp + monochromator; **2** – plano – convex lens; **3** – diaphragm; **4** – collimated lens; **5** – focusing (positive) lens, **6** –stage for the sample linear elongation; c) The white arrows show the direction of sample’s elongation.

The diffraction image (the diffraction pattern) can be easily observed by the naked eye as shown in Figure 6.4 a. It contains six spots of the 1st order, arranged hexagonally around the 0-order spot (the central spot). To acquire the intensity of the diffracted wavelength the screen was replaced by the fibre-detector that collected the optical response from each spot, for each elongation step performed every 200 μm Fig.6.4 b illustrates the measurements conditions applied for the acquisition of the 1st order spots signal.

(a)



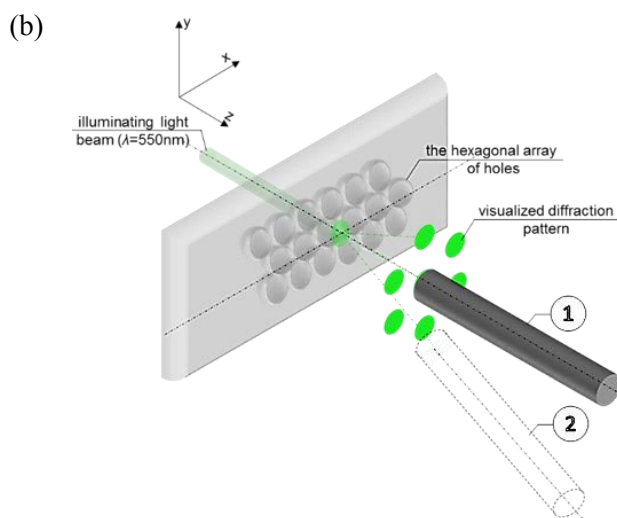


Figure 6.4. a) Diffraction pattern provided by the incoherent light impinging on the sample where the 1st order of diffraction spots is observable; b) positioning of fibre detector on different spots.

7.3 Results and discussion

As described in the introduction, the optical response of the structure was investigated analysing the changes in the diffracted wavelength of the 1st order spots as a function of the applied strain. The measurements were performed in the elongation range between 0 - 1000 μm . For the elongation of 1000 μm , a change visible by naked eyes as shown in Figure 6.5 is evident.

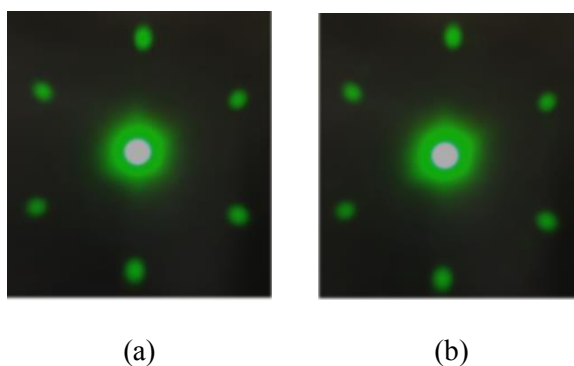
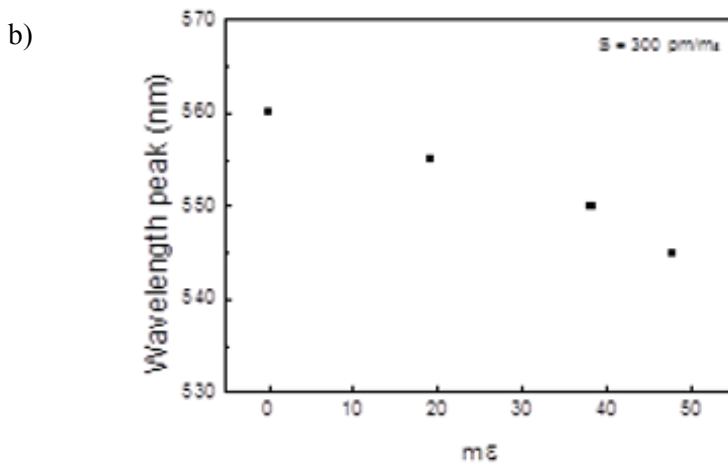
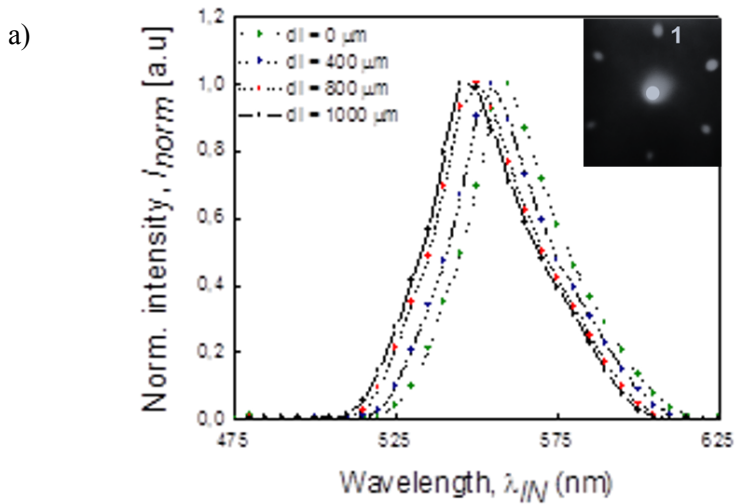


Figure 6.5. Diffraction patterns obtained using $\lambda = 555 \text{ nm}$

as excitation source a) unstretched sample, b) sample elongated at $\Delta l = 1000 \mu\text{m}$.

Using the approach described in the experimental section the signal from the 1st order diffraction spots for several elongation steps of $200 \mu\text{m}$ has been collected and depicted in Fig.6.6. Spots number 1 and 3 have been reported as example.



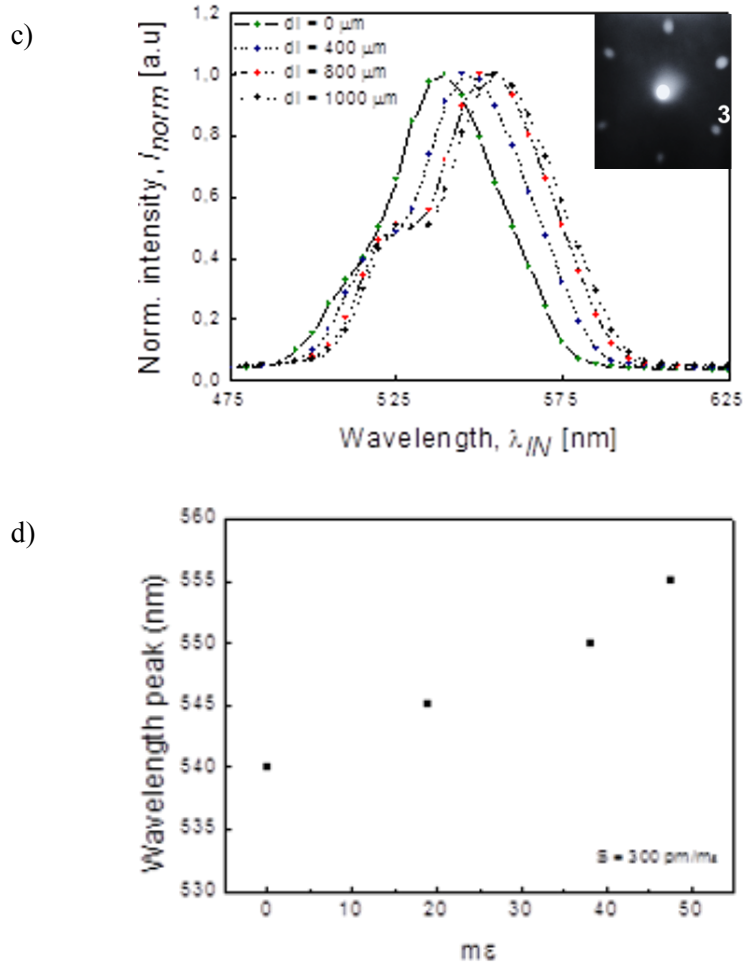


Figure 6.6: Relationship between the peak positions and elongation of the silicone grating (from initial 0 to 1 mm) owing to stretching. a) normalized reflectance spectra (top spot 1 and bottom spot 3), b): peak wavelength position as a function of $m\epsilon$ (top spot 1 and bottom spot 3)

Analysing Fig. 6.6. we can clearly notice two opposite linear behaviours: a blue shift for spot number 1 and a red shift for spot number 3 associated to a modification of the diffraction grating pitch. In fact, the diffracted peak wavelength decreases from 560 nm to 545 nm for spot number 1 and increases from 540 nm to 554 nm for spot number 3 for a strain at about 47 $m\epsilon$. Moreover, from the data reported in Figure 6.6.b a sensitivity of the sensor of about 300 pm/ $m\epsilon$ has been determined for

both the spots. This result is comparable with other mechanochromic sensors reported in the literature.

7.4 Conclusions

In this chapter the approach developed in order to assess the sensitivity of the grating has been described. In the specific the application of an axial strain, modifies the pitch of the semivooids as well as their shape. Analysing the diffraction patterns acquired, as a function of the applied strain, we have noticed that the distance of the spots in position 1 and 6 increases respect to the position of the zero order, while the distances position of the spots 2,3,4,5 decrease. This effect can be associated to the modification of the shape of the semivooids. In fact, an elliptical shape of the voids has been observed. The elliptical shape produces a variation in the pitch in two directions (X-Y). In X direction, parallel to the applied strain, we have an increase of the pitch of the grating while in the direction perpendicular we have decreasing of the pitch. These considerations are in agreement with the experimental spectra acquired where a red shift has been observed for example from spot number 3, while for the spot number 1 a blue shift is evident. Moreover, a linear trend of the wavelength shift is observed with a sensitivity of the sensor is of about 300 pm/m determined for both the spots. This result is comparable with other mechanochromic sensors reported in the literature (see the review of Chan et al. (2013)).

Chapter 7

Estimation of the strain based on transmission measurements: changes in shape of diffraction pattern and in the polarization of the diffracted light

7.1 Introduction

In this chapter, two approaches to assess the strain sensitivity are applied and discussed. Both of them involved data provided by the diffraction pattern. In the first one, the diffraction pattern was projected on a screen and registered by a CCTV camera. It was created by light transmitted through the sample, and diffracted by the periodic structure at the top surface of the sample. In a second step, the images taken by the camera were used to measure the distance between spots at the same diagonal, and to assess the intensity of diffracted light. However, first, the images should be proceeded to remove the background, which provides additional error to calculations, and is due to the following effects:

- interaction between the screen and the diffracted light;
- light scattering at the surface of other components in the experimental setup.

Both effects depend on the methodology applied to acquire the measurements and the noise provided by them can be removed by digital filtration in Matlab or any other software for image processing.

This approach is usually employed after accurate selection of the experimental conditions (i.e. choice of the optical filters) The final result corresponds to a uniform black background, whose brightness (the intensity per surface unit) is equal to 0 in the greyscale (scale range values from 0 to 255).

The different steps of the experiments are summarized as follows:

- background removing;
- estimating the centroid (X, Y -coordinations of the geometrical centre of spot) of each 1st order diffraction spot.

- estimating the distance between two spots at the same diagonal;
- assessing the mean value of light intensity coming from each 1st order spot.

In this chapter, two approaches to assess the strain sensitivity are demonstrated. Both of them involved data provided by the diffraction pattern. The diffraction pattern was projected onto the screen and registered by the CCTV camera. It was created by light transmitted through the sample, and diffracted by the periodic structure at the top surface of sample (the two – dimensional diffraction grating). In the next step, the images taken by CCTV camera were used to measure the distance between spots at the same diagonal, and to assess the intensity of diffracted light. However, first, the images should be proceeded to remove the background impact, which provides additional error to calculations. The background impact refers to the speckles (white single points on the dark background) which are assumed as noises, and relate to the following effects:

- interaction between the screen and the diffracted light;
- light scattering at the surface of other components in the experimental setup.

Both effects are results of applied methodology for measurements. Hence, they are not avoidable. However, the noises provided by them can be removed by digital filtration in Matlab or any other software for image processing.

This approach is usually employed after accurate selection of the experimental conditions (i.e. choice of the optical filters) The final result corresponds to a uniform black background, whose brightness (the intensity per surface unit) is equal to 0 in the greyscale (scale range values from 0 to 255).

The different steps of the experiments are summarized as follows:

- background removing;
- estimating the centroid (X, Y -coordinations of the geometrical centre of spot) of each 1st order diffraction spot
- estimating the distance between two spots at the same diagonal;
- assessing the mean value of light intensity coming from each 1st order spot.

The second approach exploited the Malus' law, which allows determining the intensity of light after its interaction with a polarizer

(vertical or horizontal), and assess the polarization based on following equations:

$$I_V = I_0(\cos \theta_V)^2 \quad (7.1)$$

$$I_H = I_0(\cos \theta_H)^2 \quad (7.2)$$

$$\theta_H = 90^\circ - \theta_V \quad (7.3)$$

Here, I_0 is the intensity of light before its interaction with a polarizer. I_V and I_H correspond to the intensity of light transmitted by a polarizer, vertical or horizontal, respectively. θ_V and θ_H correspond to the initial polarization of light before its interaction with a polarizer (vertical or horizontal, respectively)

$$I_H = I_0(\cos(90^\circ - \theta_V))^2 \quad (7.4a)$$

$$I_H = I_0(\sin \theta_V)^2 \quad (7.4b)$$

$$I_H = I_V(\tan \theta_V)^2 \quad (7.5a)$$

$$\frac{I_H}{I_V} = (\tan \theta_V)^2 \quad (7.5b)$$

$$\theta_V = \tan^{-1} \sqrt{\frac{I_H}{I_V}} \quad (7.6)$$

In this approach, the initial polarization of light is defined by the angle θ_V , which corresponds to the orientation of the electrical vector in XY -plane, as depicted in Fig. 7.1

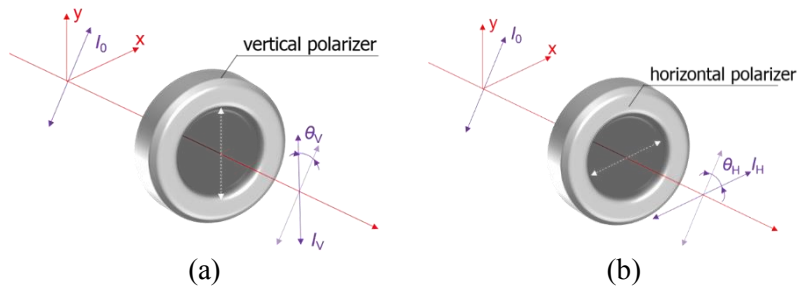


Figure 7.1. Sketches describing the interaction of the light with the polarizers by means of Malus' law, the same notations have been used in the equations 7.1. – 7.8.

With regard to the experiment two cases are taken into account: a) the light interacts with the vertical polarizer, b) the light interacts with the

horizontal polarizer. Here, I_0 is the initial intensity; I_V and I_H are the light intensity after interaction with the vertical and the horizontal polarizer. θ_V and θ_H are angles between the initial polarization and the main axis of the vertical and horizontal polarizer, respectively.

7.2 Experimental set up

The sketch of the measurements set up is reported in figure 7.2 and is constituted by:

- a semiconductor laser diode (NovaPro, rgb lasersystem) (1) providing monochromatic, coherent light with wavelength $\lambda = 405\text{nm}$;
- optical elements: optical filters (their optical density (OD) values and their quantity depended on the quality of image registered by CCTV camera) (2), depolarizer (3), vertical polarizer rotated in XY – plane (4), positive lens ($f = 15\text{ cm}$) (5);
- linear stage to stretch the sample along x -axis (6);
- CCTV camera (Panasonic, WV – BP510) to record the diffraction image projected on the screen.

The numbers (1) – (6) correspond to the components in Fig.7.2.

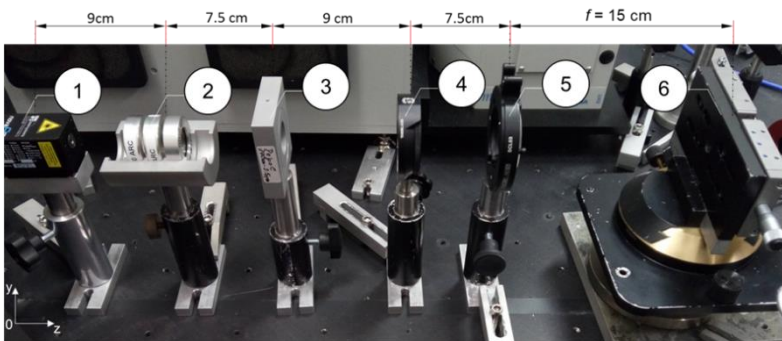


Figure 7.2. The experimental set up view. The numbers refer to the components as follow: 1 – laser diode, 2 – the set of optical filters, 3 – depolarizer, 4 – the vertical polarizer (V-polarizer), 5 – the positive (focusing) lens, 6 – the linear stage for one-dimensional sample stretching.

In the experimental setup, the incident light beam was provided by the laser diode. Initially, it was polarized vertically and its power was equal to $\sim 140\text{mW}$. The light illuminated the sample at the 0° angle. At these conditions, the diffracted image was too bright to be collected by the camera. Hence, it was necessary to apply a set of optical filters, whose quantity and optical density values were determined experimentally to avoid saturation of the camera.

Referring to the second approach, two complementary strategies have been taken into account.

- 1) In the first one, in order to ensure a vertical polarization, the light was initially depolarized and then polarized again by passing through the V-polarizer (see Figure 7.2).

The light beam was focused by the positive lens on the sample which was placed at the distance $f = 15\text{cm}$ from the lens. The diffraction image was projected on the screen behind the sample and recorded by the camera. It was placed at the distance of 79 cm from the screen, and connected directly to a computer equipped with PowerDirectorPro software for screening and saving the image of diffraction pattern. In the second one, the experimental setup did not contain the depolarizer and the V-polarizer (see Figure 7.3). The vertically polarized light was focused by the positive lens on the sample. After passing through the sample, the light was illuminating the polaroid-type polarizer. In fact, the diffraction pattern was induced by diffracted light polarized vertically or horizontally, alternatively. The diffraction image projected on the screen was recorded by the CCTV camera.

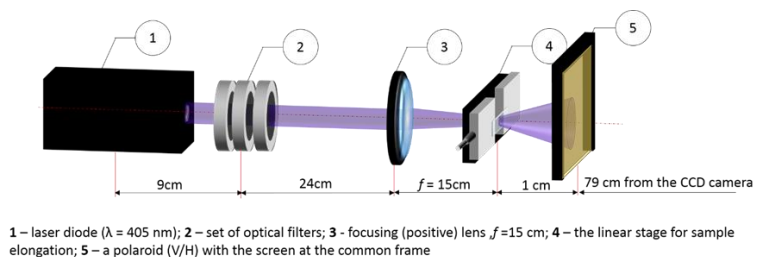


Figure 7.3. The experimental setup on which the intensity of the laser was appropriately modulated by optical filters.

In any case the focalization on the sample is provided by the use of a positive lens as reported in Figure 7.2 and Figure 7.3. This permits increasing the resolution of the image where a clearer image of the diffraction pattern is achieved as shown in Fig. 7.4a and Fig. 7.4.b.

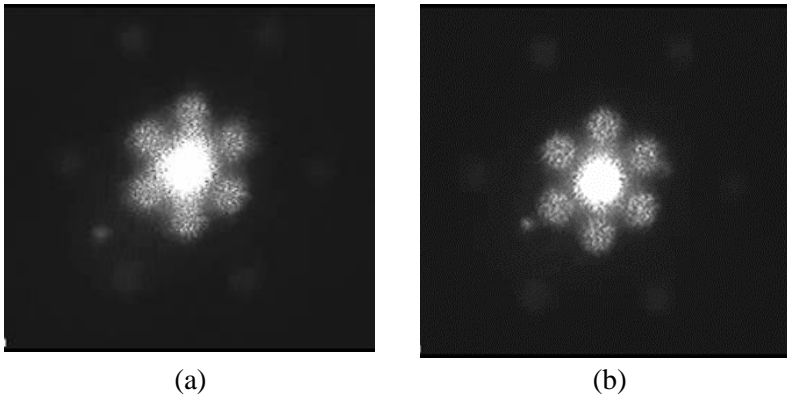


Figure 7.4. The diffraction image obtained a) without the positive lens; b) with the positive lens.

- 2) To verify the response of the sample to an axial applied strain it was fixed to the linear stage and stretched symmetrically along OX axis in several steps every 200 μm (100 μm at each side) up to the total elongation of 2000 μm . By the interaction of the laser diode ($\lambda = 405\text{nm}$) with the sample under elongation, the structural deformation was detectable analysing the shape changes in the diffraction image. The image was screened in real time by the computer and saved by the software. In the second approach, the effect of the elongation has been studied considering the variation in polarization. For each step of elongation (starting with the non-elongated state) the polarization of illuminating light beam was switched from $\theta = 0^\circ$ to $\theta = 180^\circ$. The horizontal polarization refers to the electrical vector along OX axis. The polarization was switched every 4° manually by rotating the V-polarizer in XY plane. In this case, the V-polarizer was working as filter that transmitted only the light with polarization corresponding to the direction of main axis of V-polarizer. For each step of elongation, the CCTV camera collected a series of diffraction images. Each image corresponds to the θ – value from 0° to 180° .

diffraction images. Each image corresponds to the θ – value from 0° to 180° .

7.3 Results

Before starting data analysis based on the images, it is necessary to remove the background which provides additional errors. The background is considered as the average value of brightness measured for different areas between the central spot and the 1st order diffraction spots. This value corresponds to the lower threshold value and all areas with the brightness value below the threshold will be depicted in black (0 in the greyscale). The upper threshold value is set automatically, and corresponds to the maximum of greyscale (255 corresponding to white colour). The first image of Figure 7.5 is the original one taken by the camera and the next three images correspond to the same diffraction pattern after the removal of the lower threshold value.

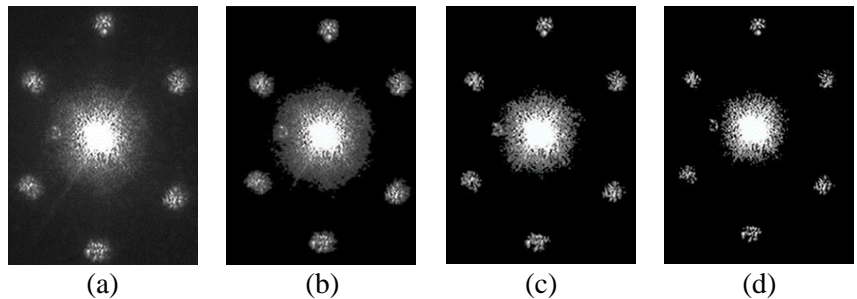


Figure 7.5. a) The original view of diffraction pattern taken by the CCTV device; and after background removal, whose impact value was equal to b) 50, c) 80, and d) 100.

The changes in the shape of diffraction pattern were estimated by measuring the distance between spots at the same diagonal. The distance was measured between the centroids (the geometrical centre of spot). The measurements were performed in pixels. However, the results were converted into centimeters based on relation that 1 cm of diffraction pattern projected onto the screen corresponds to 179 pixels at the image. Figure 7.6 reports the distance between the spots as a function of the applied strain values that were calculated applying the following equations.

$$\varepsilon = \frac{\Delta l}{l_0} \tag{7.9}$$

where Δl is the total elongation of sample after each step $dl = 200\mu\text{m}$, and l_0 is the initial length of the investigated area, which was the same for all measurements and amounted 9mm.

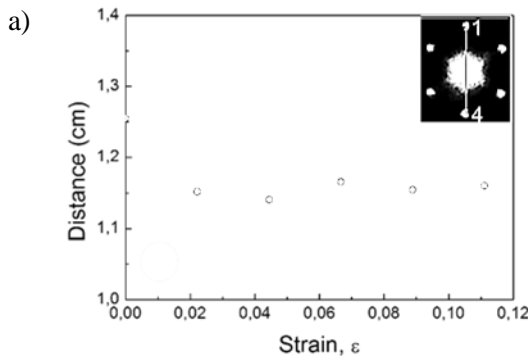
Based on eq. 7.9 it is possible to define strain as a function of length for a stretched sample:

$$\varepsilon = \frac{l-l_0}{l_0} = \frac{l}{l_0} - 1 \tag{7.10}$$

Table 7.1. The values of sample elongation (the first row) with the corresponding strain values.

$\Delta l [\mu\text{m}]$	0	200	400	600	800	1000	1200	1400	1600	1800	2000
ε	0	0.022	0.044	0.067	0.089	0.111	0.133	0.156	0.178	0.200	0.222

The graphs depicted in Fig. 7.6 show the relation between the distances in diffraction pattern and the strain. The inset pictures show the corresponding couple of spots for which the measurements were performed.



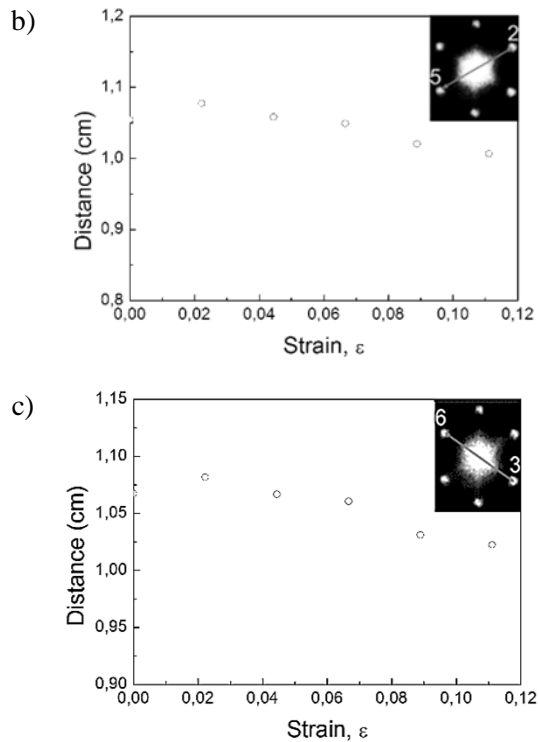


Figure 7.6. The distance variations as a function of strain for three couples of 1st order spots.

Figure 7.7. depicts the optical response (the intensity of diffracted light) as a function of polarization of light illuminating the sample. Each plot corresponds to different steps of elongation: the circle points refer to the unstretched sample, the triangle points are attributed to the sample elongated at about 400 μm , and the cross points correspond to the sample elongation equal to 1000 μm .

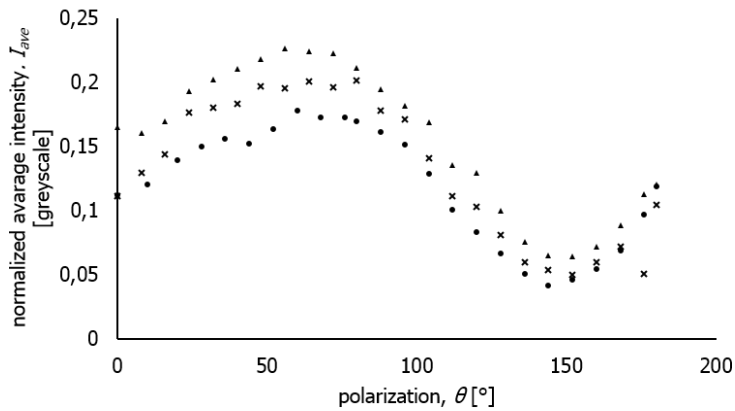


Figure 7.7. Light intensity as a function of the polarization of the incident beam (varying from 0° to 180°) using the set up reported in Figure 7.3. The black, circle points refer to the unstretched sample, the grey triangle points correspond to the elongation of $400\mu\text{m}$, and the grey cross points are related to the elongation at about $1000\mu\text{m}$.

In Tables 7.2 and 7.3. the evolution of the electrical field in XY -plane are reported.

In the specific table 7.2 shows the position of electrical field vector in XY -plane, which is perpendicular to the direction of light propagation. The position of electrical field in XY -plane is determined by the angle θ , as described in section 7.1 and reported in Table 7.2.

Table 7.2. a) Evolution of electrical vector in XY -plane, determined for different values of strain (the columns) and different spots (the rows).

ϵ	Evolution of electrical field vector					
0,000						
0,022						

0,044						
0,067						
0,089						
0,111						
0,133						
0,156						
0,178						
0,200						
0,222						

The table 7.3. summarizes the values of θ . Each value corresponds to the different orientations of electrical vector in table 7.2.

Table 7.3. The values of angle determining the position of the electrical field vector in *XY*-plane (θ is an angle between the vector of electrical field and *OY*-axis

ε	θ -values ($^\circ$) for:						
	central spot	spot 1	spot 2	spot 3	spot 4	spot 5	spot 6
0,000	30,4	5,0	7,5	7,5	5,6	6,4	6,3
0,022	33,6	9,4	11,8	12,9	10,1	9,7	11,8
0,044	25,3	6,8	9,3	13,1	8,1	7,1	7,9
0,067	24,9	6,5	7,7	10,1	6,5	6,9	8,4
0,089	25,2	6,6	7,9	10,1	6,8	6,8	8,4
0,111	26,1	7,9	12,6	14,3	9,5	9,3	10,8
0,133	25,4	7,7	12,0	13,9	9,2	9,0	10,1
0,156	27,0	8,7	13,0	15,5	11,1	11,6	13,3
0,178	26,6	8,4	13,6	15,1	10,5	10,7	12,7
0,200	27,7	9,4	13,4	15,6	11,8	12,2	12,6
0,222	28,0	12,0	16,7	19,7	15,7	15,7	16,4

7.4 Discussion

The measurements of shape deformation of diffraction pattern (Fig. 7.6) show the linear relation for the couple of spots 2 and 5, and the couple of spots 3 and 6. In particular, a linear behavior has been evidenced in the strain range from 0 to 0,111, where $\varepsilon = 0,111$ corresponds to the elongation $\Delta l = 1000 \mu\text{m}$. The results plotted in Fig. 7.7. shows the sample response as a function of the polarization of the incident light, where the same trend is observed suggesting that for this range of elongation, the applied strain does not affect significantly the optical response.

This is also confirmed by the results depicted in Table 7.2 and 7.3 where comparable values of θ have been determined, suggesting that for this range of applied strain the approach considering the different response in polarization is less sensitive respect to the one studying the distances in diffraction pattern.

7.5 Conclusions

In this chapter different approaches have been employed in order to study the optical response and the sensitivity of the realized two-dimensional diffraction grating. In this case, the response has been

obtained by transmission measurements; the light diffracted by the circular apertures (holes at the top surface of sample) creates a diffraction pattern composed of 0th order spot in the center, surrounded by six 1st order spots forming a hexagon. Applied stress affects the diffraction pattern in two ways:

- by modifying its shape;
- by changing the brightness.

Hence, the structural deformations can be detected in two ways:

- by measuring the distance variations between spots at the same diagonal
- by controlling the polarization of diffracted light, based on Malus' law

The first approach referred to the shape variations of diffraction pattern. Its results confirmed a linear relation, in the range between 0 and 0,111 ϵ , between increasing strain and the distance of the diffracted spots. In fact, a decrease of the distance for the couple of spot 2 and spot 5, and for the couple of spot 3 and spot 6 is observed in agreement with the optical spectra discussed in chapter 6.

The unexpected behavior evidenced with higher strain values could be associated to the symmetry distortion of diffraction pattern.

The second approach concerns the variation of the optical response as a function of the applied axial strain by means of polarization measurements.

Considering the results obtained the approach proposed seems to be less sensitive respect to the one studying the distances in diffraction pattern. However, it is possible to expect an improvement on the sensitivity using the polarization measurements modifying the excitation wavelength employing the higher efficiency of diffraction grating at higher wavelength respect to $\lambda = 405$ nm.

In any case the approach in transmission allowed to determine the sensitivity of the diffraction grating which is comparable with those reported for mechanochromic sensors. Moreover, the approach proposed can be considered a versatile tool for the development of sensors with an easy readout method.

Chapter 8

Strain sensitivity estimated by measurements in reflection mode, referring to the shape changes of diffraction pattern and the polarization of diffracted light

8.1 Introduction

In the previous chapters, the optical response of the grating has been investigated exploiting complementary approaches based on the transmission mode. In these cases, a white light or a laser at ($\lambda = 405$ nm) impinged on the sample and through the analysis of the diffracted wavelengths and by the changes in the diffraction pattern has been verified that, the application of a strain, produces a variation in the periodicity due to a change in its structural and morphological features. Finally, these through there measures, measurements have permitted to determine the sensitivity of the grating has been determined.

In this chapter are reported the experimental conditions employed to investigate the optical response of the grating under a uniaxial strain by reflection measurements. Unlike in transmission mode, in the reflection mode the incident beam and the reflected beam will be at the same side of the sample. This configuration approach wants to simulate the real situation, although in laboratory, in order to prove that this type of sensor could find application in the field of SHM.

Moreover, if compared with the approaches reported in chapter 6 and 7, this kind of investigation possesses two advantages:

- it reduces the size of the setup significantly;
- it gives the possibility to realize the diffraction grating using a non-transparent substrate.

More details concerning the properties and possible applications of the grating are for example reported in (Palmer and Loewen 2005) where

pro and con are highlighted. Briefly the reflection gratings significantly reduce the dimension of the measurement systems, due to the arrangement of the source, the optical elements and the detector (Palmer and Loewen 2005). Furthermore, reflection gratings are not limited by the transmission properties of grating substrate, and they provide more diffraction angles.

Speaking about possible applications, it is worth mentioning that diffraction gratings are often used in monochromators, spectrometers, lasers, wavelength division multiplexing devices, optical pulse compressing devices, but also for the development of sensors; considering this last aspect both transmission and reflection interrogation mode have been employed. In fact, they have been used in order to realize chemical (Cai et al. 2014) and biological (Cai et al. 2015) sensors, but also physical ones (Yu et al.2010).

Some insight on strain sensitivity of diffraction gratings has already been reported and discussed in details in e.g. (Kim et al. 2000; Zhao and Assundi 1999; and Minati et al.2017), considering one-dimensional diffraction gratings.

The aim of this chapter is to demonstrate the sensitivity of this kind of sample in the reflection mode. As mentioned above, the elongation of the sample clearly influences its optical response and, as happened in chapter 7, this was detected by collecting the diffraction pattern with the CCTV camera.

8.2 Experimental setup

The sketch and the measures of the elements that compose the set up are reported in figure 8.1. It is constituted by:

- a laser diode emitting monochromatic ($\lambda = 405 \text{ nm}$) coherent light;
- a depolarizer;
- a vertical polarizer (V-polarizer)
- a positive (focusing) lens with the focus length $f = 15 \text{ cm}$
- a linear stage for one-dimensional sample stretching;
- a polaroid-type polarizer;
- a CCTV camera.

The light emitted by the laser diode was initially vertically polarized (the vertical electrical vector in the XY - plane perpendicular to the direction

of light propagation). A set constituted by a depolarizer and V-polarizer, this last one mounted on a rotator stage allowed controlling the state of the light polarization. Then a lens permitted to focus the beam on the grating area. Screen and camera were placed as shown in Figure 8.1 b. The diffraction pattern was projected on the screen, and all changes of its brightness and in its shape were registered by the CCTV camera.

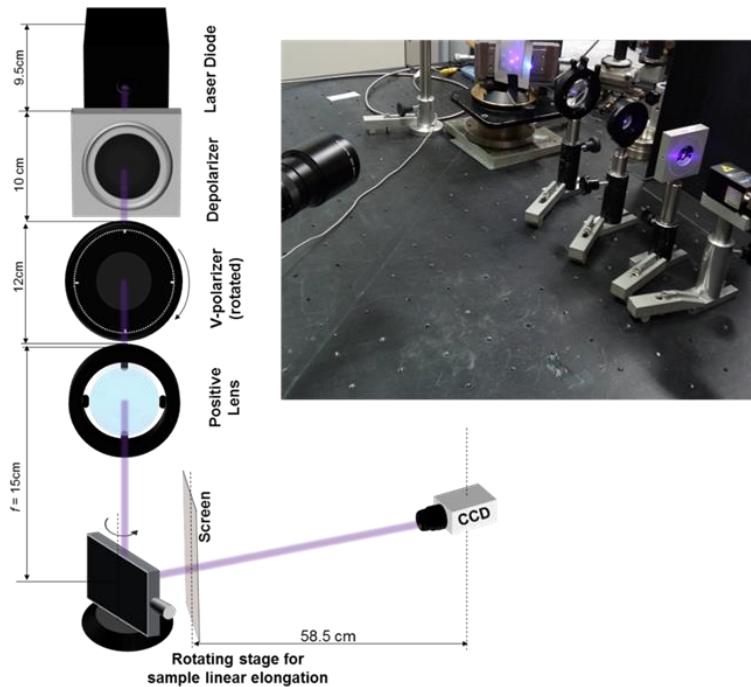


Figure 8.1. Scheme of the experimental setup to measure the geometrical changes of diffraction pattern.

In the second approach, to estimate the polarization of reflected beam, the polaroid-type polarizer was placed before the screen.

In both approaches, the images of diffraction pattern were taken by the CCTV camera, positioned at the distance of 58.5 cm from the screen (Fig.8.1) and at the distance of 72.5 cm from the polarizer (Fig.8.2.).

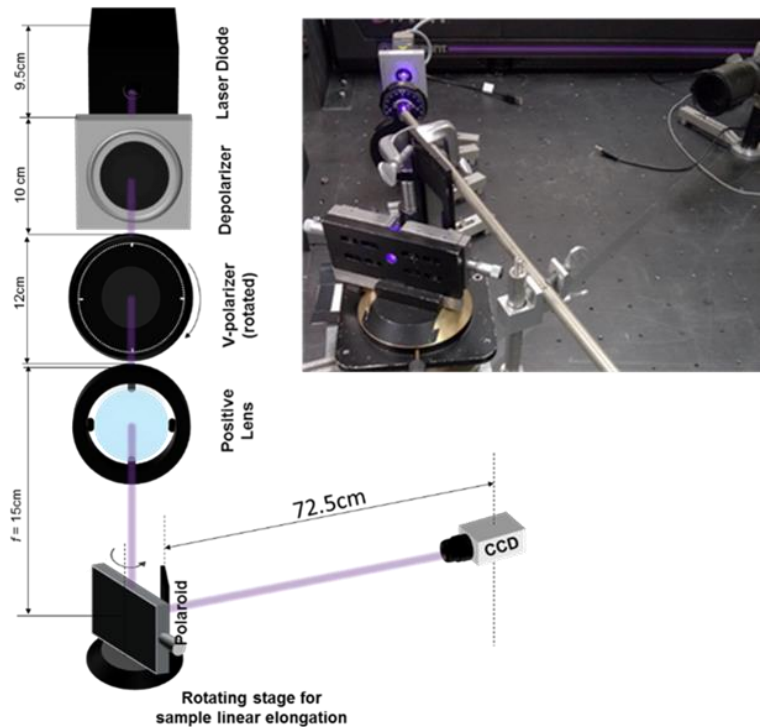


Figure 8.2. Scheme of the experimental setup to measure the polarization. The inset image shows its real view.

All parameters (depicted in Fig.8.3), such as the incident angle between the normal to the surface of the sample and the illuminating beam, and also the distance between the sample and the polaroid/ the screen were found experimentally with respect to the following conditions:

- the complete diffraction image should be observable with the naked eye i.e. all six 1st order spots of the first order surrounding the central one;
- the brightness of diffraction pattern should be sufficient to perform measurements after removing the background.

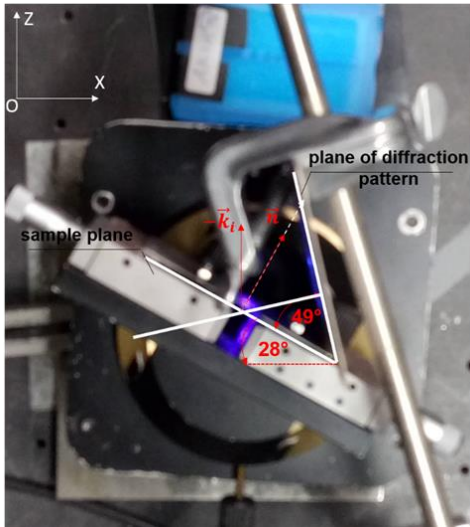


Figure 8.3. The arrangement of screen and sample in the experimental setup. Here, \vec{n} terms the normal to the sample plane, and $-\vec{k}_i$ is the wavevector of incident/illuminating light.

8.3 Results and Discussion

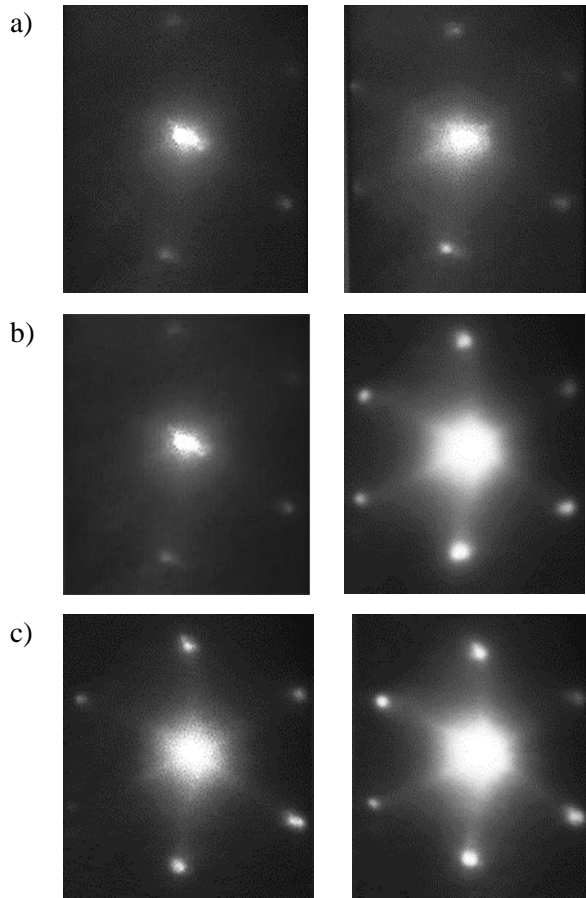
In order to make a comparison with the experiments reported in the previous chapter, the same stimulus, meaning the same elongation, has been applied to the sample. In fact, it has been stretched symmetrically with steps of $200 \mu\text{m}$ (the sample was elongated $100 \mu\text{m}$ at each side) up to the value of $2000 \mu\text{m}$. During the elongation, the laser light was impinging on the periodic structure, the reflected beam was illuminating the screen, and the diffraction pattern image was collected by the camera in order to visualize any structural change.

Speaking about the polarization measurements, the screen was illuminated by the light polarized vertically when the main axis of polaroid was vertical, or horizontally when the main axis of the polaroid was horizontal. In both cases, the camera took the picture of diffraction pattern.

Considering the initial experimental conditions that have been chosen, it has been verified that, for the incident light with an in-plane wavevector along Γ -K axis, there is a variation in the intensity of the diffraction patter for four different polarizations (Vertical, -45° , $+45^\circ$,

H) as reported by J. Sun et al. (Sun 2010); this means that the structure is polarization sensitive.

In Fig.8.4 are shown the diffraction patterns for different polarization angles of illuminating beam, where all pictures were taken at the same conditions i.e. the distance between the polaroid-type polarizer and screen was the same, the incident angle of illuminating light was identical, and the sample was not stretched.



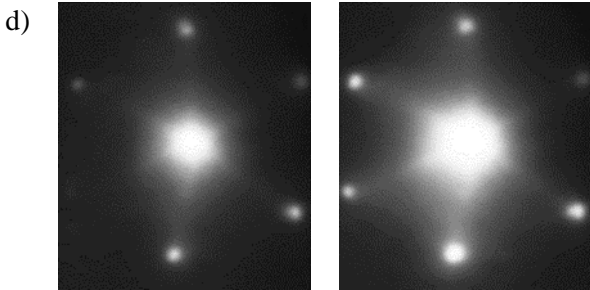


Figure 8.4. Diffraction patterns with differently polarized light: (a) vertically; (b) at the angle (-45°); (c) horizontally; (d) at the angle (45°). The left-handed images correspond to the vertically polarized light reflected at the periodic structure, whereas the right-handed images correspond to the horizontal polarization of reflected light.

After collecting all the diffraction patterns, in order to easily study the optical response of the system, the image taken for a tilted polarized light (at the angle (-45°) has been chosen. In fact, this configuration shows a diffraction pattern, where all the six 1st order diffraction spots are visible and the level of their intensity is “sufficient” to employ the same approach used in chapter 7 in order to determine the sensitivity of the grating. In Figure 8.5 are reported the distances between the spots as a function of the applied strain values that were calculated applying the equation 7.9. Analysing the graphs is possible to notice a linear relation for the couple of spots 1-4, 2-5, and for the couple 3-6. In particular, a linear behaviour has been evidenced in the strain range from 0 to $0,089\epsilon$ in agreement with the results reported in chapter 7. For higher strain values the behaviour is not linear probably due to a different response of the PDMS matrix. However, although the measurements in the reflection mode are suitable with respect to applications in strain sensors, the applied approach based on the geometrical changes of diffraction images strongly depends on the arrangement of screen and sample, which is strictly determined by the incident angle, the diffracted angle, and the angle between the screen plane and the sample plane.

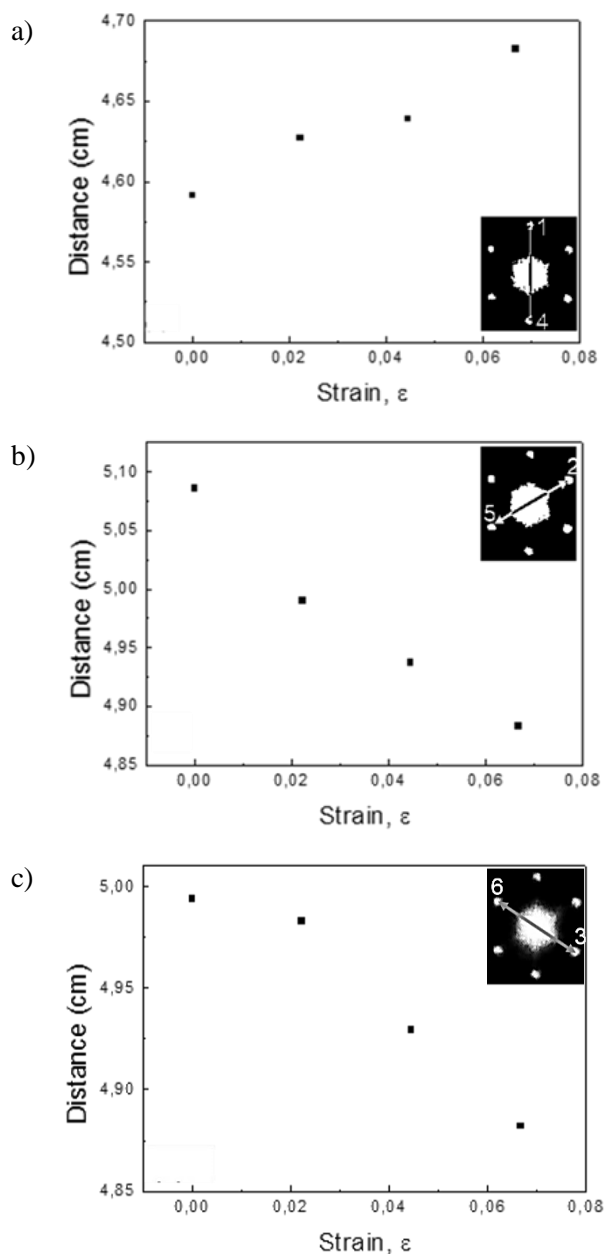


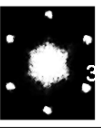


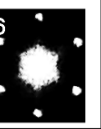
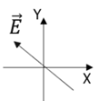
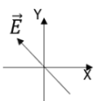
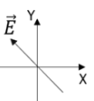
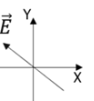
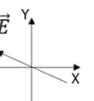
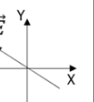
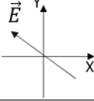
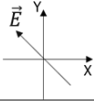
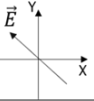
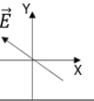
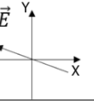
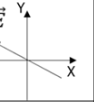
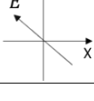
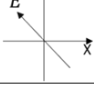
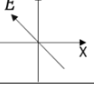
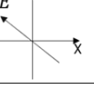
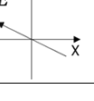
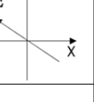
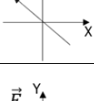
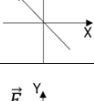
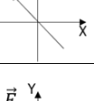
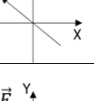
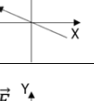
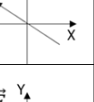
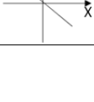
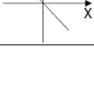
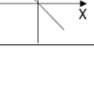
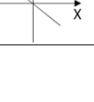
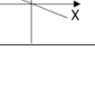
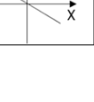


Figure 8.5. The distance variation between two spots at the same diagonal (the couple of spots is shown in the inset picture).

The analysis of the optical response as a function of the polarization state has been performed in the same way as for the transmittance

approach. Table 8.1. reports the orientation of electrical vector for each spot and each strain value ranging from 0 to 0,089.

Table. 8.1. Orientation of electrical field vector in *XY*-plane determined for each spot (shown in the first row) and each strain value separately.

						
ε	Evolution of electrical field vector					
0,000						
0,022						
0,044						
0,067						
0,089						

In Table 8.2. are summarized the values of θ . Each value corresponds to the different orientations of electrical vector in Table 8.1.

Table 8.2. The values of angle (θ) corresponding to each position of the electrical field at table 8.1 vector in XY -plane (θ is the angle between the electrical vector and OY -axis)

ε	θ - values ($^\circ$) for:						
	central spot	spot 1	spot 2	spot 3	spot 4	spot 5	spot 6
0,000	48,9	48,9	43,5	44,2	51,9	65,8	57,3
0,022	48,8	48,8	44,9	47,7	54,6	70,0	62,1
0,044	49,0	49,0	43,2	43,9	51,6	64,2	56,3
0,067	49,1	49,6	43,7	43,4	50,9	66,4	56,8
0,089	49,0	50,3	43,1	44,0	51,5	68,3	58,9

The results shown in Table 8.1 and 8.2 suggest that for this range of elongation, the applied strain does not affect significantly the optical response in agreement with the data obtained by the transmission approach. In fact, every step of elongation equal to $200\mu\text{m}$ increases the strain at about 0,022, and switches the polarization about $\Delta\theta = 0,1^\circ$ for the central spot, and for the 1st order spots so that $\Delta\theta = \{2,1^\circ$ (spot 1); $1,05^\circ$ (spot 2); $2,1^\circ$ (spot 3); $1,8^\circ$ (spot 4); $3,5^\circ$ (spot 5); $3,3^\circ$ (spot 6) $\}$. These values are the average values of polarization variation assessed for the first four steps of elongation, with respect to the limit of $\varepsilon = 0,089$. As previously, the different response in polarization is less sensitive than calculating the distances of the diffraction pattern.

8.4 Conclusions

In this chapter, a reflection based approach has been developed and discussed with the aim to investigate the possibility to use the realized grating as strain sensor. In particular, the method that has been described here, allows using this system for Structural Health Monitoring (SHM) purposes

As in the previous chapters, the results were obtained analysing the changes in the diffraction pattern. Hence, the measurements referred to the geometrical changes in its shape, and in the intensity variation as a function of the polarization of the impinging light.

Initially the measurements were performed considering the shape variations of diffraction pattern induced by the application of a uniaxial strain. However, this approach requires high precision in the alignment of the screen and the sample as well as camera, where a proper

positioning plays a crucial role.

The second approach concerns the variation of the optical response as a function of the applied axial strain by means of polarization measurements. A negligible variation in the intensity, as a function of the polarization of the impinging light, during the elongation, has been observed; this could be a consequence of the mismatch between the illuminating wavelength and the pitch. A possible solution could be the approach proposed by (Jing, Wu and Lin 2014), using as excitation source light with a wavelength equal to the half of pitch.

In any case the approach in reflection mode that has been proposed allows to confirm the results reported in chapters 6 and 7 meaning the linear response and the sensitivity of the sensor.

Moreover, the approach proposed here could be considered a versatile tool for the development of sensors with an easy readout method that can be used in the field of SHM.

Chapter 9

Conclusions and further developments

9.1 Conclusions

The experimental part of this work refers to three experiments, which each of them presents other optical approach to detect mechanical distortion of periodic structure. The periodic structure involved in the experiments was fabricated as a thin molded layer. It includes a hexagonal arrangement of semiholes. The analysis of sample morphology performed by atomic force microscope (AFM) and scanning electron microscope (SEM) confirmed a periodic, hexagonal arrangement of semiholes. However, the AFM images provide deep analysis of profile of voids, that is strongly non-uniform. In addition, the top-view SEM images taken for a larger sample area depict structural veins and discontinuities, which are imperfections typical for a self-assemble product.

The sample fabrication hired “natural lithography” approach, which is defined as a combination of self-assemble method and one of lithography techniques (Zhao et al. 200). The self-assemble approach was applied to produce the direct structure (the template) of MCC. By PDMS deposition, followed by its removal, the spheres were transferred into PDMS matrix (the MCC replica on a PDMS substrate). The next step involved wet- etching with DMF, what resulted in the inverse replica of MCC. This structure exhibits diffractive properties (a biperiodic/ two-dimensional diffraction grating), which results in the blaze effect on its top surface (the multicolour pattern on the molded layer) indicate by illuminating white light.

Further investigations exploit diffractive properties of the structure by light transmission (chapter 6 and 7) and reflection (chapter 8).

In general, diffraction gratings are considered as an optical instrument, which optical response (a diffracted light) depends strongly on their geometry. Hence, applied stretching indicates structural changes influencing parameters of diffracted light.

In this work, three approaches to detect these changes were tested. Two of them control the diffracted light parameters such as: diffracted wavelength (chapter 6) and polarization (chapters 7 and 8). The third one involves shape changes in diffraction pattern, which is a visible product of light interaction with the periodic structure, to assess structural changes of diffraction grating.

In this work, the major attention was focused on methodology i.e. measurements conditions, accurate applied optical method (including selection of monitored parameter) and accurate instruments for registration the results. However, the reliability of measurements is determined not only by methodology but also by the quality of the object/ sample, which in this case depends on the applied fabrication technique.

The involved materials in the fabrication exhibit valuable features such as:

- polymers are easily available and low-cost materials (considering their price and no special fabrication conditions required such as clean-room conditions)
- PDMS are an elastomer with easily tunable properties (), compatible with lithography techniques, appropriate for commercial application because it is non-toxic, environmental friendly, transparent, light-weight and flexible.

However, the fabrication protocol requires optimization. Current approach is a combination of self-assembly method assisted by wet etching. Alternatively, referring to the theory about monolayer colloidal crystals and their derivatives in Chapter 5, there is worthy to consider one of natural lithography techniques (self-assembly assisted by one of lithography techniques), which allows to control features and parameters of final product.

The spectroscopic approach (chapter 6) based on the analysis of diffracted light spectrum allows to analyze only effects on the sample surface. The obtain results suggest that the applied stress results in shape transition from spherical to elliptical, what corresponds to changes of pitch in XY – plane (the plane of periodicity).

Chapter 7 and chapter 8 present two approaches to determine the strain. In the first approach the geometrical changes of diffraction pattern are estimated by using a CCTV camera. In the second approach, the polarization of diffracted light is analyzed based on variations of diffraction pattern brightness.

The measurements of geometrical changes in the diffraction pattern show the linear relationship between the applied stress and distance variations between two spots at the common diagonal.

For sample illumination with the wavelength $\lambda = 405$ nm, the measurements of polarization exhibit less sensitivity to deformation than diffraction pattern, what can be a result of the mismatch between the grating pitch and the exciting wavelength.

9.2 Further developments

The experiments provide valuable and promising results to perform further investigations on strain sensitive materials and optical techniques to detect structural deformation. Hence, some aspects of methodology should be modified to obtain reliable results:

- the total elongation of sample should not cross the value corresponding to $\varepsilon = 0.111$; above this limit the deformation should be considered as non-reversible structural changes inducing a permanent disorder of the structure geometry;
- with respect to the experimental results presented in (Khodadad, Dhindsa and Saini 2016), there is worthy to measure the light intensity provided by 2nd order diffraction spots, whose variations are more significant than in case of 1st order diffraction spots.
- the experimental results presented in chapters 7 and 8 show that the polarization of diffracted light is affected not only by the shape of voids (the surface effects), but also variation of volume parameters (the slope of wells and the depth of grooves) should be considered. They can be assessed by applying ellipsometric approach based on Mueller matrix formalism, as suggested in (Garcia-Caurel et al. 2013)
- Garcia-Caurel with his co-workers showed that ellipsometric approach is valuable for assessing the structural parameters as well as to reconstruct a grating profile. Hence, it can be used to demonstrate:
 - variations of volume parameters stimulated by deformation;
 - changes in grating profile during elongation.

In ellipsometric approach, the system is described by transmission/reflection matrix, whose components depend on grooves parameters.

Changes in methodology will influence the configuration of experimental setups. As suggested in (Palmer and Loewen 2004), to measure the light intensity, there is better to use other detector than a CCD camera or similar devices providing results as images, because of:

- optical noises resulted from light interaction with a screen plane (speckles on the image background);
- removal of the noises provides additional errors to measurements;
- The measurements need to be performed in grey scale; hence the maximal measured intensity value is 255 (the highest value in the grey scale corresponding with white colour)

Hence, in an alternative experimental setup the CCTV camera should be replaced by two photodiodes. Each photodiode should be assisted by a filter to cut off undesired wavelengths (to avoid optical noises), and connected with two different channels of oscilloscope. An oscilloscope provides following benefits:

- the saturation effect is avoidable by manipulating the range of measurements;
- two different channels enable simultaneous control over optical response from two diffraction spots at the same diagonal; and results displayed at two separated graphs in real time.
- the oscilloscope provides quantitative and qualitative measurements of polarization (the value and the type of polarization can be determined)

Other appealing problem is the magnification effect of diffracted image. However, it is also avoidable by applying a collimated lens. A collimated lens transformed the spherical wavefront into the planar one. In fact, increasing distance between a detector and sample does not result in increasing diffraction image and decreasing intensity of diffraction light.

Above considerations provide many opportunities to develop each experiment by optimization the fabrication protocol and methodology including experimental setups and data collection

References

- Abdelsalam, M. E., S. Mahajan, P. N. Bartlett, J. J. Baumberg, and A. E. Russell. 2007. "SERS at Structured Palladium and Platinum Surfaces." *Journal of American Chemical Society* 129(23): 7399 – 7406.
- Alcock, R. D., C.D. Creasey, P. Wileman, N.A. Halliwell, and J.M. Coupland. 2004. "Remote Detection of the Pitch and Orientation of a Reflective Diffraction Grating: An Optical Strain Gauge." *Proc. R. Soc. A* 461(2053): 179 – 188. doi: 10.1098/rspa.2004.1390.
- Allix, O., and P. Vidal. 2002. "A new multi-solution approach suitable for structural identification problems." *Computer methods in Applied Mechanics and Engineering* 191: 2727 – 2758.
- Antonakakis T., et al., *Gratings: Theory and Numeric*, HAL Id: hal-00785737.
- Asundi, A., and S. Zhao. 2000. "Optical strain sensor using position-sensitive detector and diffraction grating: error analysis." *Optical Engineering* 39(6): 1645-1651.
- Avril, S., A. Vautrin, E. Ferrier, P. Hamelin, and Y. Surrel. 2004. "Experimental analysis of reinforced-concrete beams repaired with CFRP sheets." *Composites Part A: Applied Science and Manufacturing* 35(7–8): 873 – 884.
- Ayres, J.W., F. Lalande, Z. Chaudhry, and C.A. Rogers. 1998 "Qualitative impedance-based health monitoring of civil infrastructures." *Smart Materials and Structures* 7 (5): 599 – 605
- Bakis, C.E., K.L. Reifsnider. 1987. "Nondestructive Evaluation of Fiber Composite Laminates by Thermoelastic Emission". In *Review of Progress in Quantitative Nondestructive Evaluation*, edited by Thompson D.O., D. E. Chimenti, 1109-1116. Berlin: Springer.

- Balaban, N.Q., U.S. Schwarz, D. Riveline, P. Goichberg, G. Tzur, I. Sabanay, D. Mahalu, S. Safran, A. Bershadsky, L. Addadi, et al. 2001. "Force and focal adhesion assembly: a close relationship studied using elastic micropatterned substrates." *Nature cell biology* 3(5): 466 – 472.
- Bartl, H. M. 2014. "Butterfly-inspired Photonics Reverse Diffraction Colour Sequence." *Proceedings of the National Academy of Sciences* 111(44): 15602-15603. doi: 10.1073/pnas.1418292111.
- Bell, J. F. 1956. "Determination of Dynamic Plastic Strain through the Use of Diffraction Gratings." *Journal of Applied Physics* 27(10): 1109–1113.
- Bell, J.F. 1965. Optical strain Gauge. U.S. Patent 3,184,961.
- Bermel, P.A., and M. Warner. 2002. "Photonic band structure of highly deformable, self-assembling systems."

Physical Review E 65(1): 010702.

- Boeman, R.G. 1991. "Interlaminar deformation on the cylindrical surface of a hole in laminated composites: an experimental study." Phd diss, VirginiaTech.
- Bonod, N., E. Popov, S. Enoch, and J. Néauport. 2006. "Polarization insensitive blazed diffraction gratings." *Journal of the European Optical Society – Rapid Publications* 1: (06029) doi: 10.2971/jeos.2006.06029.
- Bruno O. P, and F. Reitich. 1993. *Numerical Solution of Diffraction Problems: A method of Variation of Boundaries III. Doubly Periodic Gratings*. Research Report No. 93-NA-003. North Carolina: U.S. Army Research Office, Research Triangle Park. Washington, DC: National Science Foundation.
- Bulhak J, and Y. Surrel. 1999. "Grating Shearography.", *Proc. SPIE 3744, Interferometry '99: Techniques and Technologies*: 506 - 515
- Cai, Z., D.H. Kwak, D. Punihaole, Z. Hong, S.S. Velankar, X. Liu, and S.A. Asher. 2015. "A Photonic Crystal Protein Hydrogel Sensor for *Candida albicans*." *Angewandte Chemie International Edition* 54(44):13036-40.
- Cai, Z., J.-T. Zhang, F. Xue, Z. Hong, D. Punihaole, and S.A. Asher. 2014. "2D Photonic Crystal Protein Hydrogel

- Coulometer for Sensing Serum Albumin Ligand Binding” *Analytical Chemistry* 86(10): 4840 – 4847. doi: 10.1021/ac404134t.
- Chan, E.P., J.J. Walsh, A.M. Urbas, and E.L. Thomas. 2013. “Mechanochromic photonic gels.” *Advanced Materials* 25 (29): 3934 – 3947. doi: 10.1002/adma.201300692.
 - Chandra, D., S. Yang and P.-Ch. Lin. 2007. “Strain responsive concave and convex microlens arrays” *Applied Physics Letters* 91(25): 251912-1 – 251912-12.
 - Chen, C.G, and M. L. Schattenburg. 2004. “A Brief History of Gratings and the Making of the MIT Nanoruler.” White Papers, etc. Space Nanotechnology Laboratory, MIT Kavli Institute for Astrophysics and Space Research, March 11. <http://snl.mit.edu/pub/papers/WP/Nanoruler-White-Paper.pdf>
 - Chen, F., G. Brown, and M. Song. 2000. “Overview of three-dimensional shape measurement using optical methods.” *Optical Engineering* 39(1): 10 – 22.
 - Chen, P.-W., and D. D. L. Chung. 1993. “Carbon fibre reinforced concrete for smart structures capable of non-destructive flaw detection.” *Journal of the American Ceramic Society* 78 (3): 816 – 818.
 - Chen, Z.M., T. Gang, X. Yan, X. Li, J. H. Zhang, Y. F. Wang, X. Chen, Z. Q. Sun, K. Zhang, B. Zhao, and B. Yang. 2009. “Ordered Silica Microspheres Unsymmetrically Coated with Ag Nanoparticles, and Ag-Nanoparticle-Doped Polymer Voids Fabricated by Microcontact Printing and Chemical Reduction.” *Advanced Materials* 18(7): 924 – 929.
 - Chiappini A. et al. *Optical Materials* (2013). <http://dx.doi.org/10.1016/j.optmat.2013.04.030>
 - Choi, D.G., H. K. Yu, S. G. Jang, and S. M. Yang. 2004. “Colloidal Lithographic Nanopatterning via Reactive Ion Etching.” *Journal of American Chemical Society* 126(22): 7019 – 7025.
 - Choi, D.G., S. G. Jang, S. Kim, E. Lee, Ch. S. Han, S. M. Yang. 2006. “Multifaceted and nanobored particle arrays sculpted using colloidal lithography” *Advanced Functional Materials* 16 (33): 33 – 40.

- Chung, D.D.L. 1998. “Self-monitoring structural materials.” *Materials Science and Engineering* 22 (2): 57–78.
- Cong, C. X., T. Yu, Z. H. Ni, L. Liu, Z. X. Shen, and W. Huang. 2009. “Controlled Fabrication of Hollow Metal Pillar Arrays Using Colloidal Masks” *Journal of Physical Chemistry* 18(26): 6103 – 6105.
- Deckman, H. W., J. H. Dunsmuir, and S.M. Gruner. 1989. “Microfabrication cellular phosphors.” *Journal of Vacuum Science & Technology B, Nanotechnology and Microelectronics: Materials, Processing, Measurement, and Phenomena* 7(6)(1832).
- Deckman, H. W., J. H. Dunsmuir, S. Garoff, J. A. McHenry, and D. G. Peiffer. 1988. “Macromolecular self-organized assemblies.” *Journal of Vacuum Science & Technology B, Nanotechnology and Microelectronics: Materials, Processing, Measurement, and Phenomena* 6 (1): 333 – 336.
- Denkov, N. D., O. D. Velev, P. A. Kralchevsky, I. B. Ivanov, H. Yoshimura, and K. Nagayama. 1992. “Mechanism of formation of two-dimensional crystals from latex particles on substrates.” *Langmuir* 8(12): 3183 – 3190.
- Deparis, O., M. Rassart, C. Vandenbem, V. Welch, J. P. Vigneron, and S. Lucas. 2008. “Structurally Tuned Iridescent Surfaces Inspired by Nature” *New Journal of Physics* 10 :013032. doi: 10.1088/1367-2630/10/1/013032.
- Dimitrov, A.S., and K.Nagayama. 1996. “Continuous Convective Assembling of Fine Particles into Two-Dimensional Arrays on Solid Surfaces.” *Langmuir* 12 (5): 1303 – 1311.
- Dubois, M., P. Lorraine, B. Venchiarutti, A. Bauco, and R. Filkins. 2000“Optimization of Temporal and Optical Penetration Depth for Lasergeneration of Ultrasound in Polymer-Matrix Composites.” In *Review of Progress in Quantitative Nondestructive Evaluation*, 287–294. Iowa State University Digital Press.
- Dunn, M. S, J.F. Williams, and R. Jones. 1988. “Thermoanalysis of composite specimens.” *Composite Structures* 11 (4): 309–24. doi: 10.1016/0263-8223(89)90094-9.

- Dziomkina, N. V., M. A. Hempenius, G. J. Vancso. 2005. "Symmetry Control of Polymer Colloidal Monolayers and Crystals by Electrophoretic Deposition on Patterned Surfaces." *Advanced Materials* 17(2): 237 – 240.
- Ettermeyer, A, and M. Honlet. 1994. "Nondestructive Testing with TV-Holography and Shearography. In: *VDI Berichte :IMECO Symposium: Laser Metrology for Precision Measurement and Inspection in Industry*, 33 – 38.
- Ettermeyer, A, Z. Wang, and T. Walz. 1997. "Application of 3d Speckle Interferometry to Material and Component Testing." *In: Proceedings of SPIE* ,188–94.
- Falldorf, C., S. Osten, C. Kopylow, and W. Jüptner. 2009. "Shearing interferometer based on the birefringent properties of a spatial light." *Optics Letters* 34(18): 2727 – 2729.
- Ferdinand, P. 2014. "The Evolution of Optical Fiber Sensors Technologies During the 35 Last Years and Their Applications in Structural Health Monitoring." Paper presented at the 7th European Workshop on Structural Health Monitoring, Nantes, July 8-11.
- Fiber-Optic Sensing Technologies. Introduction to Fiber-Optic Sensing. <http://www.ni.com/white-paper/12953/en/>.
- Garcia-Caurel, E., R. Ossikovski, M. Foldyna, A. Pierangelo, B. Drévillon, and A. De Martino. 2013. "Advanced Mueller Ellipsometry. Instrumentation and Data Analysis." In *Ellipsometry at the Nanoscale* edited by M. Losurdo and K. Hingerl, 31 – 143. Springer: Berlin, Heidelberg
- Gautschi, G. 2002. *Piezoelectric Sensorics: Force, Strain, Pressure, Acceleration and Acoustic Emission Sensors, Materials and Amplifiers*. Berlin: Springer
- Gaylord, T. K., and M. G. Moharam. 1985. "Analysis and Applications of Optical Diffraction by Gratings." *Proceeding of the IEEE* 73(5): 894 – 937.
- Grant, E., M. Kolle, P. Kim, Mughees Khan, P. Munoz, and J. Aizenberg. 2004. "Bioinspired Micrograting Arrays Mimicking the Reverse Colour Diffraction Elements Evolved by the Butterfly Pierella Luna." *Proceedings of the National Academy of Sciences* 111 (44): 15630-15634. doi: 10.1073/pnas.1412240111.

- Grédiac M., and L. Dufort. 2002. “Experimental evidence of parasitic effects in the rail shear test on sandwich beams.” *Experimental Mechanics* 42(2): 186 – 193.
- Grédiac, M, E. Toussaint, and F. Pierron. 2002. “Special virtual fields for the direct determination of material parameters with the virtual fields method. 1. Principle and definition.” *International Journal of Solids and Structures* 39(10): 2691–705.
- Grédiac, M. 2004. “The use of full-field measurement methods in composite material characterization: interest and limitations” *Composites: Part A* 35: 751 – 761.
- Grédiac, M., F. Auslender, and F. Pierron. 2001. “Applying the virtual fields method to determine the through-thickness moduli of thick composites with a nonlinear shear response.” *Composites: Part A* 32(12):1713 – 1725.
- Grédiac, M., N. Fournier, P.-A. Pari, and Y. Surrel. 1998. “Direct identification of elastic constants of anisotropic plates by modal analysis: experiments and results.” *Journal of Sound and Vibration* 210(5):645–59.
- Han, L., J. P. Newhook, and A.A. Mufti. 2004. Centralized remote structural monitoring and management of realtime data. Paper presented at the SPIE International Symposium on Smart Structures and Materials, March 2004.
- Harrison, G. R. 1949. “The production of diffraction gratings. I. Development of the ruling art” *Journal of the Optical Society of America* 39(6): 413 – 426.
- Haynes, Ch. L., and R.P. Van Duyne. 2001. “Nanosphere Lithography: A Versatile Nanofabrication Tool for Studies of Size-Dependent Nanoparticle Optics.” *The Journal of Physical Chemistry B* 105(24): 5599–5611.
- He, B. B., U. Preckwinkel, and K. L. Smith. 2000. “Fundamentals of two-dimensional X-ray diffraction (XRD2).” Paper presented at the Denver X-ray Conference (DXC) Applications of X-ray Analysis. July / August 2000.
- Hecht, Eugene. 2002. Optics. San Francisco: Addison Wesley.
- Holgado, M., et al. 1991 “Electrophoretic deposition to control artificial opal growth.” *Langmuir* 15(14): 4701 – 4704.

- Hoogenboom, J.P., C. Rétif, E. de Bres, M. van de Boer, A. K. van L. Suurling, J. Romijn, and A. van Blaaderen. “Template-Induced Growth of Close-Packed and Non-Close-Packed Colloidal Crystals during Solvent Evaporation.” *Nano Letters* 4, no.2 (2004): 205 – 208.
- Hsu, C. M., S. T. Connor, M. X. Tang, and Y. Cui. 2008. “Wafer-Scale Silicon Nanopillars and Nanocones by Langmuir-Blodgett Assembly and Etching.” *Applied Physics Letters* 93(13): 133109
- Hsu, W. P., R. Yu, and E. Matijevic. 1993 “Paper Whiteners: I. Titania Coated Silica.” *Journal of Colloid and Interface Science*. 156 (1): 56-65
- Hu, W., H. Li, B. Chang, J. Yang, Z. Li, J. Xu, and D. Zhang. 1995. “Planar Optical Lattice of TiO₂ Particles.” *Optics Letters* 20 (9): 964-966.
- Huang, Z. P., H. Fang, and J. Zhu. 2007 “Fabrication of Silicon Nanowire Arrays with Controlled Diameter, Length, and Density.” *Advanced Materials* 19 (5): 744 – 748.
- Huke, P., R. Klattenhoff, C. von Kopylow, and R. B. Bergmann. 2013. “Novel Trends in Optical Non-Destructive Testing Methods.” *Journal of the European Optical Society: Rapid Publications* 8:
- Hulteen, J. C., and R. P. Van Duyne. 1994. “Nanosphere Lithography: A Materials General Fabrication Process for Periodic Particle Array Surfaces.” *Journal of Vacuum Science and Technology A* 13(3): 1553 – 1558.
- Hulteen, J. C., D. A. Treichel, M. T. Smith, M. L. Duval, T. R. Jensen, R. P. V. Duyne. 1999. “Nanosphere Lithography: Size-Tunable Silver Nanoparticle and Surface Cluster Arrays.” *The Journal of Physical Chemistry B* 103(19): 3854–3863.
- Hung, Y. Y. 1996. “Shearography for Non-destructive Evaluation of Composite Structures.” *Optics and Lasers in Engineering* 24 (2 – 3):161 – 182.
- Hunter, R. J. 1993. *Introduction to Modern Colloid Science*. Oxford: Oxford University Press.
- Isis Canada. 2004. *ISIS Educational Module 5: An Introduction to Structural Health Monitoring*.

- Jang, S. G., H. K. Yu, D. G. Choi, and S. M. Yang. 2006. “Controlled Fabrication of Hollow Metal Pillar Arrays Using Colloidal Masks.” *Chemistry of Materials* 18(26): 6103 – 6105.
- Jang, S.G., D. G. Choi, C. J. Heo, S. Y. Lee, and S. M. Yang. 2008. “Nanoscale Ordered Voids and Metal Caps by Controlled Trapping of Colloidal Particles at Polymeric Film Surfaces.” *Advanced Materials* 20(24): 4862 – 4867.
- Jiang, P. 2005. “Wafer-Scale Fabrication of Periodic Polymer Attolitre Microvial Arrays.” *Chemical Communication* (13): 1699 – 1701. doi: 10.1039/B418447E.
- Jiang, P. 2006. “Large-Scale Fabrication of Periodic Nanostructured Materials by Using Hexagonal Non-Close-Packed Colloidal Crystals as Templates.” *Langmuir* 22(9): 3955 – 3958.
- Jiang, P., J. F. Bertone, K. S. Hwang, and V. L. Colvin. 1999. “Single-Crystal Colloidal Multilayers of Controlled Thickness.” *Chemistry of Materials* 11(8): 2132 – 2140. doi: 10.1021/cm990080.
- Jiang, P., T. Prasad, M.J. McFarland, and V. L. Colvin. 2006. “Two-Dimensional Non-Close-Packed Colloidal Crystals Formed by Spin Coating.” *Applied Physics Letters*. 89(1): 011908-01 – 011908-03.
- Jimenez, F. L., Sh. Kumar and P.M. Reis. 2016. “Soft Colour Composites with Tuneable Optical Transmittance.” *Advanced Optical Materials* 4 (4): 620 – 626.
- Jin, C.J., Z. Y. Li, M.A. McLachlan, D.W. McComb, R.M. De La Rue, N. P. Johnson. 2006. “Optical Properties of Tertragonal Photonic Crystal Synthesized via Template – Assisted Self-Assembly.” *Journal of Applied Physics*. 99 (11):116109
- Jing, P., J. Wu, and L.Y. Lin. 2014. “Patterned Optical Trapping with Two-Dimensional Photonic Crystals.” *ACS Photonics* 1: 398–402.
- Johnson, S. G., and J. D. Joannopoulos. 2003. Introduction to Photonic Crystals: Bloch's Theorem, Band Diagrams, and Gaps (But No Defects). Massachusetts Institute of Technology (MIT), Cambridge.

- Jun, S., and Y.-S. Cho. 2003. “Deformation-Induced Bandgap Uning of 2D Silicon-Based Photonic Crystal.” *Optics Express* 11(21): 2769 – 2774.
- Kelb, Ch., E. Reithmeier, and B. Roth. 2014. “Foil- Integrated 2D Optical Strain Sensors” *Procedia Technology* 15: 710 – 715.
- Khodadad, I., N. Dhindsa, and S.S. Saini. 2016. “Refractometric Sensing Using High-Order Diffraction Spots from Ordered Vertical Silicon Nanowire Arrays.” *IEEE Photonics Journal* 8 (2). doi: 10.1109/JPHOT.2016.2548469
- Kim, B. – J., H. Jung, H. – Y. Kim, J. Bang, and J. Kim. 2009. “Fabrication of Gan Nanorods by Inductively Coupled Plasma Etching via SiO₂ Nanosphere Lithography.” *Thin Solid Films* 517(14): 3859 – 3861.
- Kim, J.-A., K.-C. Kim, E. W. Bae, S. Kim, and Y. K. Kwak. 2000. „Six-degree-of-freedom displacement measurement using a diffraction grating.” *Review of Scientific Instruments* 71(8): 3214 – 3219.
- Kim, M. H., S. H. Im, and O. O. Park, *Advanced Functional Materials* 15(8): 1329 – 1335.
- Kim, S., and V. Gopalan. 2001. “Strain-Tunable Photonic Band Gap Crystals.” *Applied Physics Letters* 78(20): 3015 – 3017. doi:10.1063/1.1371786.
- Kondo, M., K. Shinozaki, L. Bergstrom, and N. Mizutani. 1995. “Preparation of Colloidal Monolayers of Alkoxylated Silica Particles at the Air-Liquid Interface.” *Langmuir* 11(2): 394 – 397.
- Kosaka, H, T. Kawashima, A. Tomita, M. Notomi, T. Tamamura, T. Sato, and S. Kawakami. 1998. “Superprism phenomena in photonic crystals.” *Physical Review B* 58(16): R10 096 – R10 099.
- Lau, K.T. 2003. “Fibre-optic sensors and smart composites for concrete applications.” *Magazine of Concrete Research*, February.
- Launay, J., F. Lahmar, P. Boisse, P. Vacher. 2002. “Strain Measurement in Tests on Fibre Fabric by Image Correlation Method.” *Advanced Composites Letters* 11(1):7–12.
- Lazarov, G. S, N. D. Denkov, O. D. Velev, P. A. Kralchevsky, and K. Nagayama. 1994. “Formation of Two-dimensional

Structures from Colloidal Particles on Fluorinated Oil Substrate.” *Journal of the Chemical Society, Faraday Transactions* 90(14): 2077 – 2084. doi: 10.1039/FT9949002077.

- LeMagorou, L., F. Bos, and F. Rouger. 2002. “Identification of Constitutive Laws for Wood-Based Panels by Means of an Inverse Method.” *Composites Science and Technology* 62(4):591 – 596.
- Lenzmann, F., K. Li, A. H. Kitai, and H. D. H. Stover. 1994. “Thin-film micropatterning using polymer microspheres.” *Chemistry of Materials* 6(2): 156 – 159.
- Li, Y., E.J. Lee, W. Cai, K.Y. Kim, and S. O. Cho. 2008. “Unconventional Method for Morphology-Controlled Carbonaceous Nanoarrays Based on Electron Irradiation of aPolystyrene Colloidal Monolayer.” *ACS Nano* 2(6): 1108 – 1112.
- Lilliu, Samuele, and Thomas Dane. 2015. Reciprocal space mapping for dummies. Cornell University Library. arXiv:1511.06224
- Lourtioz, J.-M. 2005. “Foreward”. In *Photonic Crystals: Towards Nanoscale Photonic Devices*, edited by J.-M. Lourtioz. Translated by P.-N. Favennec. Berlin: Springer.
- Luo, Ch, S. G. Johnsona, M. Soljačić, J. D. Joannopoulos, and J. B. Pendryb. 2004. “Novel optical phenomena with photonic crystals.” In *Proceeding SPIE 5166: UV/Optical/IR Space Telescopes: Innovative Technologies and Concepts*, edited by H. A. MacEwen, 207. Bellingham: SPIE.doi:10.1117/12.507
- Maheshwari, M., V. G. M. Annamdas, J. H. L. Pang, A. Asundi, S. C. Tjin. 2017. “Crack Monitoring Using Multiple Smart Materials; Fiber-optic sensors & Piezo sensors.” *International Journal of Smart and Nano Materials* 8(1): 47 – 55. doi: 10.1080/19475411.2017.1298220
- Mao, Q, B. Zhao, D. Sheng, and Z. Li. 1996. “Resistance changement of compression sensible cement specimen under different stresses.” *Journal Wuhan University of Technology* 11 (3): 41 – 45.

-
- Marczewski, D., and W. A. Goedel. 2005. "The preparation of sub micrometer sized rings by embedding and selective etching of spherical silica particles." *Nano Letters* 5: 295 – 299.
 - Mata A., A.J. Fleischman, S. Roy." 2005 Characterization of polydimethylsiloxane (PDMS) properties for biomedical micro/nanosystems." *Biomed Microdevices*. 7(4):281-293.
 - McDonald Cooper J., and G.M. Whitesides. 2002. "Poly(dimethylsiloxane) as a Material for Fabricating Microfluidic Devices" *Accounts of Chemical Research* 35(7): 491 – 499.
 - McNeill, D. 2004. "Novel Event Localization of SHM Data Analysis." Paper presented at the Second International Workshop on Structural Health Monitoring of Innovative Civil Engineering Structures, Winnipeg, September 22-23.
 - Meuwissen, M.H.H. 1998. "An Inverse Method for THE Mechanical Characterization of Metals." Phd diss, Eindhoven University of Technology.
 - Micheletto, R., H. Fukuda, and M. Ohtsu. 1995. "A Simple Method for the Production of a Two-dimensional, Ordered Array of Small Latex Particles." *Langmuir* 11(9), 3333 – 3336.
 - Miller, R. J., and H. F. Gleeson. 1996. "Lattice Parameter Measurements from the Kossel Diagrams of the Cubic Liquid Crystal Blue Phases." *Journal de Physique II* 6: 909 – 922.
 - Minati, L., A. Chiappini, C. Armellini, A. Carpentiero, D. Maniglio, A. Vaccari, L. Zur, A. Lukowiak, M. Ferrari, and G. Speranza. 2017. "Gold Nanoparticles 1D Array as Mechanochromic Strain Sensor." *Materials Chemistry and Physics* 192: 94 – 99,
 - Mio, C., and M. D. W. Marr.1999. "Tailored Surfaces Using Optically Manipulated Colloidal Particles." *Langmuir* 15(25): 8565 – 8568.
 - Moharam, M. G., E. B. Grann, and D.A. Pommet. 1995. "Formulation for Stable and Efficient Implementation of the Rigorous Coupled-Wave Analysis of Binary Gratings". *Journal of the Optical Society of America A* 12(5): 1068 – 1076.
 - Mollenhauer, D., and K. Reifsnider. 2000. "Measurements of Interlaminar Deformation along the Cylindrical Surface of a Hole in Laminated Composite Materials by Moiré

- Interferometry.” *Composites Science and Technology* 60: 2375 – 2388.
- Mollenhauer, D.H. 1997. “Interlaminar Deformation at a Hole in Laminated Composites: A Detailed Experimental Investigation Using Moiré Interferometry.” PhD diss., Virginia Polytechnic Institute and State University.
 - Muñoz, H.E. “PDMS: The Favorite Material of Microfluidics (for now)”. Published October 27, 2011. <https://www.microfluidicfuture.com/blog/pdms-the-favorite-material-of-microfluidics-for-now>.
 - Newman, JW. 1991. “Production and field inspection of composite aerospace structures with advanced shearography”. In *Review of Progress in Quantitative Nondestructive Evaluation: Volume 10b*, edited by 2129 – 2133. New York: Springer.
 - Ng, E.C.H., Y.K. Koh, and C.C. Wong. 2012. Colloidal crystals. In *Modern aspects of bulk crystal and thin film preparation*, edited by N. Kolesnikov and E. Borisenko, 579 – 608. Rijeka: In Tech.
 - O’Connor, D.J. 1989. “A Comparison of Test Methods for Shear Properties of the Cores of Sandwich Construction.” *Journal of Test and Evaluation* 17(4):241 – 246. doi: 10.1520/JTE11121J
 - Ohmori, M., and E. Matijevic. 1992. “Preparation and Properties of Uniform Coated Colloidal Particles. VII. Silica on Hematite.” *Journal of Colloid Science* 150(2): 594 – 598.
 - Osten, W., F. Elandalousi, and W. Jüptner. 1996. “Recognition by Synthesis – A New Approach for The Recognition of Material Faults in HNDE.” In *Proceeding of. SPIE: Laser Interferometry VIII: Applications*, 220–224.
 - Osten, W. 2008 “Digital Image Processing for Optical Metrology”. In *Springer Handbook of Experimental Solid Mechanics*, edited by William N. Sharpe, 481 – 564. New York: Springer.
 - Palmer, Ch., and E. Loewen. 2004. *Diffraction Grating. Handbook*. 6th ed. New York: Newport Corporation.

- Park, W., J. – B. Lee. 2004. “Mechanically tunable photonic crystal structure.” *Applied Physics Letters* 85(21): 4845 – 4847. doi: 10.1063/1.1823019.
- Peng, K. Q., M. L. Zhang, A. J. Lu, N. B. Wong, R. Q. Zhang, and S. T. Lee. 2007. “Ordered Silicon Nanowire Arrays via Nanosphere Lithography and Metal-Induced Etching.” *Applied Physics* 90(16): 163123. doi: 10.1063/1.2724897
- Pierron F, and M. Grédiac. 2000. “Identification of The Through-Thickness Moduli of Thick Composites from Whole-Field Measurements Using the Iosipescu Fixture: Theory and Simulations.” *Composites: Part A* 31(4): 309 – 318.
- Pierron, F, S. Zhavaronok, and M. Grédiac. 2000. “Identification of The Through Thickness Properties of Thick Laminates Using the Virtual Fields Method.” *International Journal of Solids and Structures* 37(32):4437–4453.
- Pursiainen, O. L.J., J. J. Baumberg, K. Ryan, J. Bauer, H. Winkler, B. Viel, and T. Ruhl. 2005. “Compact Strain- Sensitive Flexible Photonic Crystals for Sensors.” *Applied Physics Letters* 87 (10): 101902. doi: 10.1063/1.2032590.
- Rahimi, R., M. Ochoa, W. Yu, and Babak Ziaie. 2015. “Highly Stretchable and Sensitive Unidirectional Strain Sensor via Laser Carbonization.” *ACS Applied Materials & Interfaces* 7(8):4463–4470;
- Rastogi P. K. 1998. “Speckle shearing photography: a tool for direct measurement of surface strains.” *Applied Optics* 37(8): 1292-1298.
- Rauch, B.J., and R.E. Rowlands. 1993. “Thermoelastic stress analysis”. In: *Handbook on experimental mechanics*, edited by A. Kobayashi, 581–599. Weinheim: Wiley
- Ren, Z. Y., X. M. Zhang, J. H. Zhang, X. Li, and B. Yang. 2009. “Building cavities in microspheres and nanospheres.” *Nanotechnology* 20(6): 065305.
- Ruhl, T., P. Spahn, G.P. Hellmann. (2003). “Artificial Opals Prepared by Melt Compression.” *Polymer* 44: 7625 – 7634. doi: 10.1016/j.polymer.2003.09.047.
- S. Park, C.-B. Yun, Y. Roh, and J.-J. Lee. 2006 “Pzt-Based Active Damage Detection Techniques for Steel Bridge Components.” *Smart Materials and Structures* 15(4):957 – 966.

- Savio, E., L. De Chiffre, and R. Schmitt. 2007. "Metrology of Freeform Shaped Parts." *CIRP Annals – Manufacturing Technology* 56: 810 – 835.
- Scruby, C., and L. Drain. 1990. *Laser Ultrasonics: Techniques and Application*. Bristol: Institute of Physics Publishing.
- Sheu, H. R., M. S. El-Aasser, and J. W. Vanderhoff. 1987. "Phase Domain Formation in Latex Interpenetrating Polystyrene Networks." *Polymeric Materials: Science and Engineering Division* 57, 911 – 915.
- Shih, T.-K., Ch.-F. Chen, J. – R. Ho, F.-T. Chuang. 2006. "Fabrication of PDMS(polydimethylsiloxane) microlens and diffuser using replica molding." *Microelectronic Engineering* 83 (11–12):2499 – 2503.
- Shuaeib, F.M., and P.D. Soden. 1997. "Indentation Failure of Composite Sandwich Beams." *Composites Science and Technology* 57(9): 1249 – 1259.
- Stepinski, T., and M. Jonsson. 2004. "Narrowband Ultrasonic Spectroscopy for NDE of Layered Structures." In *Proceedings of 16th World Congress of NDT* (ABENDE, BINDT, Munich, 2004).
- Stratoudaki, T, J. Hernandez, M. Clark, and M. Somekh. 2007. "Cheap Optical Transducers (CHOTs) for Narrowband Ultrasonic Applications." *Measurement Science and Technology*. 18: 843 – 851.
- Strong, J. 1960. "Johns Hopkins University and diffraction gratings." *Journal of the Optical Society of America* 50(12): 1148 – 1152.
- Suh, W., M. F. Yanik, O. Solgaard, and Sh. Fan. 2003. "Displacement-sensitive photonic crystal structures based on guided resonance in photonic crystal slab." *Applied Physics Letter* 82(13): 1999 – 2001. doi: 10.1063/1.1563739.
- Sukhoivanov, I. A., and I. V. Guryev. 2009. *Photonic Crystals: Physics and Practical Modeling*. Berlin: Springer.
- Sun, C. H., A. Gonzalez, N. C. Linn, P. Jiang, and B. Jiang. 2008. "Templated biomimetic multifunctional coatings." *Applied Physics Letters* 92(5): 051107.
- Sun, F.Q, W. P. Cai, Y. Li, B. Q. Cao, Y. Lei, and L. D. Zhang. 2004. "Morphology-Controlled Growth of Large-Area Two-

- Dimensional Ordered Pore Arrays.” *Advanced Functional Materials*. 14(3): 283–288.
- Sun, J., Ch. Tang, P. Zhan, Z.-l. Han, Z. – Sh. Cao, and Z.-L. Wang. 2010. “Fabrication of centimeter-sized single-domain two-dimensional colloidal crystals in a wedge-shaped cell under capillary forces”. *Langmuir* 26(11):7859 – 7864.
 - Sun, M., M. W. J. Staszewski, and R. N. Swamy. 2010. “Smart Sensing Technologies for Structural Health Monitoring of Civil Engineering Structures.” *Advances in Civil Engineering*
 - Sun, M.Q., W.J. Staszewski, R.N. Swamy, and Z.Q. Li. 2008. “Application of low-profile piezoceramic transducers for health monitoring of concrete structures.” *Ndt and E International* 41(8): 589 – 595.
 - Sun, Z.Q., Y. Li, J. H. Zhang, Y. F. Li, Z. H. Zhao, K. Zhang, G. Zhang, J. R. Guo, B. Yang. 2008. “A universal approach to fabricate various nanoring arrays based on a colloidal-crystal-assisted-lithography strategy.” *Advanced Functional Materials* 18(24): 4036 – 4042.
 - Surrel, Y. 2000. “Fringe Analysis.” In: *Photomechanics. Topics in Applied Physics 77*, edited by P.K. Rastogi, 55 – 99, Berlin: Springer.
 - Sutton, M. A., S. R. McNeill, J. D. Helm, and Y. J. Chao. 1999. “Advances in Two-Dimensional and Three-Dimensional Computer Vision.” In *Photomechanics*, edited by P. K. Rastogi, 323 – 372. Berlin: Springer.
 - Tamulevičius, T., I. Gražulevičiūtė, A. Jurkevičiūtė, and S. Tamulevičius. “The calculation, fabrication and verification of diffraction grating based on laser beam splitters employing a white light scatterometry technique.” *Optics and Lasers in Engineering* 51:1185–1191.
 - Tan, B. J. -Y., K. -Y. Lim, F. -C. Cheong, G.L. Chong, A.T.-S. Wee, and C. -K. Ong. 2004. “Fabrication of Two-Dimensional Periodic Non-Close-Packed Array of Polystyrene Particles.” *Journal of Physical Chemistry B*. 108(48): 18575 – 18579.
 - Tan, Y. and H. Chen. 2012. “Diffraction of transmission light through triangular apertures in array of retro-reflective microprisms.” *Applied Optics* 51(16): 3403 – 3409.

- Tandon, S.N., M. Soljagic, G.S. Petrich, J.D. Joannopoulos, and L.A. Kolodziejski. 2005. "The superprism effect using large area 2D-periodic photonic crystal slab." In *Photonics and Nanostructures-Fundamentals and Applications 3*: 10 – 18.
- Templeton, DW. 1987. "Computerization of Carrier Fringe Data Acquisition, Reduction and Display." *Experimental Techniques* 11 (11): 26–30.
- Thangawng, A.L., R.S. Ruoff, M.A. Swartz, M.R. Glucksberg. 2007 "An Ultra-Thin PDMS Membrane as a Bio/Micro-Nano Interface: Fabrication and Characterization." *Biomed Microdevices* 9(4):587 – 595.
- Tilley, R. 2011. *Colour and the Optical Properties of Materials: An Exploration of the Relationship Between Light the Optical Properties of Materials and Colour*, 211 – 225. West Sussex: John Wiley & Sons
- Trau, M., D. A. Saville, and I. A. Aksay. 1996. "Field-Induced Layering of Colloidal Crystals." *Science* 272(5262):706-709.
- Tyrrell, Y.R. 1997. "Electronic Speckle Pattern Interferometry." In *Optical Measurements Methods in Biomechanics*, edited by J.F. Orrer and J.C. Shelton, 99 – 124. London: Chapman & Hall.
- Ugelstad, J. et al.1992. "Preparation and application of new monosized polymer particles." *Progress in Polymer Science* 17(1): 87-161.
- Valsesia, A., P. Lisboa, P. Colpo, and F. Rossi. 2006. "Fabrication of Polypyrrole-Based Nanoelectrode Arrays by Colloidal Lithography." *Analytical Chemistry* 78 (21): 7588 – 7591.
- Vautrin, A., J.R. Lee, J. Molimard, Y. Surrél Y. 2002." Full-field optical techniques: applications to strain measurement and mechanical. In: *Proceedings of the 10th European conference on composite materials. (ECCM10)*, Bruges, Belgium; 2002
- Venkatesh, S., P. Jiang, and B. Jiang. 2007. "Generalized fabrication of two-dimensional non-close-packed colloidal crystals." *Langmuir* 23(15): 8231 – 8235.
- von Kopylow, C., O. Focke, and M. Kalms. 2007. "Laser Ultrasound – A flexible Tool for the Inspection of Complex CFK Components and Welded Seams," *Proc. SPIE* 6616, 66163J

- Walz, T., and A. Ettermeyer. 1998. "Automatic shearography system for helicopter rotor blades." *Proceedings of SPIE* 3397: 187–192.
- Ward, A. J. I., and S. E. Friberg. 1989. *MRS Bulletin* 14(12):41 – 46.
- Wasowski J.J., and L.M. Wasowski. 1987. "Computer-based Optical differentiation of fringe patterns." *Experimental Techniques* 11(3):16–18.
- Weekes, S. M., F. Y. Ogrin, W. A. Murray, and P. S. Keatley. 2007. "Macroscopic Arrays of Magnetic Nanostructures from Self-Assembled Nanosphere Templates." *Langmuir* 23(3): 1057 – 1060.
- Welch, V., V. Lousse, O. Deparis, A. Parker, and J. P. Vigneron. 2007. "Orange Reflection from a Three-Dimensional Photonic Crystal in the Scales of The Weevil *Pachyrrhynchus Congestus* Pavonius (Curculionidae)." *Physical Review E* 75 (4): 041919; doi: 10.1103/PhysRevE.75.041919
- Wen, Y., Y. Chen, P. Li, D. Jiang, and H. Guo. 2007. "Smart concrete with embedded piezoelectric devices: implementation and characterization," *Journal of Intelligent Materials, Systems and Structures* 18 (3):265–274.
- Wickman, H. H., and J. N. Korley. 1998. "Colloid crystal self-organization and dynamics at the air/water interface." *Nature* 393:445 – 447. doi:10.1038/30930.
- Wileman, P., J.M. Coupland, C.D. Creasey, D.M. Rowley, and N.A. Halliwell. 1994. "The laser strain gauge: micro machining of diffraction gratings using an excimer laser." *Strain* 30(1): 15 – 18.
- Wong, Eehern J. "Modelling and control of rapid cure in polydimethylsiloxane (PDMS) for microfluidic device applications." PhD diss., Massachusetts Institute of Technology, 2010.
- Wu, F., and F.K. Chang. 2001. "Diagnosis of debonding in steel-reinforced concrete with embedded piezoelectric elements." In proceeding of the 3rd International Workshop on Structural Health Monitoring: The Demands and Challenges
- Xia, Y., and G. M. Whitesides. 1998. "Soft Lithography," *Angewandte Chemie International Edition* 37(5): 550 – 575.

- Xia, Y., B. Gates, Y. Yin and Y. Lu. 2000. “Monodispersed Colloidal Spheres: Old Materials with New Applications.” *Advanced Materials* 12(10): 693–713.
- Xing, Y.M., H. Yun, F.L. Dai. 1999. “An Experimental Study of Failure Mechanisms in Laminates with Dropped Plies.” *Composites Science and Technology* 59:1527–31.
- Xu, F., J.W. Durham, III, B. J. Wiley, and Y. Zhu. “Strain-Release Assembly of Nanowires on Stretchable Substrates” *ACS Nano* 5, no. 2 (2011): 1556 – 1563.
- Xu, H, and W. A. Goedel. 2003. “Mesoscopic rings via controlled wetting of particle imprinted templates.” *Angewandte Chemie Internatnl.* Ed. 42: 4696 – 4700.
- Y. Y. Lim, Y.Y., S. Bhalla, and C. K. Soh. 2006. “Structural identification and damage diagnosis using self-sensing piezo-impedance transducers.” *Smart Materials and Structures* 15 (4): 987 – 995.
- Yablonovitch, E. 2007. “Photonic Crystals: What’s in a Name?” *Optics & Photonics News*, March
- Yan, L., K. Wang, J. Wu, L. Ye. 2006. “Hydrophobicity of model surfaces with closely packed nano- and micro- spheres.” *Colloids and Surfaces A: Physicochem. Eng. Aspects* 296, no. (2006): 123 – 131.
- Yan, X., J. M. Yao, G. Lu, X. Li, J. H. Zhang, D.F. Zhu, W. Li, X. Zhang, and B. Yang. 2005. “Fabrication of Non-Close-Packed Arrays of Colloidal Spheres by Soft Lithography.” *Journal of the American Chemical Society* 12(21): 7688 – 7689.
- Yoshiyama, T., I. Sogami, and N. Ise. 1984. “Kossel line analysis on colloidal crystals in semidilute aqueous solutions.” *Physical Review Letters* 53(22): 2153 – 2158
- Yu, C, K. O’Brien, Y.-H. Zhang, H. Yu, and H. Jiang. 2010. “Tunable Optical Gratings Based on Buckled Nanoscale Thin Films on Transparent Elastomeric Substrates.” *Applied Physics Letters* 96: 041111-1- 041111-3.
- Zaiser, E. M., and V. K. LaMer. 1948. “The kinetics of the formation and growth of monodispersed sulfur hydrosols.” *Journal of Colloid Science* 3(6): 571 – 598.
- Zhang, J., Y. Li, X. Zhang, and B. Yang. 2010 “Colloidal self-assembly meets nanofabrication: from two-dimensional

- colloidal crystals to nanostructure arrays.” *Advanced Materials* 22(38): 4249 – 4269.
- Zhang, J., Y. Li, X. Zhang, and B. Yang. 2010. “Colloidal Self – Assembly Meets Nanofabrication: From two – dimensional colloidal crystals to nanostructure arrays.” *Advanced Materials* 22(38): 4249 – 4269.
 - Zhang, P., C. Ying, and J. Shen. 1997. “Directivity patterns of laser thermoelastically generated ultra-sound in metal with consideration of thermal conductivity.” *Ultrasonics* 35(3): 233 – 240.
 - Zhao, B., and A. Asundi. 1999. “Strain microscope with grating diffraction method.” *Optical Engineering* 38(1): 170-174.
 - Zhao, Q., et al. (2012). “Electric- Field-Tuned Color in Photonic Crystal Elastomers”. *Applied Physics Letters* 100(10): 101902. doi: 10.1063/1.3691930.
 - Zonta, D., A. Chiappini, A. Chiasera, M. Ferrari, M. Pozzi, L. Battisti, and M. Benedetti. 2009. “Photonic crystals for monitoring fatigue Photonic crystals for monitoring fatigue phenomena in steel structures” *Proceedings of SPIE* 7292. doi: 10.1117/12.814915;